12-2016

Ambient ionization - mass spectrometry: Advances toward intrasurgical cancer detection

Alan Keith Jarmusch
Purdue University

Recommended Citation

Jarmusch, Alan Keith, "Ambient ionization - mass spectrometry: Advances toward intrasurgical cancer detection" (2016). *Open Access Dissertations*. 950.
https://docs.lib.purdue.edu/open_access_dissertations/950

Graduate School Form 30
(Updated 11/20/2014)

PURDUE UNIVERSITY
GRADUATE SCHOOL
Thesis/Dissertation Acceptance

This is to certify that the thesis/dissertation prepared

By Alan Keith Jarmusch

Entitled AMBIENT IONIZATION - MASS SPECTROMETRY: ADVANCES TOWARD INTRASURGICAL CANCER DETECTION

For the degree of Doctor of Philosophy

Is approved by the final examining committee:

R. Graham Cooks

Philip S. Low

Peter T. Kissinger

Mary J. Wirth

To the best of my knowledge and as understood by the student in the Thesis/Dissertation Agreement, Publication Delay, and Certification/Disclaimer (Graduate School Form 32), this thesis/dissertation adheres to the provisions of Purdue University's "Policy on Integrity in Research" and the use of copyrighted material.

Approved by Major Professor(s): R. Graham Cooks

Approved by: Timothy Zwier 08/15/2016

Head of the Department Graduate Program Date

AMBIENT IONIZATION - MASS SPECTROMETRY: ADVANCES TOWARD INTRASURGICAL CANCER DETECTION

A Dissertation

Submitted to the Faculty

of

Purdue University

by

Alan Keith Jarmusch

In Partial Fulfillment of the

Requirements for the Degree

of

Doctor of Philosophy

December 2016

Purdue University

West Lafayette, Indiana

For my wife, Amie, parents, Keith and Linda, siblings, Scott and Samantha,
friends and family.

ACKNOWLEDGEMENTS

I cannot begin to list the numerous contributions of the people that have supported me throughout my dissertation research, so for those of you I do not explicitly mention – thank you. My career as a scientist is due to a few very talented scientists and excellent mentors. Professor Nadja B. Cech, my undergraduate academic and research mentor, exposed me to analytical chemistry and convinced me to pursue graduate research. Thank you for your guidance, positivity, and continued support. Professor R. Graham Cooks, my Ph.D. mentor, provided an unparalleled graduate education in mass spectrometry. I cannot express how thankful I am for my experience and your guidance. I will cherish our conversations as much as the science. The environment you have fostered in Aston Labs is unique and your approach to mentorship continues to inspire me. I wholeheartedly appreciate everything that you have done for me. I would also like to thank my committee members for their role in my graduate education, thank you Professor Peter Kissinger, Professor Philip Low, and Professor Mary Wirth.

The contributions of my fellow Astonites deserves recognition. Livia Eberlin, the first person I meet in the lab, thank you for your teaching me about DESI imaging. Your contributions to ambient ionization in medicine are inspiring, and I hope that together we

can improve patient care through better diagnostic methods. Kevin Kerian, I really enjoyed our time working together and traveling to Indianapolis for research. Zane Baird, thank you for teaching me more about 3D printing and electronics – normally over a cold adult beverage. I would be remiss not to mention the help and comradery of Cedric D'Hue, Karen Yannell, Christina Ferreira, and Katelynn Smith. Valentina Pirro, I have learned a lot from you, possibly more than any other of our fellow Astonites, and hope to maintain a strong friendship wht you over the coming years. Clint Alfaro, you are the future of DESI imaging and I can't imagine a more capable person. Enjoy your time and work hard – always keep the overall picture in mind. I could not have accomplished what I have without the support of those in Aston Labs and for that I am forever grateful to all of you.

I would like to acknowledge the contributions of our physician collaborators. Thank you Dr. Aaron Cohen-Gadol and Dr. Eyas Hattab for your assistance in the human brain cancer studies. Human prostate and kidney cancer studies would have been impossible without the contributions of Dr. Timothy Masterson and Dr. Liang Cheng. The input of Dr. Michael Childress, Dr. José Ramos-Vara, and Dr. Craig Thompson to the study of canine non-Hodgkin's lymphoma was invaluable. The knowledge from these talented physicians-scientists has been paramount to my personal and professional growth, and I will be forever grateful for the opportunity to work with you all. I hope that the excellent research we have produced will become the foundation for future studies and translation of the laboratory science into clinical practice.

The enormous support and love of my friends and family cannot be fully reflected in this dissertation. My parents, Keith and Linda, instilled character and work ethic in me, two qualities that have directly impacted my graduate study and life. I am forever grateful for their support and unconditional love – thank you, mom and dad. Scott and Samantha, my siblings, I could not be more proud of your individual accomplishments – personal and professional. I love you both and will always support you. Mathew Jordan, my closest friend, thank you for providing me with all the personal joy in the world, laughter is a powerful medicine. To my friends that are too many to mention, thank you for your support and love – I cannot wait to see what our future lives hold. Miles, my dog, thank you for always being happy to see me when I get home, regardless of what good or bad has happened that day. And last but absolutely not least, Amie, my wife, who in many ways has put in an equivalent amount of blood, sweat, and tears into my graduate study. You are my sunshine and continue to be my best friend – I love you more each and every day. I look forward to our future adventures and new moments that we can share together. Whether it be a backpacking vacation or simply sharing a cup of coffee in the morning – I'm glad to have you as my partner.

TABLE OF CONTENTS

Page

LIST OF TABLES

Table Page

Table Page

LIST OF FIGURES

Figure Page

Figure Page

Figure Page

ABSTRACT

Jarmusch, Alan Keith. Ph.D., Purdue University, December 2016. Ambient Ionization - Mass Spectrometry: Advances toward Intrasurgical Cancer Detection. Major Professor: R. Graham Cooks.

My dissertation research has focused on the development of ambient ionization – mass spectrometry (MS) for clinical measurements, specifically intrasurgical cancer detection. The molecular differences between normal and cancerous tissue were detected via direct tissue analysis in vitro by touch spray ionization (TS) or by analyzing sectioned or smeared tissue using desorption electrospray ionization (DESI). The physical form of the tissue, e.g. in vitro sampling, sectioned, or smeared, was inconsequential in differentiating normal from cancerous tissue; however, the spectra acquired by TS and DESI differed due to differences in ionization processes. We envision that TS-MS and DESI-MS could impact diagnostic medicine, for example in providing surgeons with rapid, near real-time information as to tissue disease state, i.e. normal or tumor. Disease state information provided to surgeons about discrete pathologically ambiguous areas, ideally intrasurgically via TS or DESI-MS smear analysis, could improve the completeness of tumor resection while minimizing unintended damage to adjacent tissue.

Touch spray ionization was developed for intrasurgical detection of cancer; TS greatly simplifies MS analysis by using the same device for in vivo sampling and subsequent ionization. Frozen tissue sections were sampled and analyzed by TS-MS providing the ability to differentiate normal from human prostate cancer, via lipid profiles, using multivariate statistics. The next proof-of-concept step for TS-MS was the analysis human kidney cancer specimens in vitro, immediately following resection. TS-MS analysis of untreated kidney tissue emulated intrasurgical use, e.g. the presence and co-sampling of biofluids such as blood. Regardless, normal renal tissue and kidney cancer was differentiated using lipid profiles and multivariate statistics.

Desorption electrospray ionization (DESI) - MS imaging of tissue sections differentiated normal from tumor in all cancers studied. DESI-MS imaging of human prostate and human kidney tissue sections were performed to corroborate TS-MS results. Human brain cancer, a major focus of my dissertation research, was studied by imaging tissue sections using DESI-MS to establish the characteristic chemical features, e.g. lipid and metabolite profiles, that distinguish normal brain parenchyma from gliomas and different brain tumors. It was found that information in the negative ion mode lipid profile, positive ion mode lipid profile, and negative ion mode metabolite profile is able to discriminate brain parenchyma (grey and white matter) and gliomas, the most common form of malignant brain tumor. Further, the negative mode lipid and metabolite profiles also proved capable of discriminating different types of brain tumors (gliomas, meningiomas, and pituitary tumors) which account for ~80% of all central nervous system tumors. DESI-MS imaging of effaced or otherwise pathologically ambiguous frozen tissue sections offered the ability to determine the underlying brain parenchyma in cancerous samples – something that traditional morphologic evaluation was not able to determine. Further, DESI-MS was able to detect molecular changes resulting from varying amounts of glioma tumor cells present within infiltrated tissues. The tumor cell percentage of these samples was predicted using N-acetyl-aspartic acid, a neurometabolite which was found to decrease in cancerous tissue, and matched well with histopathologic evaluation.

The transition from DESI-MS imaging of sectioned tissue to DESI-MS analysis of tissue smears was driven by the time restriction of intrasurgical application. The potential of DESI-MS analysis of smears was first demonstrated upon canine non-Hodgkin's lymphoma fine-needle aspirate smears which provided similar sensitivity and specificity values to that of tissue section imaging but is technically less demanding and decreased analysis time. DESI-MS imaging of tissue sections established that MS profiles contained the sufficient information for diagnosis; whereas DESI-MS analysis of tissue smears made the intrasurgical analysis of human brain tumors feasible. The observed lipid or metabolite profiles were not significantly altered by the physical act of smearing and their signal intensities were comparable to those of tissue sections. Further, the chemical information obtained from tissue smears was equivalent to those of tissue sections as determined by canonical component analysis. The culmination of my dissertation research was the creation and implementation of an intrasurgical DESI-MS tissue smear analysis method for human gliomas. Preliminary results from the initial intrasurgical cases analyzed using the developed DESI-MS method are discussed.

CHAPTER 1. INTRODUCTION

1.1 Ambient Ionization – Mass Spectrometry

Ambient ionization refers to a family of methods that produce gas-phase ions outside of the mass spectrometer. Ionization occurs under ambient conditions (e.g. temperature, pressure, and humidity) from untreated samples, greatly reducing or eliminating sample preparation (e.g. extraction, desalting, and pre-concentration). (1, 2) Desorption electrospray ionization (DESI) was the first ambient ionization method, reported in 2004, (3) since then more than forty ambient ionization methods have been described. (4, 5) Ambient ionization methods differ in detail (e.g. spray-based, plasma-based, and laser-based) and in the degree to which ionization is coupled to desorption which can occur via heating, acoustics, momentum transfer, and others. (2, 6) Simplicity and rapid analysis are emphasized; rapid analysis is primarily obtained via relaxed sample pretreatment and lack of chemical separation prior to MS. Ambient ionization methods display near universal applicability with sensitivity allowing for the detection of various compound classes in minute quantities, even when present in complex mixtures (e.g. tissue and biofluids); compounds are measured via mass-to-charge ratios, the ions serving as surrogates of neutral analytes. The lack of chemical separation is compensated by the analytical sensitivity and chemical specificity of mass spectrometry. Additional chemical specificity can be obtained via ion fragmentation and multiple stages of mass analysis (i.e. tandem mass spectrometry or MS^n, where “n” is equivalent to the number of mass analysis stages) which provides structural information. Reduction of sample handling, increased analysis speed, and MS sensitivity and chemical selectivity make ambient ionization – MS well suited in clinical applications.

1.1.1 Desorption Electrospray Ionization (DESI)

DESI generates ions via a strongly coupled desorption and ionization process. Charged solvent is pumped through fused-silica capillary and emitted as charged droplets with a coaxial flow of gas (typically nitrogen) which serves to direct the droplets and assist in droplet evaporation. The charged solvent droplets impact a surface and create a thin-film of solvent into which molecules (i.e. analytes) are dissolved from the analyzed material (e.g. tissue). Subsequent droplets impact the thin-film and splash, via momentum transfer, charged microdroplets toward the mass spectrometer. (7, 8) The microdroplets undergo evaporation and Columbic fission (due to excess surface charge) in processes similar to those in electrospray ionization, yielding gas-phase ions. Selection of the DESI solvent system determines the solubility of analytes (following solubility rules), while other parameters like pneumatic pressure and geometry of the spray, e.g. angle of incidence, affect the efficiency of desorption/ionization process and the spatial resolution in the case of DESI imaging experiments.

1.1.2 Substrate-Based Ambient Ionization

A group of ambient ionization methods exist which rely on spray-based ionization from non-porous and porous substrates, (4) e.g. probe electrospray ionization (PESI), (9) touch spray ionization, (10), and paper spray. (11) The substrate-based methods are unique in that the substrate is used for sample collection (or is the sample) and as the means of ionization. Ionization typically occurs from a sharp tip, naturally present or created, which is used to generate a strong electric field; however, a sharp tip is not necessary as long as a sufficiently strong electric field is created. Solvent or innate fluid present in the sample is electrified and is emitted as charged droplets which undergo evaporation and Coulombic fission, processes of electrospray ionization, eventually yielding analyte ions. Substrate-based ionization methods have varying amounts of desorption and ionization coupling, but the process of sampling and analysis is considered to involve two-steps. The characteristics of substrate-based ambient ionization are advantageous for clinical MS applications; sampling directly onto the substrate can be performed remotely, transported, and rapidly analyzed by MS.

Substrates are divisible based on porosity. Non-porous substrates, such as metal, were initially used for ionization, e.g. use of acupuncture needles in PESI is an early example. Non-porous surfaces are amenable provided they are conductive and terminate in a sharp tip or can otherwise produce a sufficient electric field. Porous substrates, such as paper, wood, (12) plants, (13) and swabs, (14, 15) have been also used and can either be organic (e.g. cellulose) or synthetic (e.g. rayon). Porous substrates provide the ability to selective adsorb components in a mixture, viz. cellulose can be used to selectively absorb polar compounds which interact with the hydroxyl group. Further, such substrates can be chemically modified to adsorb components using targeted interactions, e.g. electrostatic interaction. Paper spray ionization, an illustrative method, has been performed using a variety of modified surfaces including hydrophilic and hydrophobic treatments to cellulose paper. (16) When the substrate can serve both as the means for sample collection and ionization, straightforward analysis of either solid or liquid samples can occur without pretreatment or even sample handling.

1.2 Mass Spectrometry Imaging

Mass spectrometry imaging detects chemical information across two spatial dimension. (17, 18) MS imaging is analogous to light-based chemical imaging techniques, e.g. fluorescence microscopy, Ramen imaging, etc, in regards to detecting chemical information over space; however, detection by mass spectrometry typically offers greater molecular specificity and sensitivity via mass measurement. Sampling occurs from voxels (i.e. three dimensional pixel) based on the thickness of the material and the depth sampling of the ionization method, e.g. solvation by thin-film or ablation by laser. The hyperspectral MS images (two spatial dimensions and “x” number of *m/z* dimensions with associated abundance measurement) provide a unique series of molecular photographs, i.e. ion images (*m/z* value and their corresponding MS abundance), can be used to unravel spatial – chemical relationships.

MS imaging can be performed by a number of ionization methods, principally secondary ion – mass spectrometry (SIMS), (19, 20) matrix-assisted laser desorption ionization (MALDI), (21, 22) and DESI. (5, 23) DESI is performed under ambient conditions whereas SIMS and MALDI are generally carried out within the vacuum of a mass spectrometer. Spatial resolution is one difference between these three ionization sources and range from SIMS, smallest (tens of nm-to-µm), to DESI, largest (tens of µm-mm). The minimum spatial resolution is typically defined by the limitations imposed by the ionization mechanism. SIMS is typically performed using a primary ion bean of elemental atoms (e.g. Cs+) or atomic clusters which impact a surface sputtering secondary ions. The sputtering depth is dependent on the current density of the ion bean, nanometers in static SIMS or up to a few micrometers via the cumulative effect of sputtering in dynamic SIMS. MALDI is performed by irradiating a matrix-coated sample with a laser; spatial resolution is determined by matrix crystallization and laser wavelength. MALDI-MS, specifically coupled to time-of-flight mass analyzers, has been used extensively for MS imaging. MALDI has been very successful in the analysis of proteins and lipids due to softer ionization (i.e. imparting less thermal energy into molecular bonds and thereby avoiding ion fragmentation) than SIMS, but cannot achieve the same spatial resolution. The spatial resolution in DESI is limited initially by size of the emitted droplets and later by the size of the thin-film which develops on the surface – the size of the thin-film is determined by surface wetting and the angle of incidence of impinging droplets. DESI-MS imaging (DESI-MSI) is commonly performed in a line-by-line fashion by continuously scanning the DESI spot (i.e. area covered by the thin-film) laterally across the sample in the x-dimension, and then stepping a defined distance in the y-dimension, repeatedly. When performed under ambient conditions has significant advantages over other MS imaging techniques which the full scan mode, every MS image pixel contains a mass spectrum that spans a user defined *m/z* range of a single ionization mode (i.e. positive or negative). The ability to analyze samples require the sample to be inserted into vacuum (e.g. SIMS) or pretreatment of samples (e.g. MALDI), particularly in the growing area of clinical MS imaging.

1.3 Ambient Ionization – Mass Spectrometry in Medicine

Diagnosis is an essential facet in medicine. Ambient ionization - MS is applicable in a number of areas of diagnostic medicine, notably point-of-care clinical measurements, pathology, and surgery. (24, 25) The aforementioned areas have unique questions and desired performance criteria; therefore, the tools and methods by which the questions are addressed are slightly different. Point-of-care measurements are generally simple (e.g. one analyte) but need be made quickly, typically at a cost in confidence. Pathology requires significantly more detailed information obtained via tissue biopsy and genetic testing, generally at the expense of time. Surgery seeks to answer simple diagnostic questions (e.g. “is this cancerous or not”) but contends with much more difficult practical questions, “what is the relative good, compared to harm, in surgically removing tissue.” Ambient ionization – MS has the potential to assist in the molecular diagnosis in all cases, leveraging mass spectrometry’s sensitivity and molecular specificity, and improve patient care via rapid chemical measurement. The latter two cases, pathology and surgery, have been the major focus of my dissertation research.

There exists a large body of scientific work demonstrating that ambient ionization – MS is capable of acquiring chemical information that differentiates between normal and cancerous tissue. Numerous ambient ionization methods have been used to analyze tissue in MS imaging and non-imaging modes including DESI, rapid evaporative ionization (REIMS), (26) PESI, and others. These studies have identified specific molecules (e.g. N-acetyl-aspartic acid in gliomas (27) as well as patterns of ions and their relative MS abundance (i.e. profiles) as potential biomarkers. Lipid profiles, a pattern of fatty acids and phospholipids, and multivariate statistics have been used to provide differentiation in human cancers of the brain, (27-29) kidney, (30, 31) liver, (32) prostate, (33, 34) breast, (35) stomach, (36) and others – primarily by DESI-MS imaging of frozen tissue sections. Advancement of these in vitro studies into clinical use is currently ongoing with intrasurgical assessment of cancer being a major focus. Two schools of thought have emerged – involving either online or offline measurements. (25) The online approach aims to integrate ambient ionization with current medical devices, such as the electrocauterization tool in REIMS (also known as the iKnife). Spectra are obtained very rapidly (seconds) with the MS instrument being located directly or closely to the operating room, and can potentially provide predicted disease state, i.e. normal versus cancer, in near real time – initial studies using the iKnife are ongoing at Imperial College. (26) However, the online ambient ionization methods tend to be destructive and do not offer the ability to corroborate predictions by pathology, the gold standard of diagnosis. The offline approach aims to insert MS into the normal pathology workflow, analyzing biopsy tissue immediately within the operating room. Further, the offline methods can be less destructive to tissue morphology/cytology, e.g. DESI-MS using the appropriate solvents, and allow pathologic evaluation post analysis on the same sample. Initial work in translating DESI-MS imaging into the operating room was performed in collaboration with Brigham and Women’s Hospital; (29) however, intrasurgical analysis was never demonstrated. A major part of my dissertation work has been transferring DESI-MS technology and knowledge accumulated in the laboratory into a feasible method for intrasurgical diagnosis of tissue.

1.4 Research Objective

The development of ambient ionization – mass spectrometry for medical measurements, namely intrasurgical cancer detection, was the overarching objective of my dissertation research. The molecular information that differentiated cancer from normal was found in lipid and metabolite profiles, analyzed by multivariate statistics. We sought to acquire the molecular information rapidly within the operating room. Two methods, touch spray and DESI, were developed for this purpose. One advantage of TS is that analysis is greatly simplified by using the same device for in vivo sampling and subsequent ionization. Touch spray is intended for in vivo sampling within surgery to assist in determine the disease state of discrete areas that a surgeon finds suspicious. The TS methodology aligns closely with the online intrasurgical methods, in vivo sampling and rapid analysis (seconds). Human prostate and kidney cancer were used to test the performance of TS-MS. The transition from DESI-MS imaging of sectioned tissue to DESI-MS analysis of tissue smears was a significant development, driven by the time restriction of surgical application. The chemical information obtained from tissue smears were able to equivalently differentiate canine non-Hodgkin’s lymphoma and human brain cancer compared with tissue sections – the traditional sample upon which to perform MS imaging and disease state differentiation. The use of tissue smears for intraoperative analysis falls under the offline intrasurgical analysis, and does not require major modification to current practice. We imagine that intrasurgical MS analysis of smeared biopsy tissue can offer the surgeon reliable pathologic information on a timescale ten times faster than current pathology, which can also be corroborated via standard pathologic evaluation. The culmination of my research is the development and implementation of an intrasurgical DESI-MS analysis method and multivariate classification system for human brain tumors.

1.5 References

1. Ambient Ionization Mass Spectrometry. Domin M, Cody R, editors: Royal Society of Chemistry; 2014.

2. Venter A, Nefliu M, Cooks RG. Ambient desorption ionization mass spectrometry. TrAC Trends in Analytical Chemistry. 2008;27(4):284-90.

3. Takats Z, Wiseman JM, Gologan B, Cooks RG. Mass spectrometry sampling under ambient conditions with desorption electrospray ionization. Science. 2004;306(5695):471-3.

4. Venter AR, Douglass KA, Shelley JT, Hasman G, Honarvar E. Mechanisms of Real-Time, Proximal Sample Processing during Ambient Ionization Mass Spectrometry. Analytical Chemistry. 2014 2014/01/07;86(1):233-49.

5. Badu-Tawiah AK, Eberlin LS, Ouyang Z, Cooks RG. Chemical aspects of the extractive methods of ambient ionization mass spectrometry. Annual review of physical chemistry. 2013;64:481-505.

6. Huang M-Z, Yuan C-H, Cheng S-C, Cho Y-T, Shiea J. Ambient ionization mass spectrometry. Annual review of analytical chemistry. 2010;3:43-65.

7. Costa AB, Cooks RG. Simulated splashes: Elucidating the mechanism of desorption electrospray ionization mass spectrometry. Chemical Physics Letters. 2008;464(1):1-8.

8. Venter A, Sojka PE, Cooks RG. Droplet dynamics and ionization mechanisms in desorption electrospray ionization mass spectrometry. Analytical chemistry. 2006;78(24):8549-55.

9. Hiraoka K, Nishidate K, Mori K, Asakawa D, Suzuki S. Development of probe electrospray using a solid needle. Rapid Communications in Mass Spectrometry. 2007;21(18):3139-44.

10. Kerian KS, Jarmusch AK, Cooks RG. Touch spray mass spectrometry for in situ analysis of complex samples. Analyst. 2014;139(11):2714-20.

11. Wang H, Liu J, Cooks RG, Ouyang Z. Paper spray for direct analysis of complex mixtures using mass spectrometry. Angewandte Chemie. 2010;122(5):889-92.

12. Hu B, So P-K, Chen H, Yao Z-P. Electrospray ionization using wooden tips. Analytical chemistry. 2011;83(21):8201-7.

13. Liu J, Wang H, Cooks RG, Ouyang Z. Leaf spray: direct chemical analysis of plant material and living plants by mass spectrometry. Analytical chemistry. 2011;83(20):7608-13.

14. Jarmusch AK, Pirro V, Kerian KS, Cooks RG. Detection of strep throat causing bacterium directly from medical swabs by touch spray-mass spectrometry. Analyst. 2014;139(19):4785-9.

15. Pirro V, Jarmusch AK, Vincenti M, Cooks RG. Direct drug analysis from oral fluid using medical swab touch spray mass spectrometry. Analytica chimica acta. 2015;861:47-54.

16. Ogihara H, Xie J, Okagaki J, Saji T. Simple method for preparing superhydrophobic paper: spray-deposited hydrophobic silica nanoparticle coatings exhibit high water-repellency and transparency. Langmuir. 2012;28(10):4605-8.

17. van Hove ERA, Smith DF, Heeren RM. A concise review of mass spectrometry imaging. Journal of chromatography A. 2010;1217(25):3946-54.

18. Wiseman JM, Ifa DR, Song Q, Cooks RG. Tissue imaging at atmospheric pressure using desorption electrospray ionization (DESI) mass spectrometry. Angewandte Chemie International Edition. 2006;45(43):7188-92.

19. Brunelle A, Touboul D, Laprévote O. Biological tissue imaging with time-of-flight secondary ion mass spectrometry and cluster ion sources. Journal of Mass Spectrometry. 2005;40(8):985-99.

20. Passarelli MK, Winograd N. Lipid imaging with time-of-flight secondary ion mass spectrometry (ToF-SIMS). Biochimica et Biophysica Acta (BBA)-Molecular and Cell Biology of Lipids. 2011;1811(11):976-90.

21. Caprioli RM. Imaging mass spectrometry: Molecular microscopy for the new age of biology and medicine. Proteomics. 2016.

22. Seeley EH, Caprioli RM. MALDI Imaging Mass Spectrometry. Detection of Chemical, Biological, Radiological and Nuclear Agents for the Prevention of Terrorism: Springer; 2014. p. 99-113.

23. Wiseman JM, Ifa DR, Venter A, Cooks RG. Ambient molecular imaging by desorption electrospray ionization mass spectrometry. Nature Protocols. 2008;3(3):517-24.

24. Ferreira CR, Yannell KE, Jarmusch AK, Pirro V, Ouyang Z, Cooks RG. Ambient Ionization Mass Spectrometry for Point-of-Care Diagnostics and Other Clinical Measurements. Clinical chemistry. 2016;62(1):99-110.

25. Ifa DR, Eberlin LS. Ambient Ionization Mass Spectrometry for Cancer Diagnosis and Surgical Margin Evaluation. Clinical chemistry. 2016;62(1):111-23.

26. Balog J, Sasi-Szabo L, Kinross J, Lewis MR, Muirhead LJ, Veselkov K, et al. Intraoperative tissue identification using rapid evaporative ionization mass spectrometry. Sci Transl Med. 2013 Jul 17;5(194):194ra93. PubMed PMID: 23863833. English.

27. Jarmusch AK, Pirro V, Baird Z, Hattab EM, Cohen-Gadol AA, Cooks RG. Lipid and metabolite profiles of human brain tumors by desorption electrospray ionization-MS. Proceedings of the National Academy of Sciences. 2016:201523306.

28. Eberlin LS, Norton I, Orringer D, Dunn IF, Liu X, Ide JL, et al. Ambient mass spectrometry for the intraoperative molecular diagnosis of human brain tumors. Proceedings of the National Academy of Sciences. 2013;110(5):1611-6.

29. Eberlin LS, Norton I, Dill AL, Golby AJ, Ligon KL, Santagata S, et al. Classifying human brain tumors by lipid imaging with mass spectrometry. Cancer research. 2012;72(3):645-54.

30. Dill AL, Eberlin LS, Zheng C, Costa AB, Ifa DR, Cheng L, et al. Multivariate statistical differentiation of renal cell carcinomas based on lipidomic analysis by ambient ionization imaging mass spectrometry. Analytical and Bioanalytical Chemistry. 2010;398(7-8):2969-78.

31. Alfaro CM, Jarmusch AK, Pirro V, Kerian KS, Masterson TA, Cheng L, et al. Ambient ionization mass spectrometric analysis of human surgical specimens to distinguish renal cell carcinoma from healthy renal tissue. Analytical and Bioanalytical Chemistry. 2016:1-8.

32. Wiseman JM, Puolitaival SM, Takáts Z, Cooks RG, Caprioli RM. Mass spectrometric profiling of intact biological tissue by using desorption electrospray ionization. Angewandte Chemie. 2005;117(43):7256-9.

33. Eberlin LS, Dill AL, Costa AB, Ifa DR, Cheng L, Masterson T, et al. Cholesterol sulfate imaging in human prostate cancer tissue by desorption electrospray ionization mass spectrometry. Analytical chemistry. 2010;82(9):3430-4.

34. Kerian K, Jarmusch A, Pirro V, Koch M, Masterson T, Cheng L, et al. Differentiation of prostate cancer from normal tissue in radical prostatectomy specimens by desorption electrospray ionization and touch spray ionization mass spectrometry. Analyst. 2015;140(4):1090-8.

35. Calligaris D, Caragacianu D, Liu X, Norton I, Thompson CJ, Richardson AL, et al. Application of desorption electrospray ionization mass spectrometry imaging in breast cancer margin analysis. Proceedings of the National Academy of Sciences. 2014;111(42):15184-9.

36. Eberlin LS, Tibshirani RJ, Zhang J, Longacre TA, Berry GJ, Bingham DB, et al. Molecular assessment of surgical-resection margins of gastric cancer by mass-spectrometric imaging. Proceedings of the National Academy of Sciences. 2014;111(7):2436-41.

CHAPTER 2. DEVELOPMENT OF TOUCH SPRAY IONIZATION FOR INTRASURGICAL CANCER DETECTION

2.1 <u>Introduction</u>

Touch spray ionization (TS) was developed explicitly for sampling and analysis in situ.(1) Intrasurgical analysis of tissue during tumor removal is intended to provide surgeons with rapid molecular-based pathologic information in pathologically ambiguous areas. Surgical removal of tumors remains one of the primary treatment options for cancer. We developed and evaluated the ability of TS-MS to detect the chemical changes associated with cancer, namely lipid profiles (i.e. *m/z* values and corresponding MS abundance). Prostate and kidney cancers are of utmost importance as they cause a significant fraction of cancer related fatalities in the United States. Prostate cancer represented ~10.7% (~180,000 cases) of all newly diagnosed cancer cases and there were an estimated 61,560 new cases of kidney cancer, 3.7% of all new cancer cases, in the United States of America in 2016. (2) Histopathology remains the gold standard for diagnosis, and while highly informative, the time required for analysis is generally incompatible with the needs of surgeons. Intrasurgically, surgeons seek a rapid assessment of the disease state, i.e. normal or tumor, of suspicious areas, particularly near the boundary of resection (*i.e.* surgical margin).

Ambient ionization - mass spectrometry (MS) can address this need by making rapid chemical measurements and objective prediction of disease state, i.e. normal versus tumor. Lipids are not currently used as diagnostic markers of cancer but use is growing as well as scientific interest. DESI provides a key connection between the information from histopathology and the characteristic mass spectra of each disease state. DESI-MS can be operated in an imaging mode, collecting mass spectra, pixel by pixel, over two dimensional space to create a 2D molecular image, i.e. ion image. DESI-MS imaging has been previously used to study human prostate (3, 4) and kidney (5, 6) cancers which reported the lipid profiles of normal and cancerous tissue. The analysis of smeared tissue biopsies by DESI-MS, an offline ambient ionization approach to intrasurgical measurement, is useful for intrasurgical measurement of human brain tumors (discussed in later chapters). The intended use of TS-MS is quite different, online intrasurgical measurement; a user-guided method in which a spot of interest is directly sampled with a probe, e.g. teasing needle, and transferred to the interface of a mass spectrometer, and ionized by the application of solvent and high voltage. TS produces information-rich spectra which are similar to DESI, but in a localized and very rapid process which typically takes a few seconds.

2.2 Experimental

2.2.1 Human Subjects

Radical prostatectomy specimens were obtained from consented patients undergoing treatment at Indiana School of Medicine (IUSM) following an Institutional Review Board (IRB) approved study, Indiana University (IU) #1205008669R004 and Purdue University (PU) #1203011967. Biopsies were obtained from specimens after resection using a disposable biopsy gun (Max-core disposable core biopsy instrument, Bard Biopsy Systems, Tempe, AZ). Biopsies (approximately 4-15 mm x 1 mm x 1 mm) were subsequently frozen, cryosectioned at 15 µm, and thaw mounted to glass microscope slides. Sections were stored at -80°C prior to MS analysis. The same slide analyzed by DESI-MS imaging was hematoxylin and eosin (H&E) stained and examined by an expert pathologist. Adjacent sections (separated by ~15 - 60 µm) were analyzed by TS-MS by sampling areas of 1-4 mm^2 from regions of known pathology.

All kidney specimens were acquired from patients undergoing nephrectomy (partial or radical) for the treatment of renal cell carcinoma and were handled in accordance with approved IRB protocols (IU #1205008669R004 and PU #1203011967). A small portion (approximately 3 x 3 x 3 mm) of tumor and adjacent normal kidney tissue (if present) was obtained in the pathology lab (University Hospital, Indianapolis) and analyzed on site using TS-MS. The tumor and normal specimens provided were noted as such by pathology, grossly. TS-MS analysis was performed while the tissue was fresh (not frozen or fixed). Subsequent to TS-MS analysis, the biopsy specimens were snap frozen in liquid nitrogen and transported back to Purdue University on dry ice for DESI-MSI analysis. Specimens were embedded in Optimal Cutting Temperature polymer (Sakura Finetek, Torrance, CA) and sectioned on a cryotome (10 µm thickness) and thaw mounted on glass slides. DESI-MS imaging was performed on the tissue sections. Tissue sections were stained afterwards and evaluated by an expert pathologist – results matched gross pathology in nearly all cases. Specimens were obtained from 21 subjects over the period March 14, 2014 to May 12, 2015. Pathologic evaluation of specimens not included in this study determined the following subtypes for the 21 subjects: 15 clear cell RCC, two papillary RCC, and three unclassified RCC, and one oncocytoma.

2.2.2 Methods

2.2.2.1 DESI-MS Imaging

A laboratory-built DESI ion source, similar to the commercial 2D source from Prosolia, Inc. (Indianapolis, IN, USA) was coupled to a linear ion trap mass spectrometer (LTQ, ThermoFisher Scientific). DESI-MS was performed in the imaging mode, collecting mass spectra over 2D space by coordinating instrument duty cycle with motion stage speed. The negative ionization mode was used collected. Automatic gain control (AGC) was inactivated. The DESI-MS spray solvent was dimethylformamide (DMF)-acetonitrile (ACN) at a 1:1 ratio (v/v), delivered at 1.0 µL/min flow rate using the instrument syringe pump. The use of DMF-ACN (1:1) was used to minimize alteration of tissue morphology

(33). Typical DESI source parameters were used. Prostate and kidney sections were imaged at a lateral spatial resolution of 200 µm and 250 µm, respectively.

2.2.2.2 Touch Spray - MS

TS-MS was performed upon human prostate specimens, frozen and sectioned, at Purdue University. The TS probe used was a commercially available teasing needle purchased from Fisher Scientific (Pittsburgh, PA, USA). Methanol was used as spray solvent and 1.0 µL was applied manually via an adjustable pipette (Eppendorf Research-2.5 µL). A linear ion trap mass spectrometer (LTQ, Thermo) was used for the TS experiments with the same operating parameters as those used in the DESI experiments except that the voltage applied to the TS probe was 4 kV and the automatic gain control was active. TS was performed by touching and desorbing material onto a teasing needle from regions of interest of 1-4 mm^2. After sampling, the tip of the probe was aligned with the inlet of the mass spectrometer, held in place by a ring stand and clamp, and high voltage and solvent were applied. Ions were generated in pulses of signal that were a few seconds in duration. The data acquired within this period were averaged and used for subsequent data analysis. Tissue from an additional 6 subjects was analyzed directly after surgical resection in a research building adjacent to the frozen pathology laboratory in University Hospital. These specimens were analyzed using the same TS methodology but the specimens were not frozen or sectioned.

All kidney specimens were analyzed by TS-MS immediately following resection in a research building adjacent to the frozen pathology laboratory in University Hospital. TS-MS was performed on the fresh (not frozen or fixed) tissue specimens using a metal teasing needle to scrape small amounts of cellular material from the bulk tissue (22). The probe was positioned in front of the mass spectrometer with the metal tip pointing at the inlet (~5-8 mm), a high voltage (4 kV) was applied, and a 1.0 µL aliquot of methanol was added to initiate ionization. Data acquired from a single sampling (touch) were averaged and used for subsequent data analysis.

2.2.2.3 Multivariate Statistics

Principal component analysis (PCA), using the non-linear iterative partial least squares algorithm, was performed on the TS-MS and DESI-MSI data using MATLAB (MathWorks, Natick, MA) and in-house routines which were described in previous work. (3, 5) Data were normalized using standard normal variate (SNV) transform to correct for baseline shifts and global variation in signal intensities, and then mean-centered prior to PCA. Linear discriminant analysis (LDA) was performed in MATLAB on the PCA compressed data (i.e. PCA-LDA) to discriminate between disease states (i.e. normal versus tumor). PCA-LDA models were validated via cross validation using five deletion groups.

2.3 Results and Discussion

2.3.1 TS-MS Analysis of Mouse Brain Tissue

The lipid profiles of brain tissue have been extensively studied using ambient ionization - mass spectrometry, i.e. DESI, (7-9) which therefore constitutes a biological standard by which to qualitatively measure the performance of TS. A minute amount of cellular and extracellular material was transferred to a TS probe using light abrasive force on the biological material. For the sake of demonstration, mouse brain tissue sections were sampled in this manner removing material in a circle (diameter <1 mm). TS mass spectra, negative ion mode, displayed in Figure 2-1 are similar to those acquired with DESI from the same region. The spectra are dominated by signals due to fatty acids (*m/z* <300), fatty acid dimers (*m/z* 300-700), and glycerophospholipids (*m/z* 700-1000). The relative abundances of *m/z* 788.5 (PS 36:1), 834.5 (PS 40:6), 885.5 (PI 38:4), and 888.5 (ST 24:1) were used to qualitatively assess neural composition (white and grey matter). Grey matter and white matter have characteristic peaks of *m/z* 834 and 888, respectively. The transverse plane of mouse brain possesses horizontal symmetry in the stained tissue, visible in the various features stained (e.g. cerebellum and corpus callosum). Touch spray was performed at six positions (Figure 2-1) annotated upon the H&E stain. The TS mass spectra from the mouse olfactory bulb (Figure 2-1, point 1) displayed unique ions detected at *m/z* 806.5 (PS 38:6) and 909.5 (PI 40:6) corresponding to parallel earlier findings using DESI.(7) Similarly, the mass spectra recorded from point 2 indicated an increased percentage of white matter, corresponding to the corpus callosum. The spectra recorded at point 5 reflect a high percentage of gray matter (periaqueductal gray and/or cerebellum). At other points a mixture of gray and white matter was observed with point 3 corresponding to the thalamus, point 4 to periaqueductal gray with white matter potentially from the posterior commissure, and point 6 primarily white matter from the granular layer of the cerebellum with some gray matter. Neuroanatomical location was approximated using the Allen Mouse Brain Atlas. (10)

The reproducibility of touch spray was further assessed using coronal mouse brain sections. These sections are comprised of grey and white matter, reflected in the spectra, whose distribution is symmetrical, vertically, between right and left hemispheres. Touch spray was performed at six equally spaced points across one coronal section (Figure 2-2). Mass spectra were reproducible in terms of the prominent glycerophospholipids ions seen and also in terms of their approximate relative intensities. They were similar between points of related neural composition; for example, A and F indicated grey matter which produces patterns including a base peak at *m/z* 834.5 and major peaks at *m/z* 788.5 and 885.5 whereas B and E displayed greater abundance of *m/z* 888.5 indicating the presence of white matter. Data were collected from all three planes, i.e. coronal, transverse, and sagittal (data not shown) which correctly reflected the correct composition, grey or white matter, based on neuroanatomical location.

2.3.2 Human Prostate Cancer

The potential of TS-MS for prostate cancer differentiation was explored by analyzing radical prostatectomy specimens in vitro, and comparing with DESI-MS results which served as a reference method. Initially, we qualitatively compared the spectra, namely the lipid profiles, that were acquired by each method. The primary components of the prostate lipid profile (negative mode) are glycerophospholipids: phosphotidylethanolamines (PE), phosphotidylserines (PS), phosphotidylcholines (PC), and phosphatidylinositols (PI). Lipids from these classes were observed in the average normal (74 samples) and tumor (26 samples) mass spectra shown in Figure 2-3 for DESI (A and B) and TS (C and D). Spectral differences between normal and tumor were seen in both average DESI and TS spectra, but the spectra from DESI and TS were clearly different from each other. The prostate cancer DESI spectrum (red) appeared to have an increased relative abundance of *m/z* 786, 794, 861, and 863 as well as an altered ratio between *m/z* 788 and 885, relative to the normal (green) DESI spectrum. The prostate cancer TS spectrum (red) also appear to have the same differences as well as variable levels of additional *m/z* values (e.g. *m/z* 737 and 844). Differences in the mass spectra between DESI and TS were also noted, namely the increased abundance of chlorinated adducts of PC lipids (e.g. 794, 820, 844). This observation would suggest that some differences between the ionization methods can be attributed to different tolerance to the salt content in the complex matrix when analyzed with no sample pretreatment - TS has a lower salt tolerance than DESI. This observation is likely due to the differences in extraction and desorption operations of the two methods. Extraction in DESI occurs in the thin film of solvent which is subsequently splashed by additional droplet impact, generating ions. Extraction in TS occurs directly into the solvent from which ions are being directly generated. The average ion intensity in TS is two orders of magnitude greater than that in DESI, suggesting that the extraction/desorption process in TS is indeed more direct and short-lived, yielding greater ion current.

2.3.2.1 Multivariate Analysis of DESI-MS and TS-MS Data

Principal component analysis (PCA), an unsupervised multivariate statistical method, was used to comprehensively explore the DESI-MS data. The PCA score plot, shown in Figure 2-4, indicated separation of normal (green) and tumor (red) samples (12 human subjects, 100 samples). The PCA loading plot indicated which ions contributed to the observed separation in the PCA score plot. Linear discriminant analysis was performed subsequent to data compression by PCA and validated by cross validation (Table 2-1) which resulted in a sensitivity, i.e. proportion of samples predicted as positive for the disease among samples that are diseased, and specificity, i.e. proportion of samples known not to be diseased that are predicted as such, of 96.2% and 98.6%, respectively.

The same tissue sections were evaluated by TS-MS, 100 samples from 12 subjects. TS-MS sampling of these samples was targeted, i.e. sampling was performed based on histopathology performed prior to MS analysis. This was the initial step in exploring if TS-MS was able to detect the same chemical information as DESI and if that chemical information was able to separate normal from tumor samples. The TS-MS data were analyzed by PCA which resulted in the separation of normal (green) and tumor (red) in Figure 2-5. The corresponding PCA loading plot indicated important ions in making that distinction. PCA-LDA cross validation, Table 2.2, yielded a sensitivity of 88.5% and specificity of 98.6%.

2.3.3 Human Kidney Cancer

TS-MS study of prostate cancer provided the first evidence that chemical information indicative of disease state could be obtained; however, that study was performed on frozen tissue sections which does not accurately emulate intrasurgical material. TS-MS was used to study healthy renal tissue and kidney cancer, i.e. renal cell carcinoma (RCC), specimens immediately following resection. Lipid profiles were collected and evaluated for their ability to distinguish disease state as an initial step towards analyzing, intrasurgically, discrete areas of pathologic ambiguity. TS-MS analysis was performed on the Indiana University medical campus immediately after resection, in a research building (R3) adjacent to the frozen pathology lab at University Hospital. Tissue was fresh (not frozen or fixed) and contained biofluids (e.g. blood). TS-MS was performed by sampling a small area of the biopsies (multiple times for some samples), many sampling events contained some amount of blood. Subsequent to TS-MS analysis, the biopsy specimens were snap frozen in liquid nitrogen for DESI-MS imaging (DESI-MSI). DESI-MSI was performed to complement TS-MS results. The solvent used for DESI-MS imaging preserves tissue morphology and allowed subsequent staining of the same tissue, improving correlation with histopathologic evaluation. (11) Previous DESI-MS imaging studies of RCC in the negative ionization mode indicated the ability to differentiate RCC and healthy renal tissue with multivariate statistics. (6)

2.3.3.1 Differentiation of Healthy and Renal Cell Carcinoma by Touch Spray – MS and Comparison with DESI-MS

Principal component analysis (PCA) was performed on TS-MS data. The PCA score and loading plots are shown in Figure 2-6. Separation between RCC (red) and healthy renal tissue (blue) is observed in the score plot. Differences in *m/z* abundances are apparent in the average mass spectra of healthy renal tissue and RCC. Healthy renal tissue gives more abundant ions *m/z* 794 and 792 (tentatively identified as chlorinated adducts of PC 34:1 and PC 34:2, respectively), and *m/z* 844 and 885 (tentatively identified as chlorinated PC 38:4 and deprotonated PI 38:4, respectively) is relatively more abundant in RCC. Cross validation of a discriminant model, linear discriminant analysis (LDA) on the PCA compressed data, was performed. The sensitivity was 96.1% and specificity was 98.1% using five deletion groups and five principal components, Table 2-3. While these results are encouraging, a larger sample size is required to validate the method's diagnostic capabilities. Note, histopathologic subtypes of the specimens were provided by pathology performed on independent samples; however, the number of samples in each subtype was too small to comment on the ability of TS-MS to delineate RCC subtypes.

PCA of the DESI-MS data (i.e. regions of interest, ROI) provided similar results to TS but slightly better separation in the PCA score plot (Figure 2-7). Cross validation (five deletion groups) was performed on the DESI PCA-LDA model. The sensitivity was 100% and specificity was 86.7% using three principal components, Table 2-4. The DESI-MS spectra, Figure 2-7, were visually different than the TS-MS spectra (Figure 2-6); however, differences between normal and RCC were still present – an observation similar to that of TS and DESI analysis of prostate cancer tissue. The major difference between the spectra were the relative abundance of chlorinated adducts – more abundant in TS than in DESI. (1) The difference in abundance can be attributed simply to differences in ionization mechanisms, increased biofluid content of fresh renal tissue for the fresh tissue analyzed by TS-MS, and perhaps to the use of different spray solvents (methanol for TS and 1:1 DMF-ACN for DESI). The differences observed suggest that both DESI and TS could be used for differentiating normal from tumor; however, each will require the development of their own respective spectral databases.

2.4 Conclusions

TS-MS is envisioned as an online ambient ionization – MS surgical tool for rapid disease state determination in areas of interest. As a surgical screening tool, TS could help preserve healthy tissue that may have otherwise been resected for histopathological evaluation or help with decisions to remove additional diseased tissue, the state of which was questionable. One alternative online approach would be the analysis of smeared tissue by DESI-MS, but in vivo sampling is not possible. One important feature of TS is that the means of sampling and ionization are incorporated into a single device. This allows for very rapid sampling and immediate analysis without sample preparation or chromatographic separation. Mouse brain tissue served as a model system by which to demonstration the ability for TS-MS methodology to obtain lipid profiles reproducibly and faithfully reproduce the lipid profiles of normal grey and white matter.

The first step in developing this surgical tool was applying TS-MS to prostate cancer, analyzing frozen tissue sections in parallel with DESI-MS. Differentiation of normal and prostate cancer samples was obtained with a targeted TS dataset; sensitivity and specificity of 88.5% and 98.6%, respectively. The next step toward intrasurgical use was analyzing fresh tissue ex vivo by TS-MS, healthy renal tissue and RCC were analyzed directly after surgical resection. The ex vivo analysis provided very similar conditions to those expected in surgery, e.g. presence of biofluids and unaltered tissue. The sensitivity of the TS-MS method for predicting RCC was 96.1% and the specificity was 98.1%. DESI-MS was performed after TS-MS on the same specimens and provided a similar sensitivity (100%) but worse specificity (86.7%). The analysis of prostate and kidney cancer illustrated that TS-MS can provide sufficient diagnostic information via lipid profiles and multivariate statistics. The most notable differences observed were the increased presence of chlorinated PCs in the TS-MS data, e.g. *m/z* 794 ($[\mathrm{PC}\ 34{:}1 + \mathrm{Cl}]^-$). The tolerance of TS-MS to salts is likely less than that of DESI due to differences in desorption and ionization mechanism as well as potential differences between the spray solvents for each method. Regardless, the chemical information obtained by each method, independently, was able to distinguish normal from tumor. The applicability of the technique is likely not exclusive to the cancers studied here, and could be useful in the surgical treatment of different cancers and diseases. In addition, refinements to the TS-MS methodology should be pursued to increase the ruggedness, ease of use, and reproducibility of the measurements.

2.5 Acknowledgements

I would like to acknowledge the researchers at Purdue who contributed to this work: Dr. R. Graham Cooks, Dr. Valentina Pirro, and Dr. Kevin S. Kerian. Thank you all for your assistance in developing touch spray ionization and the prostate and kidney cancer studies – it was truly a team effort. Second, I would like to acknowledge the team of physicians. The surgeons, particularly Dr. Timothy A. Masterson, were invaluable, providing specimens for research and their expert opinions. Dr. Liang Cheng, our pathologist, is also owed thanks for evaluating a large number of specimens and providing crucial insight into pathology.

2.6 References

1. Kerian KS, Jarmusch AK, Cooks RG. Touch spray mass spectrometry for in situ analysis of complex samples. Analyst. 2014;139(11):2714-20.

2. National Cancer Institute - SEER Fact Sheet [cited 2016 July 19]. Available from: http://seer.cancer.gov/statfacts/.

3. Kerian K, Jarmusch A, Pirro V, Koch M, Masterson T, Cheng L, et al. Differentiation of prostate cancer from normal tissue in radical prostatectomy specimens by desorption electrospray ionization and touch spray ionization mass spectrometry. Analyst. 2015;140(4):1090-8.

4. Eberlin LS, Dill AL, Costa AB, Ifa DR, Cheng L, Masterson T, et al. Cholesterol sulfate imaging in human prostate cancer tissue by desorption electrospray ionization mass spectrometry. Analytical chemistry. 2010;82(9):3430-4.

5. Alfaro CM, Jarmusch AK, Pirro V, Kerian KS, Masterson TA, Cheng L, et al. Ambient ionization mass spectrometric analysis of human surgical specimens to distinguish renal cell carcinoma from healthy renal tissue. Analytical and Bioanalytical Chemistry. 2016:1-8.

6. Dill AL, Eberlin LS, Zheng C, Costa AB, Ifa DR, Cheng L, et al. Multivariate statistical differentiation of renal cell carcinomas based on lipidomic analysis by ambient ionization imaging mass spectrometry. Analytical and Bioanalytical Chemistry. 2010;398(7-8):2969-78.

7. Eberlin LS, Ifa DR, Wu C, Cooks RG. Three-Dimensional Vizualization of Mouse Brain by Lipid Analysis Using Ambient Ionization Mass Spectrometry. Angewandte Chemie International Edition. 2010;49(5):873-6.

8. Eberlin LS, Ferreira CR, Dill AL, Ifa DR, Cooks RG. Desorption electrospray ionization mass spectrometry for lipid characterization and biological tissue imaging. Biochimica et Biophysica Acta (BBA)-Molecular and Cell Biology of Lipids. 2011;1811(11):946-60.

9. Jarmusch AK, Pirro V, Baird Z, Hattab EM, Cohen-Gadol AA, Cooks RG. Lipid and metabolite profiles of human brain tumors by desorption electrospray ionization-MS. Proceedings of the National Academy of Sciences. 2016:201523306.

10. Allen Mouse Brain Atlas. Available from: http://mouse.brain-map.org/static/atlas.

11. Eberlin LS, Ferreira CR, Dill AL, Ifa DR, Cheng L, Cooks RG. Nondestructive, histologically compatible tissue imaging by desorption electrospray ionization mass spectrometry. ChemBioChem. 2011;12(14):2129-32.

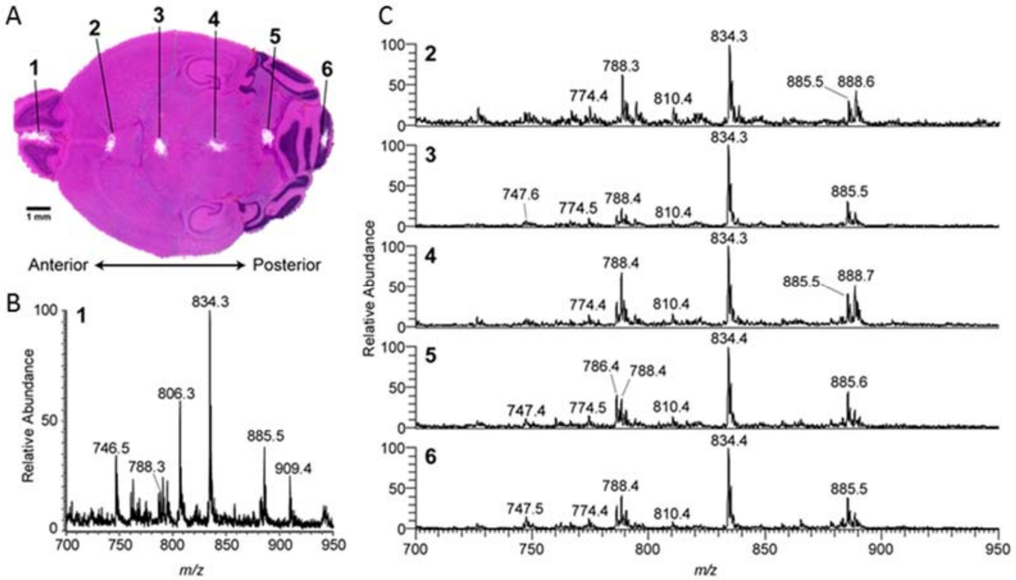

Figure 2-1 (A) Transverse mouse brain tissue section (H&E stained) with discrete TS-MS sampling areas annotated. (B) TS-MS spectrum of sampling area 1, corresponding to the olfactory bulb, which contains the unique ion *m/z* 909.4. (C) TS-MS spectra of sampling areas 2-6.

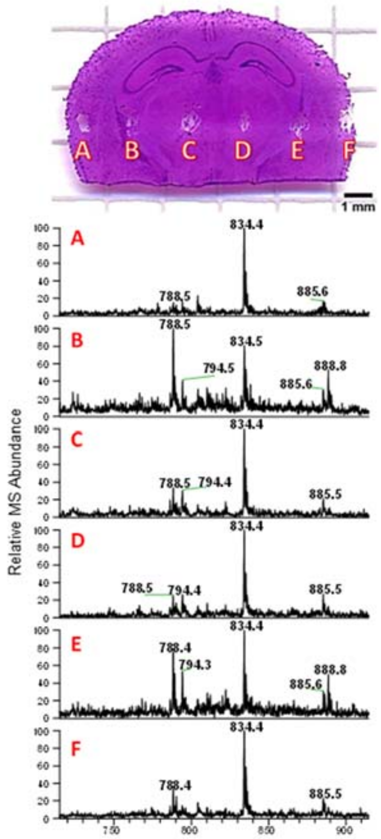

Figure 2-2 Coronal mouse brain tissue section, H&E stained, with sampling points, A-F, annotated. Mass spectra corresponding to the sampling points, A-F, are included with major ions annotated.

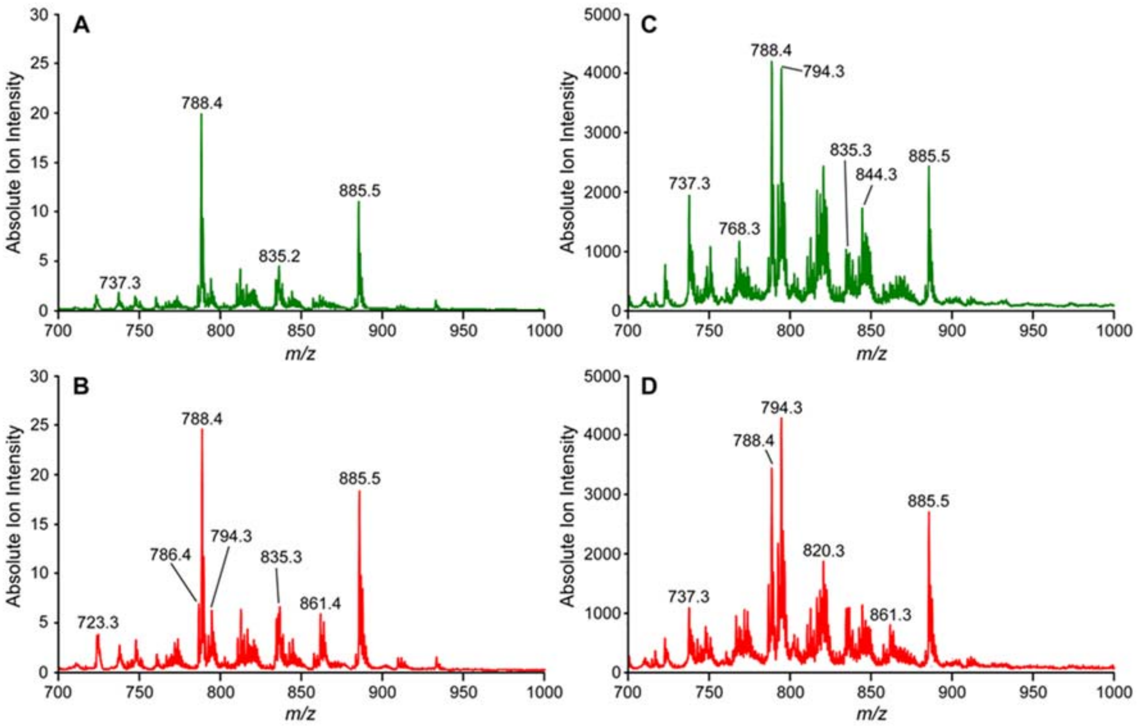

Figure 2-3 (A) Average DESI-MS spectrum, *m/z* 700 – 1000, for normal human prostate and (B) average DESI-MS spectrum of human prostate cancer. (C) Average TS-MS spectrum for normal human prostate and (D) average TS-MS spectrum of human prostate cancer.

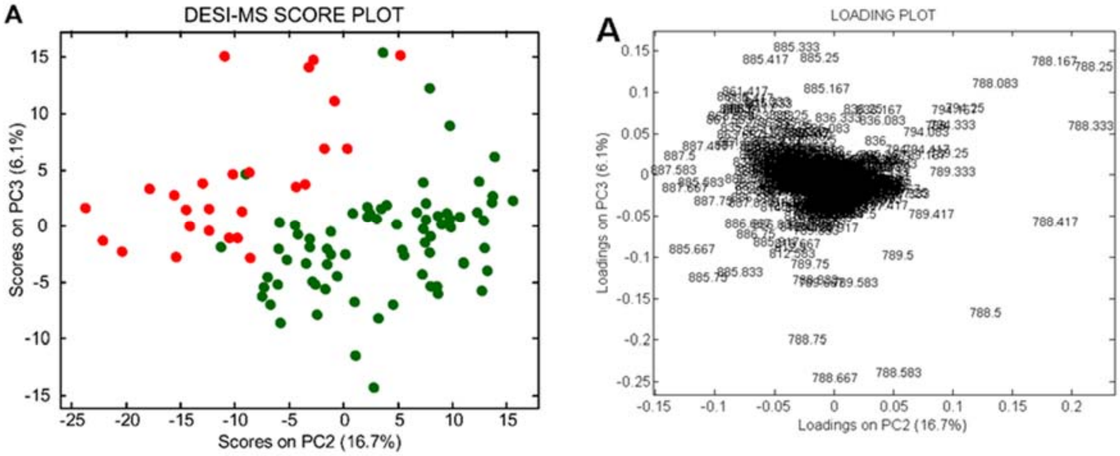

Figure 2-4 (A) DESI-MS PCA score plot for normal human prostate (green) and human prostate cancer (red). (B) PCA loading plot with *m/z* values annotated.

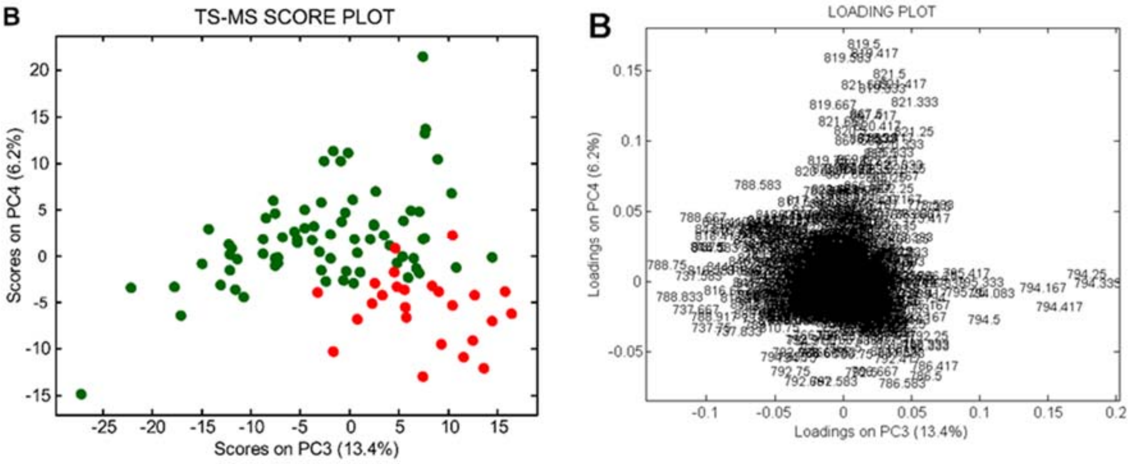

Figure 2-5 (A) PCA score plot for TS-MS analysis of normal human prostate (green) and human prostate cancer (red). (B) PCA loading plot for TS-MS data with *m/z* annotated.

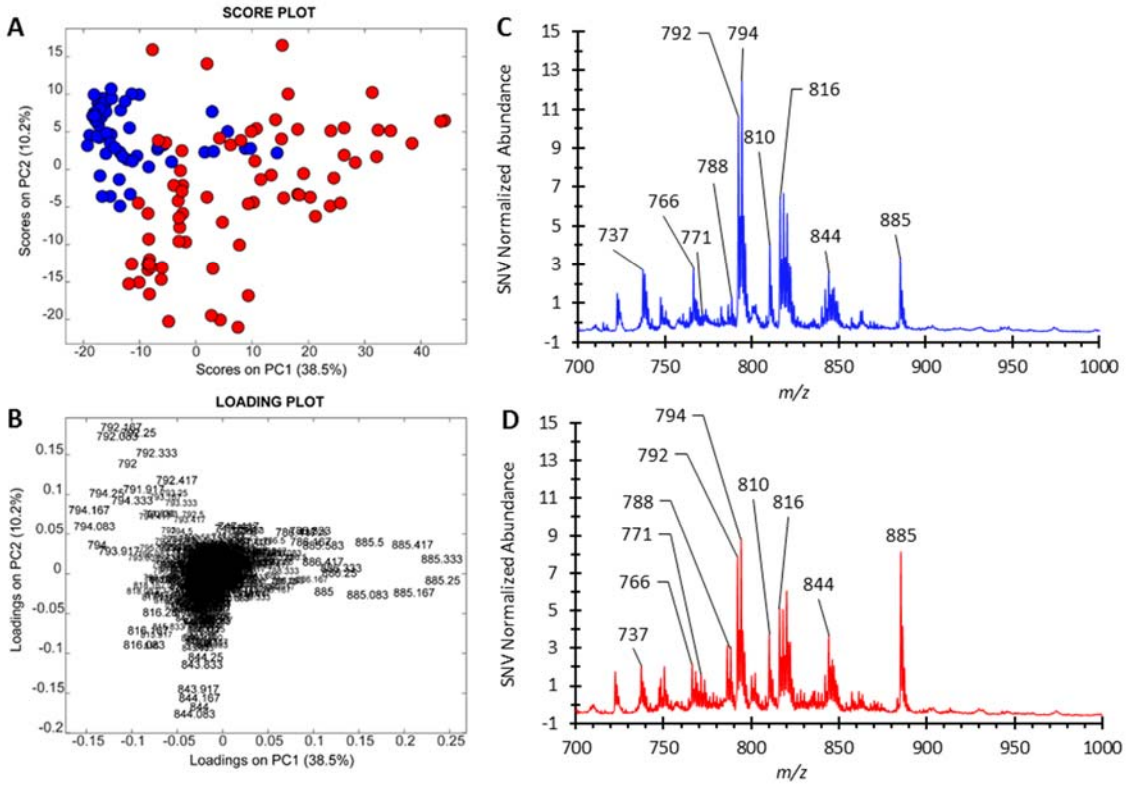

Figure 2-6 (A) PCA score plot for TS-MS data, normal (blue) and human kidney cancer (red). (B) PCA loading plot with *m/z* annotated. (C) Average TS-MS spectrum, *m/z* 700 – 1000, of normal human renal tissue and (D) average TS-MS spectrum for human kidney cancer.

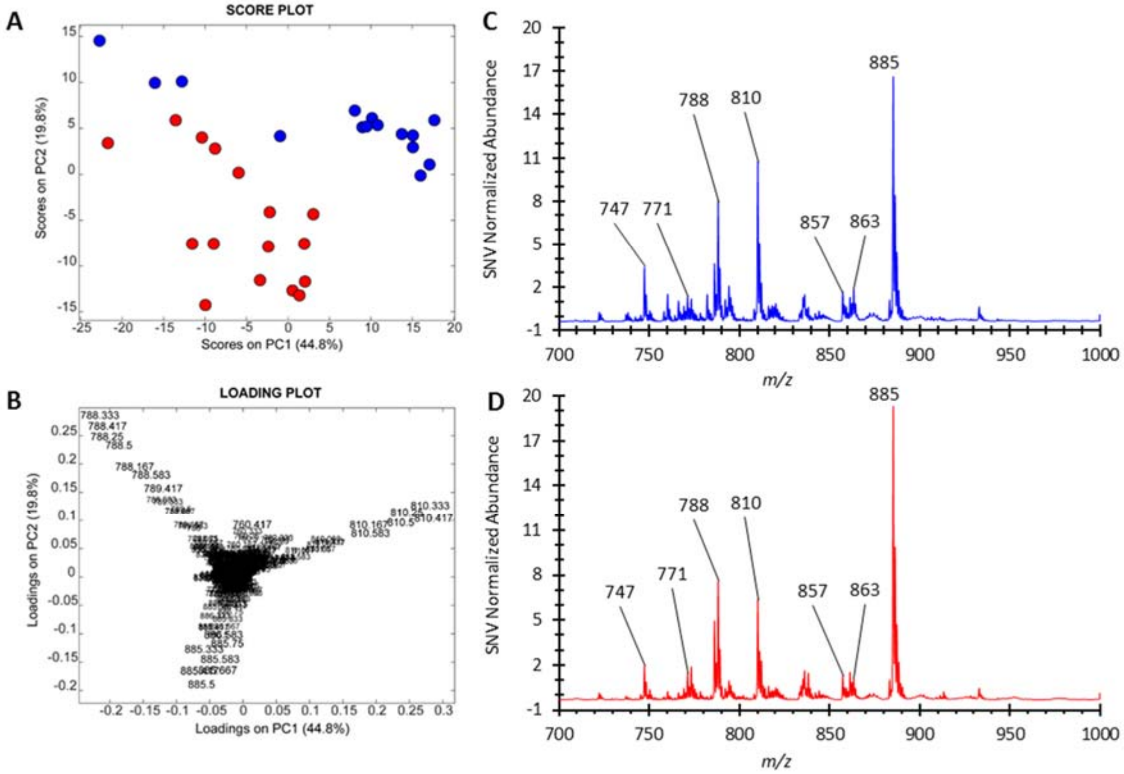

Figure 2-7 (A) PCA score plot for DESI-MS data, normal (blue) and human kidney cancer (red). (B) PCA loading plot with *m/z* annotated. (C) Average DESI-MS spectrum *m/z* 700 – 1000, of normal human renal tissue and (D) average DESI-MS spectrum for human kidney cancer.

Table 2-1 DESI-MS PCA-LDA cross validation confusion matrix for human prostate cancer (tumor) and normal.

		DESI Prediction	
		Tumor	Normal
Pathology	Tumor	25	1
	Normal	1	73

Table 2-2 Targeted TS-MS PCA-LDA cross validation confusion matrix for human prostate cancer (tumor) and normal.

		TS Prediction	
		Tumor	Normal
Pathology	Tumor	23	3
	Normal	1	73

Table 2-3 TS-MS PCA-LDA confusion matrix for human kidney cancer (tumor) and normal.

		TS Prediction	
		Tumor	Normal
Pathology	Tumor	73	3
	Normal	1	53

Table 2-4 DESI-MS PCA-LDA confusion matrix for human kidney cancer (tumor) and normal.

		DESI Prediction	
		Tumor	Normal
Pathology	Tumor	16	0
	Normal	2	13

CHAPTER 3. CHARACTERISTIC LIPID PROFILES OF CANINE NON-HODGKIN'S LYMPHOMA FROM SURGCIAL BIOPSY TISSUE SECTIONS AND FINE NEEDLE ASPIRATE SMEARS BY DESI-MS

3.1 Introduction

Non-Hodgkin's lymphoma (NHL) is a diverse group of cancers, afflicting canines and humans. Rates of NHL in canines exceed that in humans; (1) nevertheless, NHL accounts for ~4.3% of all new cancers in the United States resulting in an estimated 72,500 deaths in 2016. (2) NHL can be broadly defined into two subgroups, B-cell and T-cell, correlated to the lymphocyte immunophenotypes from which the cancer originated; there are many further subtypes within B-cell and T-cell NHL. B-cell lymphomas are the more common of the two, particularly diffuse large B-cell lymphoma, thus they are the primary focus of this study. Canine lymphoma is currently being considered as a meaningful comparative model for human NHL, while important in its own right. (1, 3)

The gold standard for diagnosis of NHL is histopathological evaluation of surgically removed lymph node (whole or in part) via tissue sections, which is commonly supported by immunohistochemistry. Histopathological diagnosis is based on morphological and cytological features, such as morphological growth pattern, nuclear size and shape, and mitotic index. (4, 5) A less invasive alternative to surgical biopsy is fine needle aspirate (FNA) biopsy, performed using a hypodermic needle that is inserted into a suspicious lymph node. A small amount of cellular material is removed, expelled onto a microscope slide, and smeared to form a cellular monolayer which may be evaluated using light microscopy following cytochemical or immunocytochemical staining. Smaller sample size and destruction of nodal architecture, a result of FNA sampling and smearing, can result in higher rates of false negatives and inconclusive diagnoses compared to tissue sections.(6) FNA does have advantages over surgical biopsy and histopathology, in that it is less expensive, less invasive, and less technically demanding.(7, 8) Both canines and humans with NHL may be significantly debilitated at the time of initial cancer diagnosis, and a minimally invasive diagnostic technique may be better suited to these patients than surgical biopsy.

A promising method for improving the diagnostic yield of FNA biopsies is desorption electrospray ionization – mass spectrometry (DESI-MS), an ambient ionization technique which allows for chemical analysis of surfaces, including tissue sections and tissue smears, at native atmospheric conditions (temperature, pressure, and humidity). The mechanism of analyte desorption and ion generation has been extensively studied. (9, 10) DESI-MS imaging of tissue sections has been applied previously in canine bladder cancer (11) and human cancers, including those of the liver, (12) brain, (13, 14) kidney, (15) bladder, (16) and other organs. (15, 17) Further, DESI-MS has been applied to human brain tissue smears which are similar to FNA smears, e.g. used for rapid analysis. Tissue smears, another alternative to tissue sectioning, differ from fine-needle aspirate on the method of collection (needle biopsy versus incisional/excisional biopsy) and the consistency of the cellular material – the latter tends to be more aqueous and contain a suspension of cells. Analysis of tissue smears allowed differentiation of normal brain tissue and gliomas (14) and has been implemented for intrasurgical analysis, discussed later in this dissertation.

The analysis of lipids that compose cells, structurally and functionally, and tissue has been the focus of the previously mentioned studies, allowing for differentiation of cancer from normal tissue without exception. The lipid profile varies with cell metabolism and signaling and is indicative of disease state. The use of multivariate statistics for pattern recognition, such as principal component analysis (PCA) followed by supervised classification techniques (e.g. linear discriminant analysis, LDA), allowed visualization and classification of differences between samples and complex relationships within large datasets.

The characteristic endogenous lipids using DESI-MS from surgical biopsy tissue sections and FNA smears for disease state differentiation (i.e. normal vs. tumor) in canine NHL was explored. DESI-MS imaging of tissue sections detected lipid profiles indicative of disease state, which established a data set with which to compare FNA smears. The characteristic lipid profiles obtained from surgical biopsies and FNAs corroborate histopathology and cytology while providing unique chemical insight. Comparison between previous data regarding the significant lipids in human NHL and this canine study provide molecular support for a canine comparative model.

3.2 Experimental

3.2.1 Materials

Specimens were provided by the College of Veterinary Medicine, Purdue University. All NHL specimens were collected from pet dogs presented to the Purdue University Veterinary Teaching Hospital (PUVTH) for medical treatment of their cancer. At the time of presentation, fine needle aspirate samples were collected from an affected lymph node in each dog using a 22-gauge hypodermic needle. FNA samples were expelled onto glass slides, allowed to air dry, and then stored at -80^{o}C until the time of DESI-MS analysis. Immediately following FNA, all dogs with NHL underwent surgical biopsy of the same affected peripheral lymph node. A portion of each biopsy was fixed in 10% neutral buffered formalin and submitted for histopathologic confirmation of NHL. The residual portion of each dog's lymph node biopsy was snap frozen in liquid nitrogen, and the samples were stored at -80oC until the time of DESI-MS analysis. Lymph node samples from healthy, purpose-bred research dogs served as normal controls. All control animals had been humanely euthanatized as part of an academic laboratory course within the Purdue College of Veterinary Medicine Doctor of Veterinary Medicine degree curriculum. Surgical lymph node biopsy and FNA samples of peripheral lymph nodes were collected immediately post-mortem from all control animals in identical fashion to that described for pet dogs with NHL. All lymph nodes from control animals were confirmed to be histologically normal following light microscopic review of H&E stained sections from formalin-fixed tissues by a board-certified veterinary pathologist. All medical and surgical procedures conducted on both control animals and pet dogs were approved by the Purdue Animal Care and Use Committee (1111000308 and 1211000780).

3.2.2 Methods

3.2.2.1 DESI-MS Analysis

Frozen surgical biopsy specimens were cryosectioned at 15µm thickness using a Cryotome FSE (Thermo, Waltham, MA, USA) and thaw mounted on glass microscope slides (Gold Seal Rite-On Microscope Slides, Thermo). Prior to analysis, the slides were allowed to come to room temperature and briefly dried using an electronic desiccator (VWR, Desi-Vac Container, Radnor, PA, USA) for approximately 10 minutes to remove any frozen condensation resulting from storage. FNA smears were also dried for ~10 minutes prior to analysis, for the same reason, and analyzed under the same conditions. Normal and tumor samples were randomized over multiple days of analysis, surgical biopsy tissue sections and specimen matched FNA were analyzed on the same day. DESI-MS was performed using a lab built prototype ionization source coupled to a linear ion trap mass spectrometer (LTQ, Thermo). DESI-MS was carried out in the negative ion mode using equal parts dimethylformamide (DMF) and acetonitrile (ACN), preserving tissue morphology and allowing subsequent histopathology to be performed on the analyzed tissue section. (18) DESI analysis was performed using the following major parameters: automatic gain control (AGC) off, maximum ion injection time of 250 ms with 2 microscans, 5 kV spray voltage, 180 PSI N_2 (gas), incident spray angle was 52˚, capillary temperature of 275°C, spray-to-surface distance ~2 mm, and spray-to-MS inlet distance ~8 mm. Identical DESI-MS conditions were used to acquire high resolution mass spectrometry data on an orbitrap mass spectrometer (Exactive, Thermo). HRMS was interpreted using XCalibur and monoisotopic formulae masses were calculated in Isopro3. Sample slides were analyzed by securing them to the moving stage. The MS scan rate was coordinated with the moving stage speed in the "x" dimension (i.e. rows), defining resolution (200 µm). Upon the completion of each row, the moving stage was stepped vertically in 200 µm increments defining the "y" resolution. The typical time required for DESI imaging of a tissue section was less than 20 minutes. Illustrative is specimen 42, ~20 min, with an imaging area approximately 8.4 mm (width) by 7.6 mm (height), including the entirety of the tissue section roughly 6.2 mm (width) by 5.8 mm (height) in dimension.

3.2.2.2 Pathology

Histopathologic review, with tumor subtyping according to World Health Organization criteria, (4) was performed on formalin-fixed lymph node tissue sections as part of routine clinical diagnosis. The clinical diagnosis was used for DESI-MS data correlation. Samples demonstrating spatially heterogeneous chemical features were evaluated post DESI-MS analysis and annotated by histopathologic review of frozen tissue sections. There were no cases in which histopathology review differed between frozen and formalin-fixed tissue sections. The annotated regions were used to define areas associated with non-malignant morphological features, unless otherwise noted. Subsequent to DESI-MS analysis, all FNA slides were stained with Wright's stain and evaluated by light microscopy. FNA slides were reviewed by an expert veterinary cytopathologist, who interpreted the nature of the sample (i.e. lymphoma vs. non-lymphoma), the distribution of cells within the sample (i.e. homogenous vs. heterogeneous distribution of cellular material within the smear), the density of cells within the sample (i.e. densely cellular vs. sparsely cellular), and whether significant red blood cell contamination of the sample was present.

3.2.2.3 Data Analysis

Surgical biopsy and FNA smear data acquired using XCalibur 2.0 (.raw) were converted with an in-house program into files compatible with BioMap software. BioMap was used to generate 2D ion images (retaining spatial relationships and displaying relative mass spectral abundance of particular mass-to-charge ratios), select regions of interest (ROI) based on pathology, and export data for multivariate analysis. An in-house MatLab (MathWorks, Inc., Natick, MA, USA) routine was used to explore chemical features present in two dimensional DESI ion images. PCA was performed upon MS hyperspectral datacubes, the composite of spatial dimension ("x" and "y"), *m/z* value, and corresponding *m/z* intensity, and plotted using an interactive brushing procedure,(19) see Supplemental information for more details.

PCA was used to explore DESI-MS data and visualize the grouping of samples resulting from chemical similarity.(20) Multivariate analysis of tissue sections was performed using in-house MatLab routines. The mass range was truncated (*m/z* 700-1000) for statistics, as it was empirically found to contain less analytical variability, providing more consistent and clear separation with regards to disease state (i.e. normal vs. tumor). Two specimens were excluded from statistics: one lymphoma sample (due to poor MS signal) and a metastatic carcinoma. MS data were normalized by the total ion current (TIC) and column-centered (i.e. mean-centered). Neither background subtraction nor a smoothing algorithm was applied to the MS data before PCA. LDA was performed for discriminant classification after unsupervised data compression by PCA (i.e. PCA-LDA), as reported elsewhere. (21) The first 8 principal components (PCs), accounting for ~90% of total data variation, were used. Classification rates report the correct classification of samples in the final PCA-LDA model. Cross validation (CV) with 5 deletion groups was used to test the prediction ability, reported as CV sensitivity and specificity. Sensitivity was calculated as the percent of the objects in the evaluation sets correctly accepted by the model. Specificity was calculated as the percent of the objects of other categories correctly rejected by the model. Average DESI mass spectra obtained from FNA smears were compared with those of surgical biopsy via multivariate statistics. A linear discriminant model (i.e. PCA-LDA) was built in PARVUS (University of Genova, Italy) using mass spectra from surgical biopsy tissue sections, to which FNA smear mass spectra were classified. The results and prediction rates are tabulated.

3.3 Results and Discussion

3.3.1 DESI-MS Imaging of Lymph Node Tissue Sections

Surgically excised lymph node biopsies were sectioned and analyzed by DESI-MS imaging, providing chemical and spatial information concurrently. The methodology employed follows that of histopathological evaluation of tissue, while providing molecular information. Tissue diagnosis by DESI-MS is performed with a spatial resolution larger than traditional histopathology (hundreds of microns versus tens of microns); however, it provides chemical information otherwise unobtainable by traditional histopathology. DESI-MS analysis of tissue sections aims to explore and establish the lipid profiles indicative of normal and NHL tumor subtypes. Negative mode DESI mass spectra showed ionized fatty acids (e.g. oleic acid, *m/z* 281), fatty acid dimers, and glycerophospholipids from *m/z* 700 - 1000 (e.g. PI 38:4, *m/z* 885). The major glycerophospholipids (GPL) ions observed included major structural and signaling lipid classes: phosphatidylinositols (PI), phosphatidylserines (PS), phosphatidylethanolamines (PE), and phosphatidylglycerols (PG). Tentative identification of the ions were made using high resolution mass measurements, Table 3-1, and tandem MS (data not shown). The majority of lymphoma-containing tissue sections displayed a conserved pattern of lipids (i.e. ion, *m/z*, and corresponding relative abundance), or lipid profile, that contrasted markedly with that of normal tissue, and varied more slightly between B-cell and T-cell subtypes. Minute analytical variances in the lipid profile and signal intensity were attributed to freezing and sectioning artifacts. These small areas contributed insignificantly upon averaging and did not compromise the ability to ascertain MS information.

DESI-MS ion images, two dimensional spatial distribution of *m/z* versus the corresponding ion abundance represented in false-color, revealed the majority of samples to be chemically homogenous, i.e. to have similar lipid profiles. Diffuse large B-cell lymphoma, Figure 3-1, was particularly homogenous, spatially and chemically, following the propensity of this cancer to diffusely obliterate normal lymph node architecture. Normal samples were also relatively homogenous in regards to chemical composition and spatial distribution. Interestingly, regions of normal lymph node anatomy, e.g. cortex and medulla, yielded nearly identical lipid profiles although differing in absolute MS intensity. The similarity of the lipid profile was unexpected as anatomical distribution of B-cell and T-cell lymphocytes is known to differ in lymph nodes: B-cells are found in densely packed follicles within the cortex and T-cells are present in the surrounding paracortex. The medulla contains a mixture of plasma cells, macrophages, and T-cells. The absolute MS signal intensity varied between the cortex and medulla, the latter yielded less signal. This intensity difference might result from the anatomical differences between the two regions that are not detected, such as the greater density of blood vessels and vascular sinuses within the lymph node medulla, which reduces the overall cellular density. The spatial resolution of DESI-MS data acquisition used does not allow for such anatomical structures to be visualized. MS imaging at higher resolution (<200 µm), possible by secondary-ion MS, (22) matrix-assisted laser desorption, (23) DESI, (24) and nanoDESI, (25) could visualize these anatomical regions with a non-linear increase in analysis time (analysis time increases with the reciprocal of the square of spatial resolution); however, investigation of normal lymph node anatomy is beyond the scope of the intended application.

Differences in the chemical information within analyzed tissue sections, disregarding previously discussed MS intensity differences, were noted in some of the normal and tumor specimens. In all of these instances (independent of tissue disease state, i.e. normal versus tumor) the difference resulted from the presence of perinodal adipose tissue, as determined by post hoc histopathology. Specimen 31 is illustrative, Figure 3-1 , a tissue section comprised primarily of a B-cell tumor with smaller regions of non-neoplastic, perinodal adipose tissue. The tumor regions have a common lipid profile that is homogenous throughout the tumor region; however, the lipid profile of small regions corresponding to perinodal adipose tissue (outlined) are significantly different and overall lower in absolute intensity as seen in the ion images (particularly *m/z* 281.5). The chemical difference of this region was further explored using PCA and an interactive brushing procedure, see

Figure 3-2. The PCA score plot, displaying each pixel of specimen 31, indicated three groups: B-cell lymphoma associated pixels (red selection), perinodal adipose associated pixels (green selection), and background associated pixels (black). The results of visual interpretation and PCA correlated well with the pathological assessment, considering the differences in spatial resolution of MS imaging and histopathology. Perinodal adipose tissue was also detected in some normal lymph nodes, for example specimen 42, as shown in Figure 3-1. The difference in the lipid profile was again evident between the two tissue types with negative mode GPL signal only noted in the lymph node parenchyma. The lack of GPL signal in adipose tissue is likely correlated to adipocytes (i.e. fat cells), which typically possess a large cytoplasmic volume to GPL membrane surface area ratio. Further, adipocytes contain greater levels of triglycerides and cholesteryl esters which are not readily detected in the negative mode with the solvent conditions chosen; however, previous DESI experiments have detected such compounds in positive ion mode from biological material with relative ease as silver adducts. (26)

3.3.2 Differentiating Lipid Profiles in NHL Tissue Sections

The lipid profiles of tissue sections were explored for molecular-based differentiation of disease state (normal versus tumor) and NHL tumor subtype (i.e. B-cell versus T-cell). The average DESI mass spectrum (from *m/z* 700 - 1000) of normal lymph node (n=22), B-cell lymphoma (n=22), and T-cell lymphoma (n=7) tissue sections, green, blue, and gold respectively, are displayed in Figure 3-3. The ratio of MS abundance of *m/z* 788.3 (PS 36:1), 838.3 (PS 40:4), and 885.5 (PI 38:4) indicated, visually, molecular differences between disease states. Nearly all B-cell samples were diagnosed as diffuse large B-cell lymphoma, differences in the lipid profile are noted in comparison to the average normal spectrum. A small number of T-cell lymphoma tissue sections were analyzed, diagnosed as peripheral T-cell lymphoma, not otherwise specified (n=4) and T-zone lymphoma (n=3). Spectral differences were also noted between normal and T-cell NHL, but the limited number of samples and multiple T-cell subtypes preclude definitive conclusions. Less abundant peaks present in B-cell and T-cell lymphoma also differed in abundance from normal samples including *m/z* 747.4 (PG 34:1), 773.3 (PG 36:2), 786.4, 812.4, 883.5. These ions and their altered relative abundance mirror those reported previously by Eberlin et al. in murine and human lymphoma specimens. (27) One metastatic carcinoma, specimen 12, was analyzed and yielded different lipid profiles from normal and lymphoma with strong alterations in *m/z* 819, 834, 865, and 867 (Figure 3-4). Abbassi-Ghadi and coworkers have previously analyzed metastatic tumors in lymph nodes by DESI, concluding that the chemical information corresponded to that of the primary tumor and had clearly different from adjacent normal lymph node. (28) Extrapolating from that work, the lipid profile of specimen 12 might correlate with that of the primary tumor; however, biopsies of the primary tumor were not available for analysis.

Principal component analysis was performed on the average spectrum of each tissue section, offering an unbiased method for qualitatively assessing the molecular information associated with the pathology-defined condition. Disease state differentiation (normal vs. tumor) was the initial level of diagnostic information explored. Normal lymph node (green) and tumor (red) samples were appropriately grouped as shown in Figure 3-3, panel D. Dispersion of the tumor samples in the PCA score plot, compared with the normal samples, is indicative of greater chemical heterogeneity within lymphoma – matching known diversity of the disease.(1) The dispersion of the lymphoma samples appears to be related to tumor immunophenotype, Figure 3-3, panel E: normal (green), B-cell lymphoma (blue), and T-cell lymphoma (gold). The PCA loading plot, displayed in Figure 3-3, aided in understanding which lipids from *m/z* 700 - 1000 contributed most to PC2 and PC6 computations. Distinguishing NHL subtypes represents a deeper level of diagnostic information, which commonly requires IHC/ICC; the chemical information obtained by DESI may circumvent or augment such protocols. The separation of B-cell and T-cell lymphoma is suggested in Figure 3-3; however, expansion of NHL subtypes is necessary to confirm this initial report. More detailed exploration of the chemical differences was performed by iterative study of the relationship between disease states rather than together as in Figure 3-5. For example, the chemical difference between B-cell and T-cell NHL tumors is more apparent upon removal of normal samples. The separation noted must be taken as preliminary, particularly for T-cell tumors, based on the relatively small sample size and known genetic diversity of lymphomas. The ability to subtype tumors using DESI-MS has been previously demonstrated, e.g. in brain and kidney tumors,(13, 15) but has not been previously reported in lymphoma. Diagnostic information acquired by DESI would serve to support pathological diagnosis, particularly relating to tumor subtyping as an alternative to immunohistochemistry.

The discriminatory performance of DESI-MS in determining disease state and subsequently tumor subtype from tissue sections was explored via PCA-LDA. Cross-validation was performed, Table 3-2, resulting a sensitivity and specificity of 93.1% and

100%, respectively. Further, PCA-LDA was performed separately taking the lymphoma subtypes into consideration, sensitivity and specificity per class (i.e. normal, B-cell, and T-cell) are tabulated in Table 3-3. Cross validation indicated two misclassifications (T-cell predicted as normal, and B-cell predicted as T-cell). The CV sensitivity of T-cell lymphoma (85.7%) was relatively poor in comparison to the other states (normal, 100% and B-cell lymphoma, 95.5%), likely the result of a smaller sample size (n=7) or the presence of two different T-cell subtypes (i.e. peripheral and T-zone).

3.3.3 DESI-MS Imaging of Fine Needle Aspirates

Histopathological evaluation of surgically excised lymph nodes, the gold standard for lymphoma diagnosis, is an invasive procedure and therefore not suitable for rapid preliminary diagnosis of NHL. Fine needle aspirate biopsy is a less expensive, less invasive, and less technically demanding method, and therefore a reasonable alternative. FNA smears are evaluated by cytology and tend to be less reliable than surgical biopsy, due to the destruction of morphological information through smearing. However, DESI-MS analysis of FNA smears provided molecular information that is similar to that of tissue sections and offers an alternative to FNA cytology, aimed at enhancing diagnostic capability.

FNA smears, prepared using standard protocols, were analyzed without any pre-treatment. DESI-MS imaging was performed on a small area of the smear, not the entirety of the smear, representing a time reducing strategy for preliminary diagnosis. An analogous similar time reduction strategy has been implemented for intrasurgical analysis of brain tumors using tissue smears, discussed later in this dissertation. It was assumed that aspiration and subsequent smearing, was sufficiently homogenizing. The MS data obtained from FNA smears were highly reminiscent of those for surgical biopsy tissue sections; the average mass spectra for normal and B-cell lymphoma are displayed in Figure 3-6. The chemical information obtained from FNA appears to be identical in nature to that of tissue sections suggesting that the type of sample does not impact ability to acquire chemical information correlated to disease state. The strategy of using DESI spectra obtained from tissue sections serves as an important reference in this case, having been used previously in other forms of cancer diagnosis, (11, 13, 15, 29) thus allowing evaluation of FNA as a new type of sample for the same DESI methodology.

Unsurprisingly, subtle differences do exist between tissue sections and FNA smears which did not preclude acquisition of mass spectral information but rather influenced data quality. FNA smears were nearly always chemically homogenous, i.e. the lipid profile was similar in all areas of the smear, supporting the assumption of sufficient homogenization, while difference in the signal intensity were common. Two major variables in FNA smears were found to affect MS intensity: the quantity of cellular material aspirated and the degree of dilution due to smearing. The effect of quantity is noted in the heterogeneity present in the ion images,

Figure 3-7, which resulted from variable amount of material – signal intensity is correlated with material quantity. The second variable is the degree of smearing of the aspirated sample which dilutes the cellular material on the glass slide. This dilution is necessary for cytologic evaluation using light microscopy, in which morphologic evaluation of isolated cells is desirable, but is deleterious for chemical analysis by DESI-MS. Slight modification to current FNA protocols that compensate for these effects is likely to increase DESI reproducibility, MS data quality, and capability for molecular diagnosis. Additionally, differences in the lipid profile were noted in cases of obvious blood contamination of the aspirated sample, resulting in a visually red coloration to the smear. The presence of blood contamination significantly increased one particular lipid, *m/z* 810, which corresponds to PS 40:6, a major membrane constituent of erythrocytes (30) and therefore easily detected. Minor blood contamination did not seem to compromise the ability to determine disease state.

Figure 3-8, subsequent staining of FNA smears (Wright's stain) analyzed by DESI and evaluation by light microscopy, indicated cellular damage, which could result from physical damage during smearing or freeze thaw cycle. Certainly, DESI has the potential to produce the observed cellular damage via physical (e.g. pneumatic) forces or chemical fixation (i.e. organic solvent). An expert cytopathologist commented that the morphologic changes in the cells appeared similar to those commonly observed in samples exposed to formalin, a common chemical fixative, which supports the latter reason for the observed effect. This observation is quite interesting in that it contrasts the preservation of morphology during analysis of histologic tissue sections – no effect on histomorphology is noted using dimethylformamide-acetonitrile as a DESI solvent system. One biological reason for this observation is the presence of stromal tissue and extracellular matrix in histologic sections, which may minimize the cellular damage of

DESI analysis relative to what was observed in FNA smears, which would presumably contain less of these protective elements.

3.3.4 Differentiation of Disease State using FNA Smears

The chemical information obtained using DESI-MS from FNA smears was evaluated by multivariate statistics. In clinical practice, the information relevant in FNA evaluation is the presence or absence of tumor, and serves only to provide a rapid, preliminary diagnosis which requires subsequent confirmation by more accurate methods such as histopathology. PCA-LDA was applied and performed by building a classification training set using tissue section data and evaluating the FNA smear data. PCA-LDA prediction of the FNA smears, Table 3-4, provided a sensitivity of 89.3% and specificity of 85.7%. The preliminary results displayed indicate that DESI-MS analysis of FNA smears has diagnostic potential. FNA smears, neither adapted nor optimized for MS analysis, provided reasonable classification results, provided that FNA smears are known to be less reliable than surgical biopsy samples evaluated by histopathology.

Beyond the rapid molecular diagnosis of NHL by DESI-MS via FNA analysis, the envisioned application, has the potential for rapid tumor subtyping. PCA cross-validation of tissue sections indicated the possibility for tumor subtyping; however, this could not be explored based on FNA sample numbers. Surely, this requires a larger and more diverse sample set, particularly with knowledge of NHL tumor heterogeneity. The primary goal of FNA analysis by DESI was demonstrated: rapid molecular-based dichotomous delineation of disease state (i.e. normal and tumor), which has potential to be a significant advancement in the rapid diagnosis of non-Hodgkin's lymphoma.

3.4 Conclusions

Differences in the lipid profiles differentiated normal lymph node and NHL tumors in tissue sections (obtained by surgical biopsy) analyzed by DESI-MS imaging. Normal lymph node tissue was chemically homogenous while differences in absolute signal were noted between regions of normal lymph node anatomy, e.g. medulla and cortex. Tumor samples were generally homogenous, particularly diffuse large B-cell lymphoma samples, matching known morphology. Multivariate statistics allowed for differentiation of normal and tumor tissue sections with a sensitivity and specificity of 93.1% and 100%, respectively. Further, subtyping of NHL tumors is suggested with an equal rate of predicted classification. FNA smears, previously unexplored for use in diagnosis using ambient ionization – mass spectrometry, provided the same chemical information relevant to disease state differentiation detected from tissue sections. FNA smear data applied to a tissue section-based classification system resulted in a sensitivity of 89.3% and specificity of 85.7%. MS signal was dependent on the composition (e.g. blood contamination), aspirated material quantity and smearing. The act of smearing of FNA, while ideal for cytology, dilutes the cellular material necessary for DESI-MS lipid analysis. Improvement in the protocols for FNA preparation, with tailoring specifically for MS analysis is likely to improve results. The molecular information detected from FNA smears are not subject to the same set of problems (e.g. physical damage of cells) experienced in cytopathology, and therefore could improve diagnostic yield. Cellular damage was noted after DESI analysis upon FNA samples, affecting only subsequent pathology and not the molecular information. The reason for this damage is presently unknown, but might result from chemical damage or pneumatic pressure. The informative but less invasive collection of FNA smears, also performed during diagnosis of other cancers, particularly those of the breast, thyroid, and salivary gland, is clearly best suited to answer the question of rapid preliminary diagnosis, “Is this sample normal or cancerous?”

DESI-MS analysis of tissue sections provided a means of exploring and establishing the lipid profiles indicative of normal lymph node and NHL tumors. FNA smears mimic those changes, primarily in GPL composition, which are certainly related to cellular and morphological changes that occur with NHL. The polar lipids detected in the negative ion mode represent only a fraction of metabolites, and further study of the metabolome may reveal additional diagnostic information. The subtype prevalence, clinical behavior, and chemical changes in GPL emulate that of human NHL, (27) supporting development of canine comparative models. The methodology outlined here is applicable to dogs while translation to humans is foreseeable.

3.5 Acknowledgements

I would like to thank our excellent collaborator Dr. Michael O. Childress for his assistance with study design, identifying subjects, and collecting specimens. The pathological evaluation provided by Dr. José A. Ramos-Vara and Dr. Craig A. Thompson is greatly appreciated. I would also like to acknowledge the Aston Lab team of Dr. Valentina Pirro and her help with data analysis, Dr. Kevin S. Kerian for his help with MS analysis, and Dr. R. Graham Cooks.

3.6 References

1. Ito D, Frantz AM, Modiano JF. Canine lymphoma as a comparative model for human non-Hodgkin lymphoma: recent progress and applications. Veterinary Immunology and Immunopathology. 2014;159(3):192-201.

2. National Cancer Institute - SEER Fact Sheet [cited 2016 July 19]. Available from: http://seer.cancer.gov/statfacts/.

3. Marconato L, Gelain ME, Comazzi S. The dog as a possible animal model for human non-Hodgkin lymphoma: a review. Hematological Oncology. 2013;31(1):1-9.

4. Valli VE, San Myint M, Barthel A, Bienzle D, Caswell J, Colbatzky F, et al. Classification of canine malignant lymphomas according to the World Health Organization criteria. Veterinary Pathology. 2011;48(1):198-211.

5. Ponce F, Marchal T, Magnol J, Turinelli V, Ledieu D, Bonnefont C, et al. A morphological study of 608 cases of canine malignant lymphoma in France with a focus on comparative similarities between canine and human lymphoma morphology. Veterinary Pathology. 2010;47(3):414-33.

6. Hehn ST, Grogan TM, Miller TP. Utility of fine-needle aspiration as a diagnostic technique in lymphoma. Journal of Clinical Oncology. 2004;22(15):3046-52.

7. Das DK. Value and limitations of fine-needle aspiration cytology in diagnosis and classification of lymphomas: A review. Diagnostic Cytopathology. 1999;21(4):240-9.

8. Landgren O, Porwit MacDonald A, Tani E, Czader M, Grimfors G, Skoog L, et al. A prospective comparison of fine-needle aspiration cytology and histopathology in the diagnosis and classification of lymphomas. The Hematology Journal. 2004;5(1):69-76.

9. Venter A, Sojka PE, Cooks RG. Droplet dynamics and ionization mechanisms in desorption electrospray ionization mass spectrometry. Analytical chemistry. 2006;78(24):8549-55.

10. Costa AB, Cooks RG. Simulated splashes: Elucidating the mechanism of desorption electrospray ionization mass spectrometry. Chemical Physics Letters. 2008;464(1):1-8.

11. Dill AL, Ifa DR, Manicke NE, Costa AB, Ramos-Vara JA, Knapp DW, et al. Lipid profiles of canine invasive transitional cell carcinoma of the urinary bladder and adjacent normal tissue by desorption electrospray ionization imaging mass spectrometry. Analytical Chemistry. 2009;81(21):8758-64.

12. Wiseman JM, Puolitaival SM, Takáts Z, Cooks RG, Caprioli RM. Mass spectrometric profiling of intact biological tissue by using desorption electrospray ionization. Angewandte Chemie. 2005;117(43):7256-9.

13. Eberlin LS, Norton I, Orringer D, Dunn IF, Liu X, Ide JL, et al. Ambient mass spectrometry for the intraoperative molecular diagnosis of human brain tumors. Proceedings of the National Academy of Sciences. 2013;110(5):1611-6.

14. Jarmusch AK, Pirro V, Baird Z, Hattab EM, Cohen-Gadol AA, Cooks RG. Lipid and metabolite profiles of human brain tumors by desorption electrospray ionization-MS. Proceedings of the National Academy of Sciences. 2016:201523306.

15. Dill AL, Eberlin LS, Zheng C, Costa AB, Ifa DR, Cheng L, et al. Multivariate statistical differentiation of renal cell carcinomas based on lipidomic analysis by ambient ionization imaging mass spectrometry. Analytical and Bioanalytical Chemistry. 2010;398(7-8):2969-78.

16. Dill AL, Eberlin LS, Costa AB, Zheng C, Ifa DR, Cheng L, et al. Multivariate statistical identification of human bladder carcinomas using ambient ionization imaging mass spectrometry. Chemistry-a European Journal. 2011;17(10):2897-902.

17. Eberlin LS, Tibshirani RJ, Zhang J, Longacre TA, Berry GJ, Bingham DB, et al. Molecular assessment of surgical-resection margins of gastric cancer by mass-spectrometric imaging. Proceedings of the National Academy of Sciences. 2014;111(7):2436-41.

18. Eberlin LS, Ferreira CR, Dill AL, Ifa DR, Cheng L, Cooks RG. Nondestructive, histologically compatible tissue imaging by desorption electrospray ionization mass spectrometry. ChemBioChem. 2011;12(14):2129-32.

19. Pirro V, Eberlin LS, Oliveri P, Cooks RG. Interactive hyperspectral approach for exploring and interpreting DESI-MS images of cancerous and normal tissue sections. Analyst. 2012;137(10):2374-80.

20. Bro R, Smilde AK. Principal component analysis. Analytical Methods. 2014;6(9):2812-31.

21. Ferreira CR, Pirro V, Eberlin LS, Hallett JE, Cooks RG. Developmental phases of individual mouse preimplantation embryos characterized by lipid signatures using desorption electrospray ionization mass spectrometry. Analytical and bioanalytical chemistry. 2012;404(10):2915-26.

22. Passarelli MK, Winograd N. Lipid imaging with time-of-flight secondary ion mass spectrometry (ToF-SIMS). Biochimica et Biophysica Acta (BBA)-Molecular and Cell Biology of Lipids. 2011;1811(11):976-90.

23. Caprioli RM. Imaging mass spectrometry: Molecular microscopy for the new age of biology and medicine. Proteomics. 2016.

24. Campbell DI, Ferreira CR, Eberlin LS, Cooks RG. Improved spatial resolution in the imaging of biological tissue using desorption electrospray ionization. Analytical and bioanalytical chemistry. 2012;404(2):389-98.

25. Laskin J, Heath BS, Roach PJ, Cazares L, Semmes OJ. Tissue imaging using nanospray desorption electrospray ionization mass spectrometry. Analytical Chemistry. 2011;84(1):141-8.

26. Jackson AU, Shum T, Sokol E, Dill A, Cooks RG. Enhanced detection of olefins using ambient ionization mass spectrometry: Ag+ adducts of biologically relevant alkenes. Analytical and bioanalytical chemistry. 2011;399(1):367-76.

27. Eberlin LS, Gabay M, Fan AC, Gouw AM, Tibshirani RJ, Felsher DW, et al. Alteration of the lipid profile in lymphomas induced by MYC overexpression. Proceedings of the National Academy of Sciences. 2014;111(29):10450-5.

28. Abbassi-Ghadi N, Veselkov K, Kumar S, Huang J, Jones E, Strittmatter N, et al. Discrimination of lymph node metastases using desorption electrospray ionisation-mass spectrometry imaging. Chemical Communications. 2014;50(28):3661-4.

29. Kerian KS, Jarmusch AK, Pirro V, Koch M, Masterson T, Cheng L, et al. Differentation of Prostate Cancer from Normal Tissue in Radical Prostatectomy Specimens by Desorption Electrospray Ionization and Touch Spray Ionization Mass Spectrometry. The Analyst. 2014.

30. Leidl K, Liebisch G, Richter D, Schmitz G. Mass spectrometric analysis of lipid species of human circulating blood cells. Biochimica et Biophysica Acta (BBA)-Molecular and Cell Biology of Lipids. 2008;1781(10):655-64.

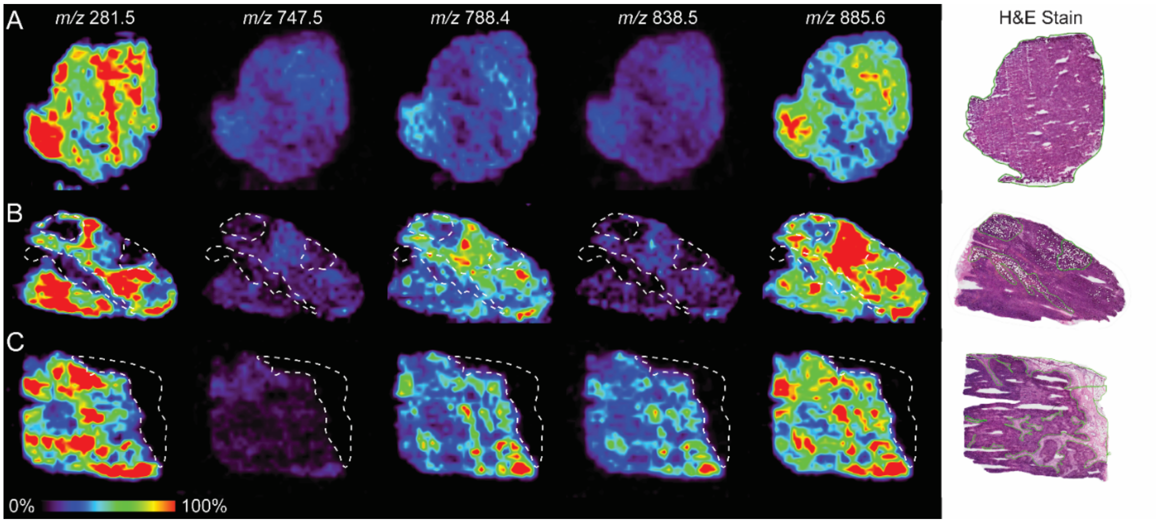

Figure 3-1 Selected negative mode DESI-MS ion images displaying the distribution of ions *m/z* 281.5, 747.5, 788.4, 838.5, and 885.6 and the corresponding H&E stain. (A) Specimen 18 is representative of B-cell lymphoma samples in regards to chemical and spatial homogeneity. (B) Specimen 31, B-cell lymphoma, contained small regions of perinodal adipose (outlined). (C) Specimen 42, illustrative of normal samples. The large region of perinodal adipose (outlined) was chemically difference than that of normal lymph node tissue.

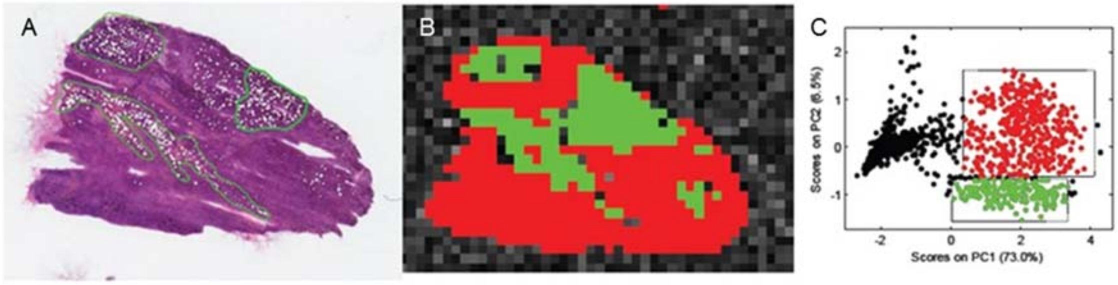

Figure 3-2 (A) Sample from specimen 31, H&E stain with annotated non-neoplastic regions in green. (B) DESI-MS image, colors indicating chemical similarity. (C) PCA score plot of pixels with subgrouping selected.

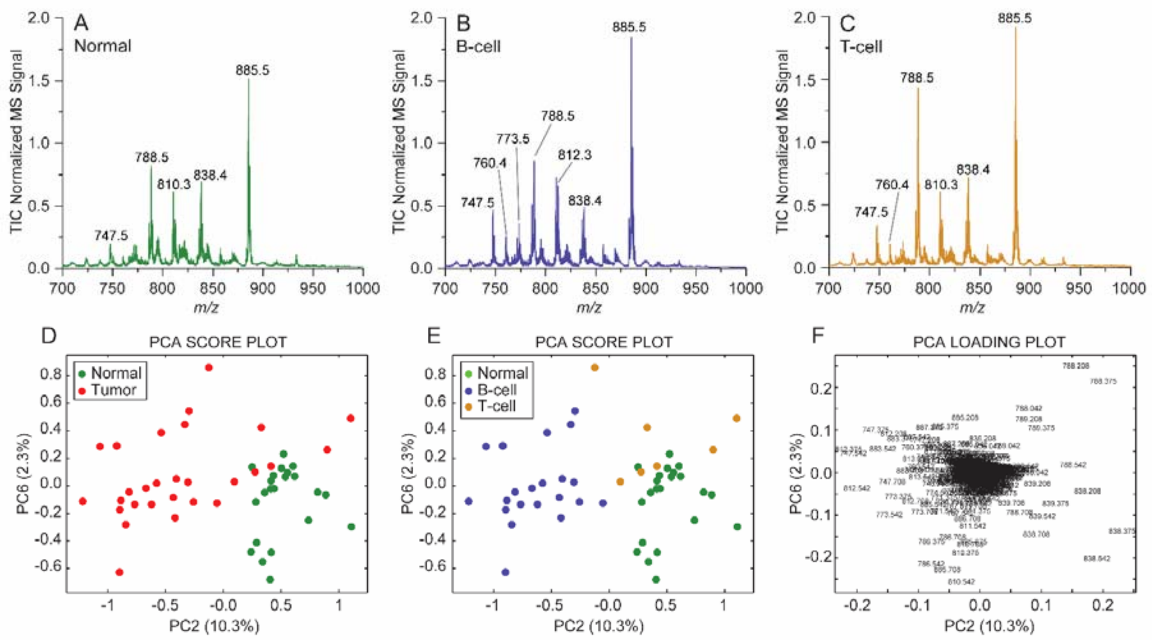

Figure 3-3 Average negative mode DESI mass spectrum, *m/z* 700 – 1000, of tissue sections: (A) normal lymph node (n=22), (B) B-cell lymphoma (n=22), and (C) T-cell lymphoma (n=7). (D) PCA score plot of normal (green) and tumor (red) samples. (E) PCA score plot of normal (green), B-cell lymphoma (blue), and T-cell lymphoma (gold) samples. (F) PCA loading plot corresponding to panel D&E with *m/z* annotated.

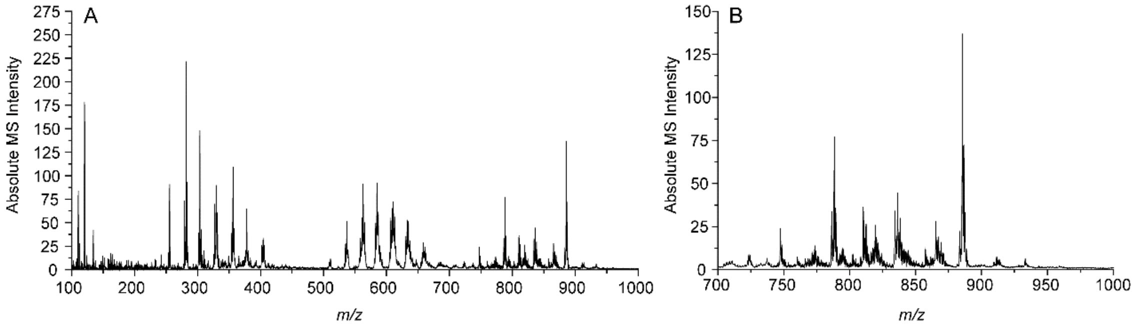

Figure 3-4 (A) Metastatic carcinoma to lymph node, specimen 12, negative mode DESI-MS. (B) Zoomed region *m/z* 700-1000 containing glycerophospholipids.

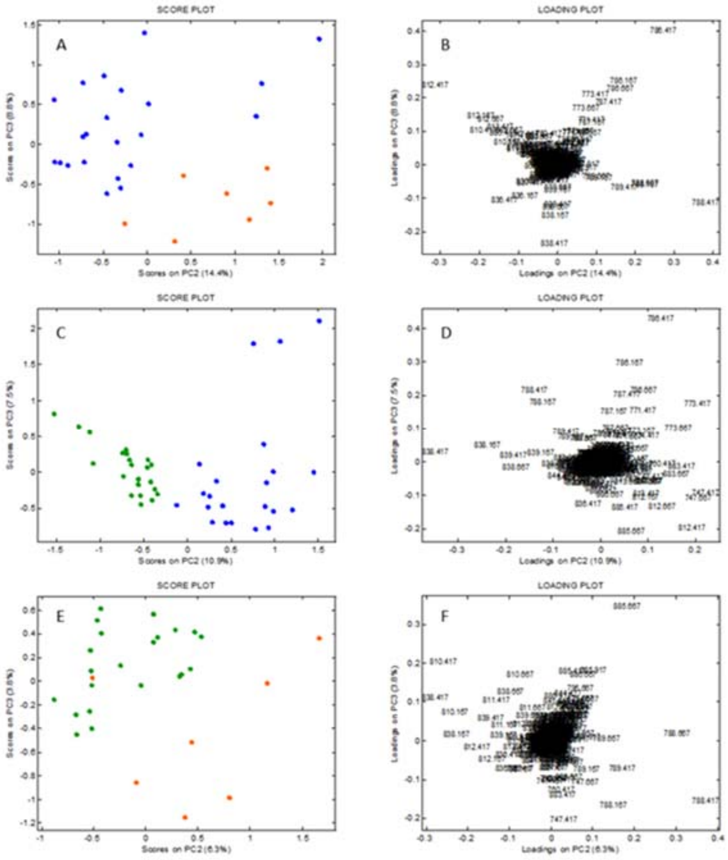

Figure 3-5 (A) PC2 vs. PC3 score plot for B-cell and T-cell lymphoma, color coded in orange and blue respectively, and (B) corresponding PCA loading plot, loadings are annotated as *m/z* values. (C) PC2 vs. PC3 score plot for normal (green) and B-cell (blue), and (D) PCA loading plot, loadings are annotated as *m/z* values. (E) PCA score plot for normal (green) and T-cell lymphoma (orange) and corresponding (F) PCA loading plot, loadings are annotated as *m/z* values.

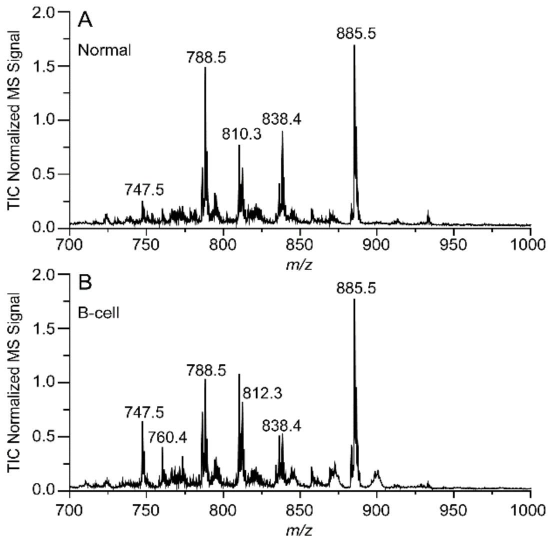

Figure 3-6 Average negative mode DESI-MS spectrum, *m/z* 700 – 1000, for (A) normal fine-needle aspirate smears (n=7) and (B) B-cell lymphoma fine-needle aspirate smears (n=28).

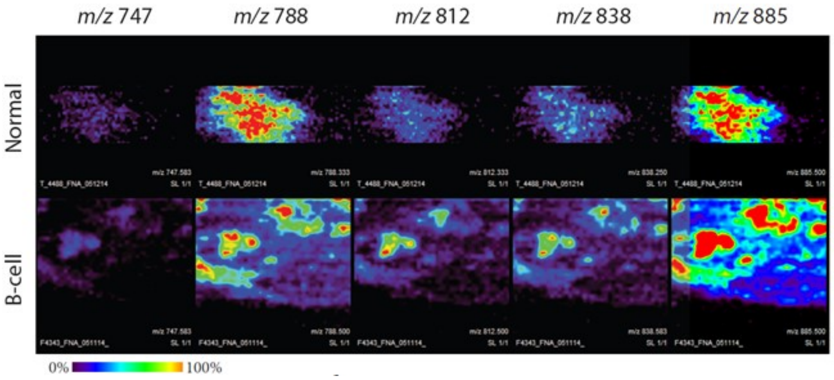

Figure 3-7 DESI ion images of normal (top) and B-cell lymphoma (bottom) fine-needle aspirate smears, the latter contains areas of higher intensity corresponding to amount of material present.

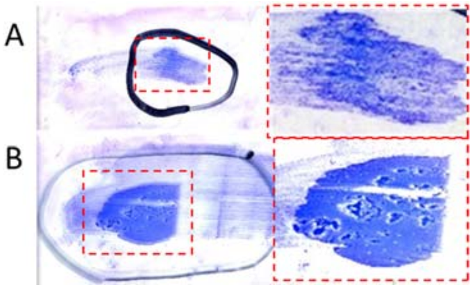

Figure 3-8 Wright's stained fine-needle aspirate smears displaying (A) an even distribution of material and (B) uneven distribution of material with corresponding zoomed insets.

Table 3-1 Tabulated negative ion mode DESI high resolution mass spectrometry data for predominate ions observed in the negative mode with identifications.

`			Normal		B-cell lymphoma		T-cell lymphoma	
Name	Ion formula	Theoretical mass	Measured mass	Mass error (ppm)	Measured mass	Mass error (ppm)	Measured mass	Mass error (ppm)
Palmitic acid	$[C_{16}H_{31}O_2-H]-$	255.2324	255.2324	0.0	255.2323	-0.4	255.2327	1.2
Oleic acid	$[C_{18}H_{32}O_2-H]-$	281.248	281.2481	0.4	281.248	0.0	281.2483	1.1
Stearic acid	$[C_{18}H_{35}O_2-H]-$	283.2637	283.2637	0.0	283.2636	-0.4	283.264	1.1
Arachidonic acid	$[C_{20}H_{31}O_2-H]-$	303.2324	303.2323	-0.3	303.2323	-0.3	303.2327	1.0
PG 34:1	$[C_{40}H_{76}O_{10}P-H]-$	747.5176	747.5173	-0.4	747.5171	-0.7	747.5184	1.1
PS 34:1	$[C_{40}H_{75}NO_{10}P-H]-$	760.5128	760.5128	0.0	760.5122	-0.8	760.5136	1.1
PE 38:4	$[C_{43}H_{77}NO_8P-H]-$	766.5386	766.5386	0.0	766.5383	-0.4	766.5393	0.9
PG 36:2	$[C_{42}H_{78}O_{10}P-H]-$	773.5332	773.5334	0.3	773.533	-0.3	773.5342	1.3
PS 36:1	$[C_{42}H_{79}NO_{10}P-H]-$	788.5441	788.5442	0.1	788.5439	-0.3	788.5450	1.1
PC 34:1 + Cl-	$[C_{42}H_{82}NO_8P+Cl]-$	794.5466	794.5465	-0.1	794.5464	-0.3	794.5471	0.6
PS 38:4	$[C_{44}H_{77}NO_{10}P-H]-$	810.5284	810.5285	0.1	810.5282	-0.2	810.5293	1.1
PS 40:4	$[C_{46}H_{81}NO_{10}P-H]-$	838.5598	838.5597	-0.1	838.56	0.2	838.5607	1.1
PI 38:4	$[C_{47}H_{82}O_{13}P-H]-$	885.5493	885.5491	-0.2	885.5488	-0.6	885.5500	0.8

Table 3-2 Cross-validation confusion matrix of DESI-MS in discriminating disease state (normal vs. canine non-Hodgkin's lymphoma) in tissue sections

		DESI-MS Prediction	
		Tumor[a]	Normal
Histopathology	Tumor[a]	27	2
	Normal	0	22

Table 3-3 Cross-validation confusion matrix for canine non-Hodgkin's lymphoma subtyping of tissue sections by DESI-MS

		DESI-MS Prediction		
		Normal	B-cell NHL	T-cell NHL
Pathology	Normal	22	0	0
	B-cell NHL	0	21	1
	T-cell NHL	1	0	6
	Sensitivity (%)	100.0	95.5	85.7
	Specificity (%)	96.4	100.0	97.7

Table 3-4 Principal component analysis – linear discriminant analysis prediction of fine-needle aspirate smears analyzed by DESI-MS

		DESI-MS Prediction	
		B-cell NHL	Normal
Histopathology	B-cell NHL	25	3
	Normal	1	6

CHAPTER 4. NEGATIVE ION MODE LIPID AND METABOLITE PROFILES OF HUMAN BRAIN TUMORS

4.1 Introduction

The incidence of brain tumors is approximately the same as that of non-Hodgkin’s lymphoma, melanoma, and urinary bladder cancer in adults over 20 years of age. Incidence rates in children and adolescents is even greater, more than five per 100,000. Brain tumors include a number of subtypes with the most prevalent being meningioma (~36%), glioma (~28%), and pituitary tumors (~15%); however, gliomas account for 80% of all malignant brain tumors.(1) In many cases, surgical resection is the most effective treatment option; maximal tumor excision is associated with an improved prognosis. (2) Gliomas are particularly difficult to treat via surgery as they often infiltrate the surrounding tissue and visually resemble normal brain tissue. Further, surgery must contend with the dilemma minimizing unintended neurological deficits while maximizing tumor removal. The gold standard for brain tumor diagnosis is histopathology. Histopathology relies heavily on morphologic and cytologic features revealed by staining of cellular structures (e.g. nucleus and cytoplasm). Surgical biopsies are taken during tumor excision and sent for histopathologic evaluation as frozen tissue sections and tissue smears. The pathologic information provided during surgery is limited, for example tumor type (e.g. glioma) and grade (e.g. low grade), compared to final pathologic evaluation which is performed using fixed tissue sections. Pathologic analysis can be repeated for infiltrative tumors to guide the extent of resection at the tumor margins; however, the time required for such evaluation (upwards of 20 minutes per sample) is limiting and prolongs surgery.

The potential diagnostic value of using ambient ionization and MS profiles, especially those based on lipids,(3) is increasing concurrently with the growing number of studies on lipid metabolism in cancer. (4, 5) Two schools of thought have emerged: offline approaches in which measurements are performed ex vivo and online approaches in which measurements are performed in vivo. (6) Desorption electrospray ionization – mass spectrometry (DESI) is arguably the most developed offline approach in which resected biopsies are analyzed ex vivo, but ideally within the operating room, providing results on the minute timescale. MS analysis by offline approaches can preserve tissue morphology allowing for subsequent histopathologic evaluation. Brain and other cancers have been investigated using rapid evaporative ionization – mass spectrometry, an online approach, a method which provides lipid–based differentiation between cancerous and normal tissue and has been performed in vivo upon patients undergoing surgical resection with promising results; however, electrocauterization is destructive and does not allow validation by pathology.(7)

DESI-MS detect biomolecules, e.g. lipids, in a profile, synonymous with mass spectrum (*m/z* values and associated abundances), and uses the entire profile for differentiation via multivariate statistics. This contrasts strongly with traditional biomarker measurement in which the predominant philosophy is “one molecule for one disease." Different methods of multivariate statistics, e.g. principal component analysis (PCA), have been used for analyzing ambient ionization MS data. The use of any one particular method must be tailored to match the question being asked. For example, PCA does not offer any ability to classify unknown samples, rather it is used for exploring the innate differences between samples in an unsupervised manner. Supervised discriminate (e.g. linear discriminant analysis, LDA) and class modeling (e.g. unequal class modeling, UNEQ) approaches allow for the classification of unknown samples. In the case of brain cancer, establishing a robust classification method is vital, and can only be implemented by including normal tissue. This is particularly difficult in the case of brain tumors in which absolute normal rarely exists for scientific study.

The study of brain cancer by DESI-MS has been an ongoing effort since 2010. (8) The negative ion mode lipid profiles acquired via DESI-MS imaging were found to be different between glioma subtypes, grades, and tumor cell concentrations (relative percent of tumor compared to parenchyma). (9) The lack of normal samples in that study prevented any conclusions as to differentiation between glioma and normal brain tissue. Surgically-derived samples with corresponding stererotactic information were analyzed, predicting tumor type (glioma or meningioma) and subtype, and illustrating the potential for determining tumor cell concentration (via lipid profiles) near the resection margins.(10) In a separate study, meningiomas, tumors which originate from the meninges (connective tissue surrounding the brain), have also been studied by DESI-MS. The lipid profiles of meniginiomas were found to be different between the normal dura mater and tumor. (11) There is little doubt that development of molecular techniques that rapidly discriminate cancerous tissue would be of great benefit to supplement intraoperative decision making and pathologic evaluation. Herein the development of a database of DESI-MS spectra, which includes negative ion mode lipid and metabolite profiles, from normal brain, grey and white matter, and gliomas is discussed. Additional differentiating information was found in the positive ion mode lipid profiles and is discussed in the next chapter. We also explored if negative ion mode lipid and metabolite profiles are capable of differentiating gliomas, meninigiomas, and pituitary tumors – types of tumors which represent ~80% of all brain and CNS tumors. DESI-MS analysis of tissue smears is detailed which greatly eases the implementation of DESI towards intrasurgical analysis.

4.2 Experimental

4.2.1 Materials

4.2.1.1 Banked Frozen Human Specimens

Cryopreserved human neurological specimens were obtained from 74 patients, 58 of whom were included in the sample cohort for the results discussed in Jarmusch et al. (12), by the Biorepository of Methodist Research Institute. The samples were purchased from the Biorepository of Methodist Research Institute after Purdue IRB determined that IRB review was not required (#1410015344). Tissue specimens were used to produce sections and smears. Details on the patient cohort are reported in the supplementary appendix of Jarmusch et al., (12) Table S4 - S5. The specimens were codified based on pathologic evaluation as grey matter (N=23 patients), white matter (N=14), gliomas (N=12) which consisted of 10 high-grade and 2 low-grade gliomas, meningiomas (N=13), pituitary tumor (N=14), and brain parenchyma containing reactive astrocytes (N=2). Subsequent to tissue sectioning and analysis, histopathologic evaluation determined that a number of samples contained multiple regions with different pathologies, hence the total number of patients for all classes does not equal the total number in the patient cohort. Tissue sections were made using a cryotome (Cryotome FSE, Thermo Scientific), 15 µm thickness, and thaw mounted onto glass microscope slides (Superfrost Plus, 25 x 75 x 1 mm, Electron Microscopy Sciences). Subsequently, tissue smears were prepared for each specimen by removing a small piece of frozen tissue (~10-50 mm^3), placing the tissue onto a glass microscope slide, allowing for the tissue to come to room temperature (20-25°C), and then smeared using a custom 3D printed device. (12) Tissue sections and smears were stored at -80°C prior to analysis. Materials were properly disinfected or autoclaved prior to disposal.

4.2.2 Methods

4.2.2.1 Negative Ion Mode Lipid and Metabolite Profiles via DESI-MS Imaging

The analysis of tissue sections and smears was performed on a linear ion trap mass spectrometer, model Finnigan LTQ (Thermo Electron Corporation, USA). The modifications to the instrument were the installation of a custom DESI source, which includes a source override adapter, an external cable for the application of high voltage, and an extended ion transfer capillary. The extended ion transfer capillary measuring a total length of 180 mm was constructed from stainless steel tubing (0.02” inner diameter and 1/16” outer diameter), the length protruding from the MS vacuum system was ~87.5 mm. Connection of the capillary with the threaded MS inlet was accomplished using Swagelok stainless steel fittings machined so that the capillary can be place all the way through the fitting and secured on one side with a ferrule and metal nut.

DESI-MS was performed using dimethylformamide-acetonitrile (1:1 v/v) which preserves tissue morphology for subsequent pathology.(13) Dimethylformamide and acetonitrile were purchased from Mallinckrodt Chemicals and Sigma-Aldrich, respectively. Additional source parameters are as follows: solvent flow rate, 1.0 µL min-1; pressure of nitrogen gas, 160 PSI; applied high voltage, -5 kV; incident angle, 52°; spray-to-surface distance, 2 - 3 mm; spray-to-inlet distance, 5 - 7 mm. Sections and smears were subjected to two sequential negative ion mode DESI-MS image acquisitions.

The first image acquired data from *m/z* 200 - 1000 with the mass spectrometer tuned for maximum transmission of *m/z* 786. The moving stage was then reset to the origin position, allowing for a subsequent image acquired from *m/z* 80 - 200 (MS tuned for *m/z* 174). Further detail of the different tune methods and corresponding instrument conditions and settings are reported in Jarmusch et al. (12)

DESI-MS imaging was performed upon tissue sections and smears by affixing the material to glass microscope slides and fixing these onto a custom two-dimensional precision moving stage. Images are collected as rows by coordinating linear motion of the moving stage with MS acquisition rate, defining resolution of 250 µm in “x”, upon completion of a row the moving stage resets to the original “x” position while stepping 250 µm in “y”. Upon completion of a sufficient number of “y” steps to cover the entire tissue surface, the moving stage was reset to the origin and a second image was acquired. The first image recorded data from *m/z* 200 - 1000 with an MS scan time of 0.85 s (automatic gain control, AGC, was disabled), 350 ms injection time with 2 microscans. The corresponding speed of the moving stage was 294.117 µm s^{-1}. The second image acquired data from *m/z* 80 - 200 with an MS scan time of 0.62 s, 125 ms ion injection time with 4 microscans - a faster injection time was necessary to compensate for greater MS abundance and lack of AGC. The linear motion of the moving stage was increased to 403.225 µm s^{-1}, compensating for the change in MS scan time, maintaining an average of one MS scan per 250 microns in the “x” dimension.

4.2.2.2 Pathology

Tissue sections and tissue smears analyzed by DESI-MS were stained after analysis by hematoxylin and eosin. Slides were chemically fixed in methanol (100%) for 2 minutes and rinsed in nanopure water (10 dips). Then slides were stained in modified Harris hematoxylin solution (Sigma-Aldrich) for 1.5 minutes, rinsed in nanopure water (10 dips), quickly dipped into Bluing Reagent (Protocol), and dipped 10 times in nanopure water. Slides were then placed in Intensified Eosin Y (Protocol) for 8 seconds and rinsed in ethanol (180 proof) in two sequential steps (10 dips each). The slides were dipped a total of 12 times into xylenes. The slides were allowed to air dry and were subsequently mounted using mounting media (Organo/Limonene Mount, Sigma-Aldrich) and glass coverslips (12-545-C, Fisher Scientific). Blind histopathologic evaluation by expert pathologist, Dr. Eyas M. Hattab, of tissue sections and smears provided the diagnosis (e.g. glioma), grading information (if possible), and an estimated tumor cell percentage. Some of the stained tissue sections and smears were digitally scanned for creation of publication quality figures using the Aperio whole slide digital imaging system (Leica Biosystems, CA). The system imaged all slides at 20x. Additional pathologic information such as IDH mutation status and final pathologic diagnosis were assessed independently via standard of care protocols and provided to the researchers.

4.2.2.3 Data Handling

DESI-MS spectra were acquired using XCalibur 2.0 (.raw) and converted into .csv or .mzXML files, and then imported into MATLAB (MathWorks, Inc., Natick, MA, USA) to reconstruct the corresponding hyperspectral datacubes, which are composites of a spatial domain (“x” and “y”), and a spectral domain, comprising the *m/z* value and the corresponding *m/z* intensity. (14) Regions of interest (ROI) were selected in MATLAB based on histopathologic review by Dr. Hattab, each ROI selection is the average spectrum of 1 mm (4 pixels) x 1 mm (4 pixels). The number of such selections per tissue section varied between two and more than a dozen, according to the dimension and pathologically distinct regions in the tissue. In-house MATLAB routines were used to process all MS data and generate the corresponding plots, except the averaged mass spectra that were exported from MATLAB and plotted in Origin Pro for improved graphical quality. Figures were created and exported using Adobe Illustrator or Microsoft Powerpoint.

4.2.2.4 Univariate Statistics

The Kruskal-Wallis non-parametric hypothesis test was chosen to verify the occurrence of statistically significant differences of NAA between classes of tissue. NAA signal was normalized to the total ion current prior to Kruskal-Wallis. The null hypothesis H0 affirms that there are no significant differences between the independent populations under examination. A significant level (a two-tailed P-value) of 0.05

(confidence interval = 95%) was chosen for the statistical test. When the experimental P-value is lower than the critical P-value, the null hypothesis is rejected. As a post hoc test, the Mann-Whitney U test was performed. The statistical tests were performed in OriginPro 2015 using built-in statistics package upon data exported from MATLAB. OriginPro 2015 was used to generate the box and whisker plots. The median line is shown, the box corresponds to the interquartile range, whiskers represent ±1.5 standard deviation, and outliers are annotated.

Receiver operator curve (ROC) analysis was performed to estimate sensitivity and specificity of NAA, determining the cut-off value (i.e. TIC normalized ion abundance, percentage) of 1.5% - corresponds to the value displayed in the y-axis of the box and whisker plot for NAA. Further, the overall accuracy (area under the curve) in discrimination of brain parenchyma and glioma was calculated.

4.2.2.5 Multivariate Statistics

Principal component analysis (PCA) was used to explore the DESI-MS data in an unsupervised fashion and to visualize groupings of samples based on chemical similarity. All spectra were normalized using standard normal variate (SNV) transform, correcting for baseline shift and variation in absolute intensity, and mean-centered prior to PCA. No background signal correction, smoothing filters, or data binning were applied. PCA was also performed with a mid-level data fusion approach, in order to comprehensively visualize relationships among samples and variables coming from multi-block experiments (lipid and metabolite profiles). The first round of PCA acts as an unsupervised latent-variable compression technique, informative features were extracted from the raw signals of each block (i.e. profile) by PCA, individually, and then combined into a new (reduced) fused dataset. The fused dataset is then analyzed by PCA providing the multivariate statistical results of data fusion.

Linear discriminant analysis (LDA) was performed as a supervised discriminant classification technique after unsupervised data compression using PCA. Discriminant methods look for a delimiter that divides the global multidimensional data domain into a number of regions, each assigned to one of the sample classes. This delimiter identifies an open region for each class and such regions determine the assignment of the samples to one of the classes. Model validation (i.e. evaluation of the predictive ability of the model) was performed via cross validation (CV) using 5 deletion groups. The number of principal components used was selected so that ~90% of the cumulative variance in the data was included. The CV confusion matrix shows how many samples belonging to a certain category were correctly/incorrectly assigned by the classification rule to that category. Sensitivity and specificity are conventionally defined and were calculated by conventional methods per class.

Canonical correlation analysis (CCA) is a way of measuring the linear relationship between two blocks of multidimensional variables observed on the same specimens.(15) We used CCA to compare the DESI-MS spectra from tissue sections and smears. CCA rotates the original variables in the two blocks, to obtain pairs of variables (one for each block), called canonical variables, that maximize correlation between the two blocks.

The canonical variables are linear combinations of the original autoscaled (i.e. unitary variance) variables. The correlation coefficients between the canonical variables of the two blocks of measurements are termed canonical correlation coefficients. In order to overcome the high inter-correlations across *m/z* values, CCA was performed after PCA, which acts as an unsupervised data compression technique. CCA was performed using the open access chemometric package V-PARVUS 2010. (12)

4.3 Results and Discussion

4.3.1 Differentiation of Gliomas and Normal Brain Parenchyma using Negative Ion Mode DESI-MS Lipid Profiles

The negative ion mode lipid profiles of brain parenchyma (i.e. grey and white matter) and gliomas acquired by DESI-MS were explored and evaluated for their ability in differentiating disease state (i.e. normal versus tumor). DESI-MS imaging allowed the selection of regions of interest (ROI) based on histopathologic evaluation of the same tissue section. The average ROI mass spectra of grey matter, white matter, and glioma were substantially different. Grey matter is comprised of glia and mostly unmyelinated neurons and is associated with a very abundant negative ion mode peak at *m/z* 834, Figure 1, identified by high resolution mass spectrometry (HRMS) and MS/MS fragmentation as phosphatidylserine with 40 carbons with 6 units of unsaturation (40:6), predominant acyl chains are 18:0 (stearic acid) and 22:6 (docosahexaenoic acid) as indicated by MS/MS. Figure 4-1, white matter is characterized by an increased relative abundance of *m/z* 788 (PS 18:1_18:0), 888 ((3’-sulfo)GalCer 24:1), 906, and 916 in the negative ion mode. Sulfatides, e.g. *m/z* 888, 904 ((3’-sulfo)GalCer 24:1 (OH)), 906, and 916, are particularly abundant which correlates with the increased myelination of neurons. Tentative identifications herein are based on nominal mass but are supported by high resolution MS measurements tabulated in Table 4-1 and Table 4-2. The pattern of ions that corresponded to grey and white matter was consistent with previous studies of murine brain tissue.(16) The variations seen in the ratio of the signals associated with *m/z* 834 and 888 does not compromise the differences in relative abundance between grey and white matter (Figure 4-2). The average mass spectrum for gliomas, Figure 4-1, was very different from that of normal brain parenchyma in that it lacks the ions at *m/z* 834 and 888 characteristic of grey and white matter, respectively. Rather, an increase in the abundance of *m/z* 794 (chloride adduct of PC 34:1) and *m/z* 885 (PI 18:0_20:4) was noted.

DESI-MS imaging revealed that regions of different composition could be defined spatially; however, areas of mixed composition were also noted. The different regions associated with grey and white matter were easily detected using ion images, illustrated in Figure 4-3. The finger-like projections of white matter (*m/z* 888) extend from the major area on the right side of the tissue into an area of grey matter (*m/z* 834). Differences in the lipid profiles were noted between anatomical regions of the brain, such as the molecular layer (an anatomical substructure within the cortex) and the other cortical layers. Note the decrease in *m/z* 788 around the white matter projections in Figure 4-3 which corresponds to the molecular layer of the cortex. Figure 4-4, the ratio of *m/z* 788, 834, and 885 varied between the molecular layer, which surrounds a meningeal blood vessel (apparent in the ion image of *m/z* 788), and that of the cortex itself. Furthermore, multivariate analysis via interactive brushing (14) supports the observed difference between the molecular layer of the cortex (red), the cortex (green), and a region associated with the presence of some white matter (blue).

Principal component analysis (PCA) was performed on the lipid profiles selected from pathology-defined ROI of brain parenchyma and glioma tissue sections, Figure 4-5. Grey and white matter were well separated, based primarily on *m/z* 834 and 888, respectively. The dispersed location of a few grey and white matter points, those that fall between their respective groupings, corresponded to tissue of mixed composition as reflected in the mass spectra. This observation reflects known parenchyma composition which can contain mixtures of unmyelinated and myelinated neurons as well as glial cells. Brain parenchyma, grey matter (green) and white matter (blue), and glioma (red) were well separated in PCA space, indicating that the first level of pathologic evaluation, “is this a glioma or brain parenchyma?” can be answered; however, the dispersion of the glioma grouping represents a complex mixture between normal tissue and tumor as well as mixed compositions of grey and white matter. Dispersion of glioma points along the vector of grey and white matter separation (right-left) is related to the relative contribution of the background parenchyma to the detected lipid profile. It is possible that the lipid profile differences between grey and white matter can overshadow more subtle differences that might indicate the presence of invasive tumor cells, particularly at relatively low tumor cell percentages (TCP), i.e. relative amount of cancerous cells as compared to normal cells. This observation does not preclude the differentiation of normal tissue, infiltration, and gliomas, but rather confirms the known complexity of brain tumors. The dispersion of the glioma class in the vertical direction in PCA score space reflects the extent of infiltration of tumor cells or TCP. A likely contribution to the observed dispersion of the glioma group is the presence of glioma subtypes (e.g. astrocytoma and oligodendroglioma). For example, the lipid profile of an oligodendroglioma might appear more similar to white matter, which is composed of a greater number of oligodendrocytes than grey matter. Discrimination of glioma subtypes had been previously studied(9) but the lack of normal samples in that study limited discussion on which factor is more significant. Note, subsequent histopathologic evaluation revealed that normal specimens commonly contained various levels of secondary infiltration.

The grey and white matter classes were comprised of regions containing <25% tumor cell concentration (mode was 10%) and one sample contained 40% tumor cell, as determined by histopathology performed on the same sample analyzed, representing a tissue composition that is reasonably expected near the surgical margin. Surgical resection margin, the point at which tumor removal is stopped, is frequently not equivalent to the tumor margin, the point at which no detectable tumor cells are present. A few specimens were well separated from the glioma class in PCA space and were found to be completely normal or contain no observable tumor cells (<5%) by the pathologist. Glioma points which fell between the glioma group and either the grey or white matter group illustrate the disease spectrum and the complexity in determining the disease state in the face of contributions from background parenchyma and infiltration.

Linear discriminant analysis (LDA) was performed subsequent to PCA to estimate disease classification performance of the negative ion mode lipid profile. The cross validation results for grey matter, white matter, and gliomas were tabulated, Table 4-3, and sensitivity (i.e. the proportion of ROIs pertaining to that class that are correctly identified as such) and specificity (i.e. the proportion of ROIs not pertaining to that class that are correctly identified as such) were calculated per class (i.e. grey matter, white matter, or gliomas). The mean of all classes provided an overall sensitivity and specificity of 93.9% and 96.1%, respectively. Misidentified samples were generally those of mixed composition, evident from their lipid profile and their location on the PCA score plot. This result supports that the lipid profiles are characteristic of grey matter, white matter, and gliomas; however, the rate of change observed in the lipid profile is not dynamic enough to accurately reflect subtle differences in mixtures of grey and white matter or between normal matter and glioma.

4.3.2 Differentiation of Gliomas and Normal Brain Parenchyma using Negative Ion Mode DESI-MS Metabolite Profiles including N-acetyl-aspartic acid

The negative ion mode metabolite profile (*m/z* 80-200) acquired by DESI from human brain tissue has not been previously explored or shown to be important for differentiating disease state. The negative ion mode metabolite profile was acquired on the same tissue after recording the negative ion mode lipid profile. The average ROI mass spectra of grey matter (green), white matter (blue), and glioma (red) are displayed in Figure 4-6, respectively. Lactic acid, identified by HRMS, was detected as a deprotonated species at *m/z* 89 and was found to be slightly increased in abundance between gliomas (4.39 ± 1.93, TIC normalized mean ± standard deviation) , n=158, and brain parenchyma (3.74 ± 1.34), n=289. This observation is consistent with metabolic aberrations inherent in cancer (e.g. high rates of aerobic glycolysis), as postulated by Warburg and others, but it does not appear to be uniquely predictive of disease. By contrast, a dramatic decrease in *m/z* 174 was noted between grey and white matter and gliomas. The TIC normalized mean of normal brain parenchyma (grey and white matter, n = 298) was 3.72 ± 2.10 (standard deviation); whereas, the mean for gliomas, n = 158, was 0.36 ± 0.25. Figure 4-7, a box and whisker plot supported that *m/z* 174 alone provided discrimination of brain parenchyma from glioma (Kruskal-Wallis p-value <0.001). HRMS and MS/MS data obtained by collision induced dissociation were used to identify *m/z* 174 as N-acetyl-aspartic acid (NAA), detected as the deprotonated ion. Furthermore, a receiver operating characteristic (ROC) curve of brain parenchyma and glioma resulted in an area under the curve (AUC) of 0.998 (Figure 4-8). The abundance of *m/z* 174 was least in meningiomas, Figure 4-7; the absence of NAA is supported by previous NMR and LC-MS studies (33) – thus serving as an endogenous positive control (i.e. signal neither expected nor detected). Meningeal tissue, and presumably meningiomas, lacks the N-acetyltransferase necessary for the biosynthesis of NAA. DESI-MS ion images of specimen 20, Figure 4-9, illustrated the considerable difference between grey matter, which contained *m/z* 834 and *m/z* 174 (NAA), and an invasive boundary of a meningioma on the right-side of the tissue section.

PCA was performed on the metabolite profile, Figure 4-10, and yielded poor separation of grey and white matter from each other but clear separation between grey and white matter from glioma. The overwhelming significance of NAA in the multivariate separation is notable in the positive loading values on PC2. Interestingly, this finding supports previous MRSI studies which indicated NAA's significance in discriminating normal and diseased neural tissues(17, 18); however, MRSI is not a common procedure used for tumor diagnosis. (19, 20) Detection of NAA in situ by MS has greater molecular specificity and speed compared to the current means of detection, primarily MRI and related techniques. NAA is an abundant molecule in the human nervous system, the biological function of which is still to be unraveled but evidence indicates a significant role in neural metabolism.(21) Ties to central metabolic processes can be made via aspartic acid as well as acetate, including lipid metabolism, energy production, amino acid synthesis, and gene regulation.(21) Further, NAA has been found to decrease in many neurological diseases and disorders such as stroke, Alzheimer's disease, epilepsy, and multiple sclerosis.(21) The detection of NAA via MS appears to be an important measure of overall neural health as specimens containing reactive astrocytes (found in trauma, infection, ischemia, neurodegenerative disease, etc) was associated with a reduction in the relative abundance of NAA. The metabolite profile and PCA does not appear to differentiate grey matter from white, but the metabolite profile did separate gliomas well. PCA-LDA cross-validation of all classes (grey matter, white matter, and glioma), Table 4-4, resulted in an overall sensitivity of 71.6% and specificity of 86.4%; however, the sensitivity and specificity for gliomas was >90%.

We hypothesized that if the abundance of NAA and the presence of tumor are correlated than the reduction in signal would provide a means of determining tumor cell percentage (TCP), i.e. relative measure of tumor cells to normal cells, previously dubbed tumor cell concentration. ROIs selected from grey matter, white matter, and glioma were given an estimated TCP by our collaborating pathologist, plotted on the x-axis, and the normalized NAA abundance was plotted on the y-axis (Figure 4-11). The trend appeared to be exponential-like decay in NAA abundance with increased TCP. Following the observed exponential-like decay, the data were replotted on a semi-logarithmic plot and linear regression was performed (Pearson's r = -0.89). Further study of the observed correlation and improved measurement is required.

4.3.3 Differentiation Meningioma, Glioma, and Pituitary Tumors using Negative Ion Mode Lipid and Metabolite DESI-MS Profiles

Meningiomas and pituitary tumors represent a large fraction of all brain tumors; the lipid profile of the former was explored in a previous study [11]. We sought to differentiate the following tumor types: glioma, meningioma, and pituitary tumor. The average lipid mass spectra displayed differences in the relative abundances of *m/z* 788 (PS 36:1), 794 (chloride adduct of PC 34:1), and 885 (PI 38:4) between the tumor types, Figure 4-12. PCA performed upon glioma (N=158), meningioma (N=111), and pituitary tumors (N=154) using the lipid information, provided good separation between all tumor types. PCA-LDA cross validation provided an overall sensitivity (99.4%) and specificity (99.7%), Table 4-5. Whilst remarkable, this result is not surprising as the cells and tissue from which the various tumors arise are quite different (e.g. glia versus meninges), and this is reflected also in histopathologic evaluation. Note, the lack of normal specimens from different tissue type precluded conclusion regarding the ability to distinguish meningiomas and pituitary tumors from their respective normal tissues.

The metabolite profile, previously discussed as being differentiating between grey and white matter and glioma, was observed to have small differences in the average mass spectra between tumor types. Figure 4-7, NAA signals were significantly different between tumor types ($p<0.001$), although change was much smaller (compared to that observed between normal brain parenchyma and glioma) and therefore limits NAA's predictive value for discriminating between tumor types. Differential levels of NAA in gliomas, meningiomas, and pituitary tumors were reported by MRSI and our data supports these previous findings.(18) The mid-level fusion of lipid and metabolite profile information did not substantially change the predicted classification from using the lipids alone supporting the visual similarity of the metabolite profile. Comprehensively, gliomas, meningiomas, and pituitary tumors can be distinguished with little ambiguity, suggesting that an unknown sample from one of these three types of tumor could be chemically recognized by the DESI-MS lipid and metabolite profiles.

4.3.4 Improved Differentiation of Gliomas and Brain Parenchyma via Data Fusion

The best separation of grey and white matter and glioma was obtained when the lipid and metabolite profiles were considered together using mid-level data fusion, Figure 4-13. Grey matter (N=223), white matter (N=66), and gliomas (N=158), were well separated and had little intra-class dispersion. The ions that were important for differentiating grey matter, white matter, and glioma in the lipid and metabolite profiles were the same. However, it is clear that improved separation between brain parenchyma and glioma is achieved when the lipid profile information is use in conjunction with the metabolites, primarily NAA. Similarly, the lack of separation between grey and white matter in the metabolite profile is compensated for by the lipid profile information. PCA followed by LDA was performed to estimate classification performance when fusing the two MS profiles. The cross-validation of grey matter, white matter, and gliomas resulted in an overall sensitivity of 97.4% and specificity of 98.5%, Table 4-6. The major advantage of using the lipid and metabolite profile is that the combination appears to more accurately reflect mixed compositions of grey matter, white matter, and glioma. The two modes appear to compensate for each other allowing subtler changes to be detected that would otherwise not be reflected in either the lipid or the metabolite profile, independently.

We further evaluated the fused lipid and metabolite DESI-MS profiles by predicting the disease state and estimating the TCP of a pathologically ambiguous specimen, Figure 4-14, as an external validation. A false-color plot of the PC1 scores of individual pixels revealed a region associated with glioma (red pixels) and a region more closely associated with white matter (blue). Pathologic evaluation of these two regions was ambiguous with one clearly a glioma and the other being either a diffuse glioma or an infiltrated region adjacent to the tumor region, qualitatively matching our findings of two chemically different regions. Further evaluation was performed using PCA-LDA as shown in which classified a region of glioma (right) while classifying the adjacent region as white matter. The region classified by LDA as white matter prompted further examination for infiltration (because infiltration was not a part of the PCA-LDA model) via NAA abundance based estimation of the tumor cell percentage. The estimated TCP in the glioma region was >75% while the other region had estimated TCP ranging from approximately 50 to 30%, roughly matching with pathologic evaluation of 60%. This illustrative example supports that MS profiles, processed using multivariate statistics, can correctly discriminate gliomas and that they can also be used to detect diffuse and infiltrative tumors, a particularly critical question during surgical resection.

4.3.5 DESI-MS Analysis of Neural Tissue Smears

Intraoperative analysis by DESI-MS is limited by the need for freezing and generating tissue sections prior to analysis. DESI-MS analysis of tissue smears is an attractive alternative to the use of tissue sections. To date, DESI-MS analysis of tissue and cytological smears has been only briefly explored.(12, 22) Smears are commonly performed by placing a minute amount of tissue onto a glass slide and then physically spreading the material to achieve a relatively uniform and diffuse layer of cellular material for staining and subsequent pathology. A custom tissue smear device was designed to confine the tissue to the middle of the glass slide (along the narrowest dimension) and smear the tissue along the longest dimension with an approximate thickness of 100 µm (Figure 4-15).

Tissue smears were imaged over an area of ~75 mm^2, exploring the MS quality and the homogeneity of the chemical information. The absolute MS signal was generally equal to that of tissue sections. Importantly, the relative abundances of the ions were similar between tissue sections and tissue smears. The average metabolite and lipid profiles of grey matter and gliomas, Figure 4-16, mirror those of the tissue sections. For example, the abundance of *m/z* 834 is notable in the grey matter spectrum and dramatically reduced in the gliomas. Similarly, the statistical significance of NAA (*m/z* 174), $p<0.001$, allows for the discrimination of grey matter and gliomas (Figure 4-17). Canonical correlation analysis (CCA)(15) was performed to assess the similarity of the chemical information obtained from tissue smears and sections, Figure 4-18. The correlation coefficients are notable (greater than 0.95) between the first three canonical variables for both the lipid and metabolite profiles, emphasizing that the physical change induced by smearing does not influence the chemical information. As a precaution, it should be mentioned that the sample matrix and associated analytical effect could influence the data obtained by MS but this effect was not observed in our experiments. The lipid and metabolite profiles of smears were nearly identical to those recorded from tissue sections indicating that sectioning can be foregone for more rapid tissue smear analysis.

4.4 Conclusions

The application of DESI-MS in brain cancer resection requires knowledge of the characteristic chemical features that distinguish brain parenchyma from glioma and different tumor types from each other and this was explored here for the first time. The strategy of using MS profiles to characterize tissue differs from the traditional use of biomarkers in which a single molecule (or ion detected by MS) is used as an indicator of disease. MS profiles are an integrated representation of downstream metabolism, or chemotype, and provide important information which extends beyond tissue diagnosis (e.g. in the case of 2HG it extends to prognosis).

We demonstrated that MS analysis of tissue sections revealed lipid-derived and metabolite signals that differ between grey and white matter and gliomas, facilitating discrimination by multivariate statistics. Difference in the MS profiles revealed the effect of brain parenchyma upon the signal obtained from glioma samples. This observation is particularly significant as gliomas frequently invade along white matter tracts, illustrating the need to understand the contribution of brain parenchyma and infiltration in predicting disease state. The significance of NAA in discriminating brain parenchyma and glioma is clear and immense. This study offers strong evidence that NAA is in fact an oncometabolite and the first in situ detection of NAA by ambient MS. The importance of NAA in glioma differentiation confirms nearly 20 year old MRSI data. NAA also appears to be predictive of tumor cell concentration in unknown samples with an exponential-like decay in MS signal from brain parenchyma to glioma. Fusion of the lipid and metabolite MS profiles provided the best discrimination of brain parenchyma (grey and white matter) and gliomas with an overall sensitivity of 97.4% and specificity of 98.5%. Further, the MS profiles proved capable of discriminating tumor types (i.e. glioma, meningiomas, and pituitary tumors) with a sensitivity and specificity >99%.

Surgical intervention of brain tumors could be simplified with intraoperative analysis of tissue without extending operative times. Tissue smears were explored which eliminate the need for tissue freezing and sectioning prior to DESI-MS. The use of a custom 3D printed smear device aided in the distribution of tissue during smearing while maintaining a sufficiently thin smear for DESI-MS. The observed lipid or metabolite profiles were not significantly altered by the physical act of smearing and their signal intensities were comparable to those of tissue sections. Further, the chemical information obtained from tissue smears was equivalent to those of tissue sections as determined by CCA. The validation of tissue smears as samples for discriminate analysis remains to be fully vetted; however, this work lays the foundation for implementation of DESI-MS intraoperatively.

4.5 Acknowledgements

I would like to acknowledge my mentor, Dr. R. Graham Cooks, and the Aston Lab team for their contribution to this project. Dr. Valentina Pirro was pivotal in the bioinformatics and study design. Dr. Zane Baird's contributed to the 3D printed smear device design and manufacturing. I would also like to acknowledge the contributions of our collaborator physicians, Dr. Aaron A. Cohen-Gadol (neurosurgeon) and Dr. Eyas M. Hattab (neuropathologist), to the study design, specimen procurement, pathologic evaluation of specimens, and crucial insight into brain tumor treatment and diagnosis.

4.6 References

1. Ostrom QT, Gittleman H, Liao P, Rouse C, Chen Y, Dowling J, et al. CBTRUS Statistical Report: Primary Brain and Central Nervous System Tumors Diagnosed in the United States in 2007–2011. Neuro-Oncology. 2014 October 1, 2014;16(suppl 4):iv1-iv63.

2. Lacroix M, Abi-Said D, Fourney DR, Gokaslan ZL, Shi W, DeMonte F, et al. A multivariate analysis of 416 patients with glioblastoma multiforme: prognosis, extent of resection, and survival. Journal of neurosurgery. 2001;95(2):190-8.

3. Barceló-Coblijn G, Fernández JA. Mass spectrometry coupled to imaging techniques: the better the view the greater the challenge. Frontiers in Physiology. 2015;6(3):1-7.

4. Bogdanovic E. IDH1, lipid metabolism and cancer: Shedding new light on old ideas. Biochimica et Biophysica Acta (BBA)-General Subjects. 2015;1850(9):1781-5.

5. Beloribi-Djefaflia S, Vasseur S, Guillaumond F. Lipid metabolic reprogramming in cancer cells. Oncogenesis. 2016 01/25/online;5:e189.

6. Ifa DR, Eberlin LS. Ambient Ionization Mass Spectrometry for Cancer Diagnosis and Surgical Margin Evaluation. Clinical chemistry. 2016;62(1):111-23.

7. Balog J, Sasi-Szabó L, Kinross J, Lewis MR, Muirhead LJ, Veselkov K, et al. Intraoperative tissue identification using rapid evaporative ionization mass spectrometry. Science Translational Medicine. 2013;5(194):194ra93-ra93.

8. Eberlin LS, Dill AL, Golby AJ, Ligon KL, Wiseman JM, Cooks RG, et al. Discrimination of human astrocytoma subtypes by lipid analysis using desorption electrospray ionization imaging mass spectrometry. Angewandte Chemie. 2010;122(34):6089-92.

9. Eberlin LS, Norton I, Dill AL, Golby AJ, Ligon KL, Santagata S, et al. Classifying human brain tumors by lipid imaging with mass spectrometry. Cancer research. 2012;72(3):645-54.

10. Eberlin LS, Norton I, Orringer D, Dunn IF, Liu X, Ide JL, et al. Ambient mass spectrometry for the intraoperative molecular diagnosis of human brain tumors. Proceedings of the National Academy of Sciences. 2013;110(5):1611-6.

11. Calligaris D, Feldman DR, Norton I, Brastianos PK, Dunn IF, Santagata S, et al. Molecular typing of meningiomas by desorption electrospray ionization mass spectrometry imaging for surgical decision-making. International Journal of Mass Spectrometry. 2014;377:690-8.

12. Jarmusch AK, Pirro V, Baird Z, Hattab EM, Cohen-Gadol AA, Cooks RG. Lipid and metabolite profiles of human brain tumors by desorption electrospray ionization-MS. Proceedings of the National Academy of Sciences. 2016:201523306.

13. Eberlin LS, Ferreira CR, Dill AL, Ifa DR, Cheng L, Cooks RG. Nondestructive, histologically compatible tissue imaging by desorption electrospray ionization mass spectrometry. ChemBioChem. 2011;12(14):2129-32.

14. Pirro V, Eberlin LS, Oliveri P, Cooks RG. Interactive hyperspectral approach for exploring and interpreting DESI-MS images of cancerous and normal tissue sections. Analyst. 2012;137(10):2374-80.

15. Doeswijk T, Hageman J, Westerhuis J, Tikunov Y, Bovy A, van Eeuwijk F. Canonical correlation analysis of multiple sensory directed metabolomics data blocks reveals corresponding parts between data blocks. Chemometrics and Intelligent Laboratory Systems. 2011;107(2):371-6.

16. Eberlin LS, Ifa DR, Wu C, Cooks RG. Three-Dimensional Vizualization of Mouse Brain by Lipid Analysis Using Ambient Ionization Mass Spectrometry. Angewandte Chemie International Edition. 2010;49(5):873-6.

17. Preul MC, Caramanos Z, Collins DL, Villemure J-G, Leblanc R, Olivier A, et al. Accurate, noninvasive diagnosis of human brain tumors by using proton magnetic resonance spectroscopy. Nature Medicine. 1996;2(3):323-5.

18. Kinoshita Y, Yokota A. Absolute concentrations of metabolites in the human brain tumors using in vitro proton magnetic resonance spectroscopy. NMR in Biomedicine. 1997;10(1):2-12.

19. Soares D, Law M. Magnetic resonance spectroscopy of the brain: review of metabolites and clinical applications. Clinical radiology. 2009;64(1):12-21.

20. Kwock L. Proton Magnetic Resonance Spectroscopy and Spectroscopic Imaging of Primary Brain Tumors. Functional Brain Tumor Imaging: Springer; 2014. p. 143-67.

21. Moffett JR, Ross B, Arun P, Madhavarao CN, Namboodiri AM. N-Acetylaspartate in the CNS: from neurodiagnostics to neurobiology. Progress in Neurobiology. 2007;81(2):89-131.

22. Santagata S, Eberlin LS, Norton I, Calligaris D, Feldman DR, Ide JL, et al. Intraoperative mass spectrometry mapping of an onco-metabolite to guide brain tumor surgery. Proceedings of the National Academy of Sciences. 2014;111(30):11121-6.

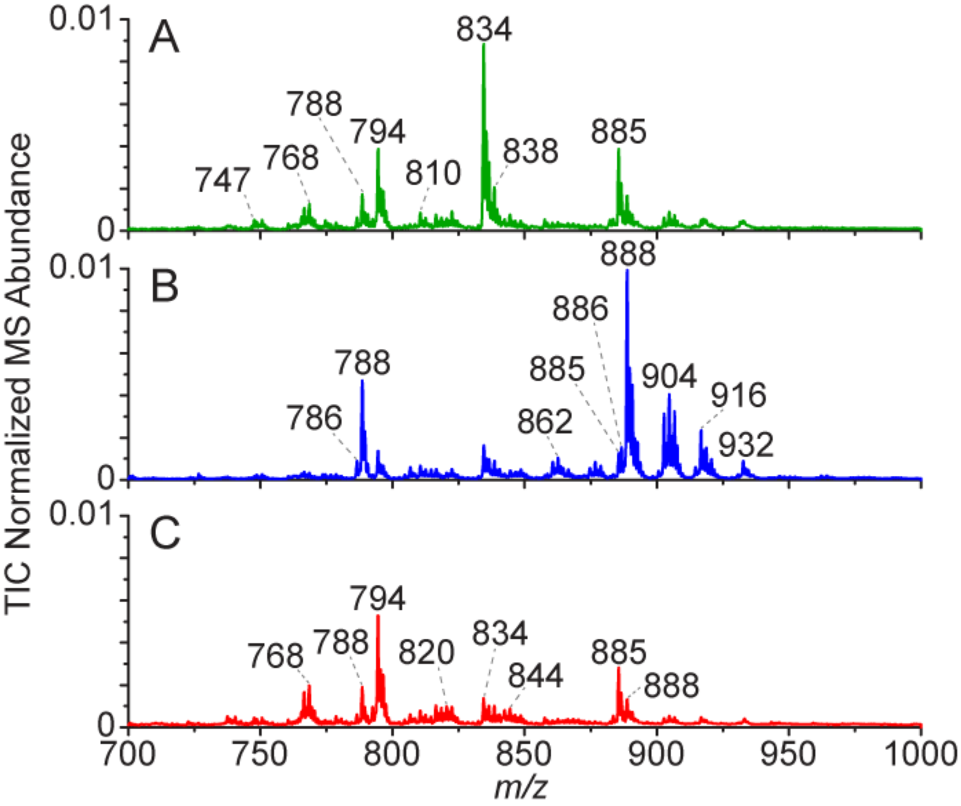

Figure 4-1. Average negative ion mode lipid MS profiles (*m/z* 700 - 1000) of (A) grey matter (green, N=223), (B) white matter (blue, N=66), and (C) glioma (red, N=158). The number of ROI is indicated by “N” and is the average spectrum recorded over a 1 mm by 1 mm area (16 pixels). The number of subjects from which the ROI originate is 58.

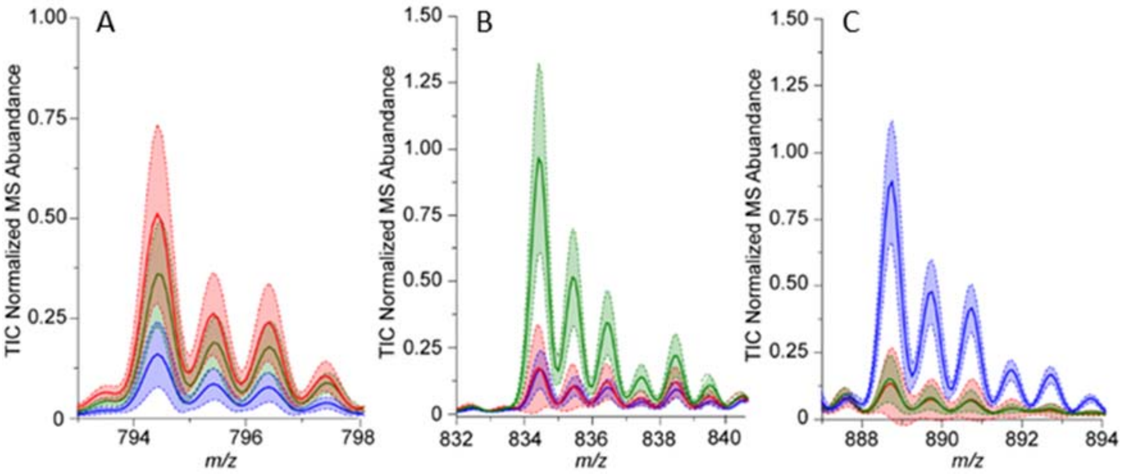

Figure 4-2. Plot of average negative ion mode mass spectra in selected mass windows. (A) *m/z* 794, PC 34:1+Cl$^-$, (B) *m/z* 834, PS 18:0_22:6, and (C) *m/z* 888, (3'-sulfo)GalCer 24:1, of grey matter (green), white matter (blue), and glioma (red). Mean denoted by solid line with ± standard deviation illustrated by the shaded area between the dotted lines.

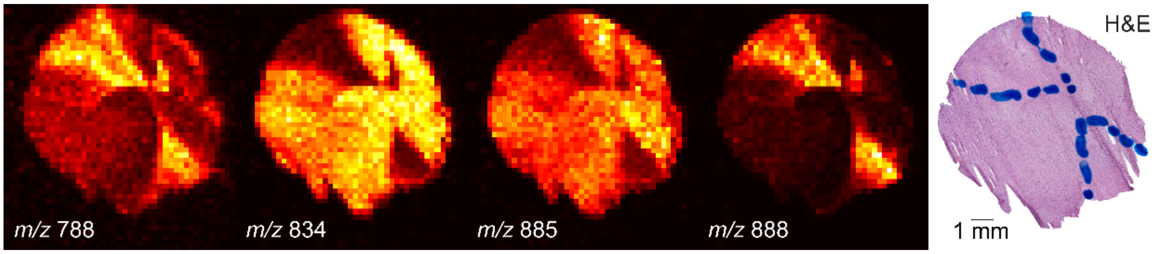

Figure 4-3. DESI-MS ion images of specimen 40 with selected lipid ions (maximum intensity plotted of each nominal *m/z*): *m/z* 788, 834, 885, and 888. Ion images are displayed in false-color, black to white (smallest to greatest intensity), and normalized to the maximum intensity of the ion plotted in each panel. Pixel size is 250 µm by 250 µm as defined by the DESI-MS imaging spatial resolution. H&E stain of analyzed tissue is shown.

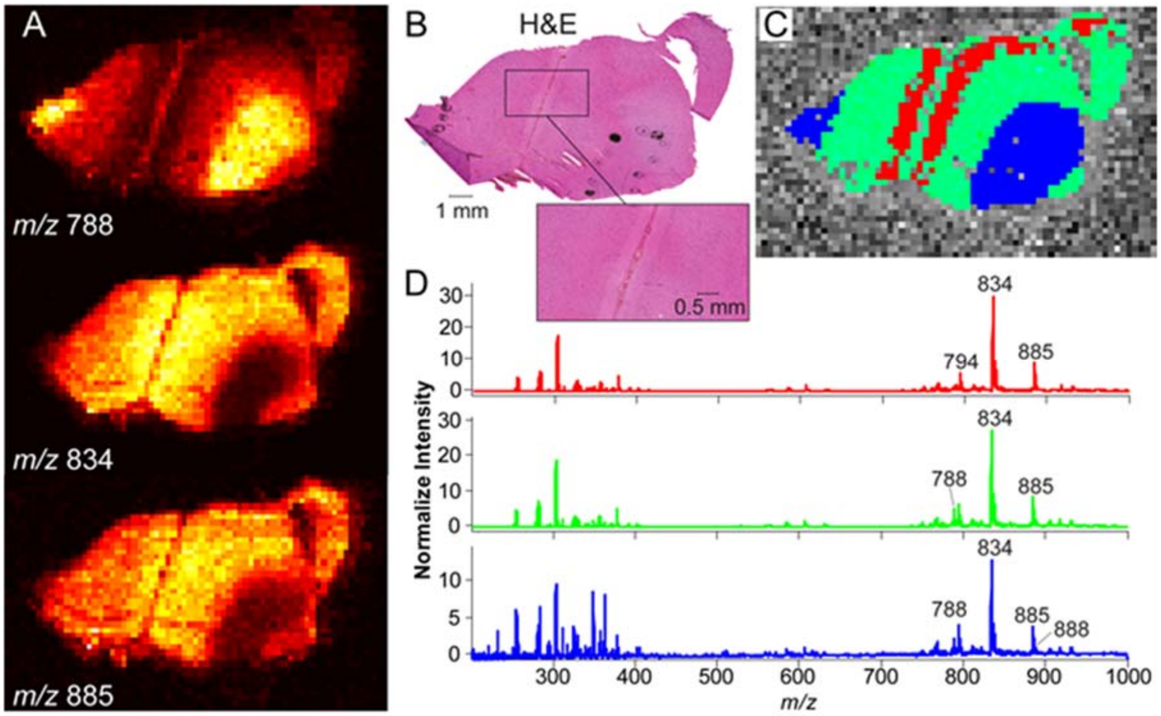

Figure 4-4. Chemical difference noted between neuroanatomical regions in specimen 44. (A) DESI-MS ion images of *m/z* 788, 834, and 885. Ion images are displayed in false-color, black to white (smallest to greatest intensity), and normalized to the maximum intensity of the nominal mass of each ion plotted. (B) H&E stain with annotated pathology, regions of white matter are annotated by pathologist in black marker. (C) Unsupervised multivariate recognition of the molecular layer, an anatomical substructure within the cortex (red); grey matter region (green); and white matter region (blue) via interactive brushing (colored image). (D) Average DESI-MS spectra obtained from interactive brushing selections.

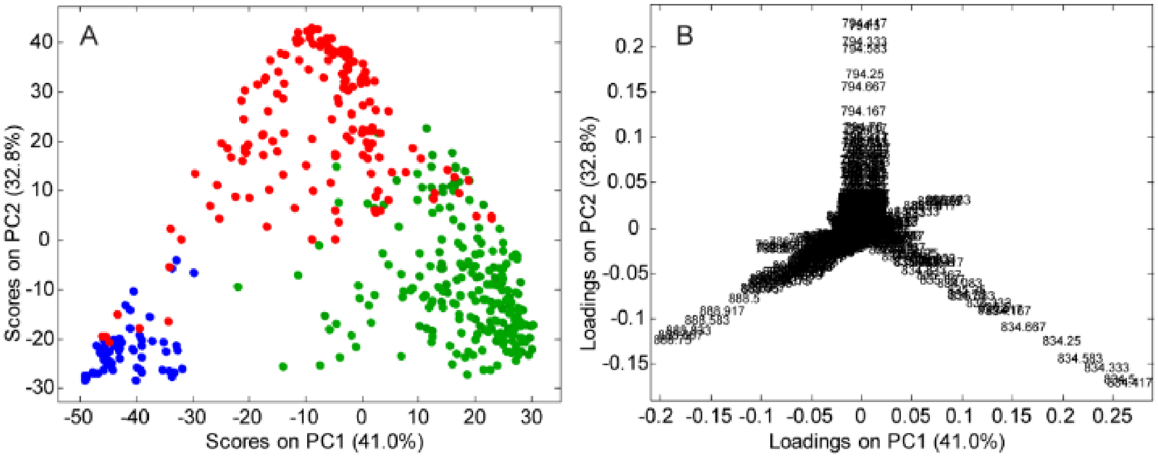

Figure 4-5. (A) PCA score plot using negative ion mode lipid profile information (*m/z* 700-1000) for grey matter (green circles), white matter (blue circles), and glioma (red circles). (B) PCA loading plot with *m/z* annotated.

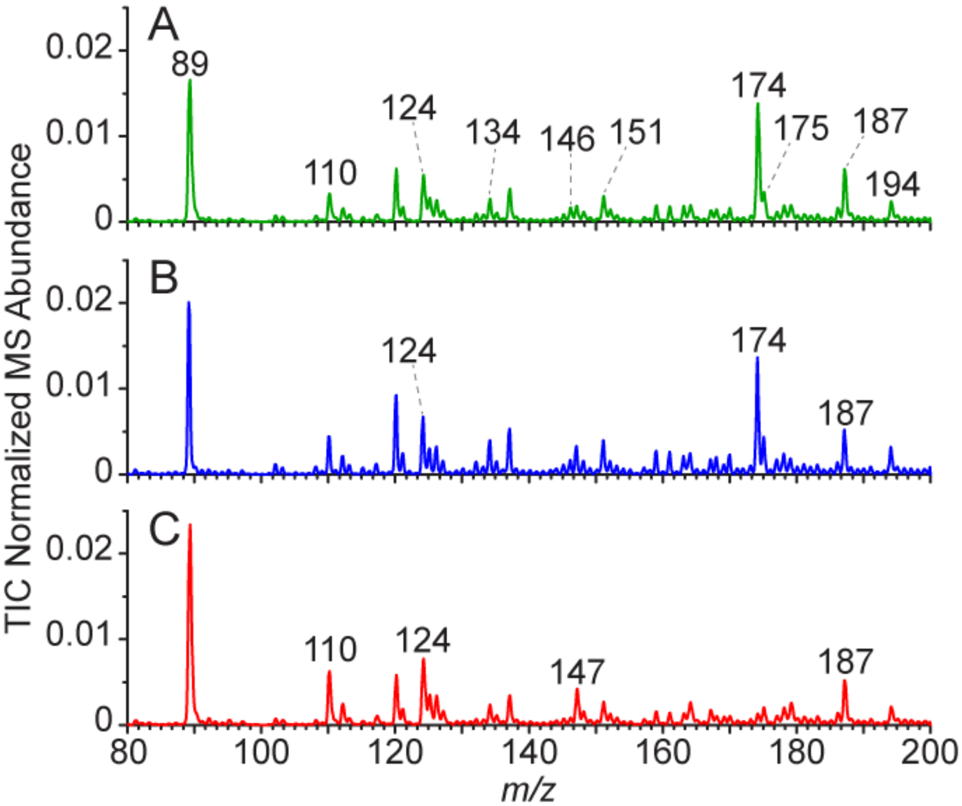

Figure 4-6. Average negative ion mode metabolite MS profiles (*m/z* 80 - 200) of (A) grey matter (green, N=223), (B) white matter (blue, N=66), and (C) glioma (red, N=158). The number of ROI is indicated by "N" and is the average spectrum recorded over a 1 mm by 1 mm area (16 pixels). The number of subjects from which the ROI originate is 58.

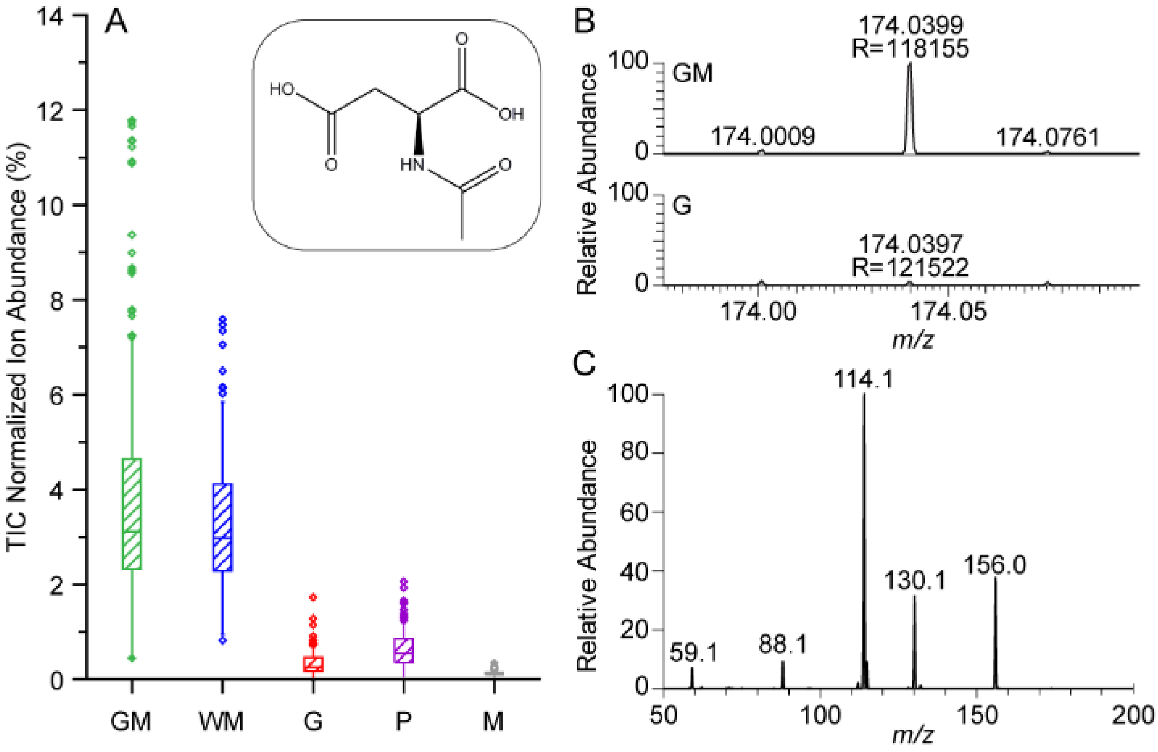

Figure 4-7. Statistical significance and identification of N-acetyl-aspartic acid, *m/z* 174 in the negative ion mode. (A) Box and whisker plot for *m/z* 174, NAA (structure inset): grey matter (GM), N=223; white matter (WM), N=66; glioma (G), N=158; pituitary (P), N=154; and meningioma (M), N=111. The box represents the interquartile range with median line and whiskers ±1.5 standard deviation with outliers represented by circles. (B) Detection of NAA by high resolution MS in grey matter (upper) and high grade glioma (lower) in specimen 51. Mass-to-charge and resolution are annotated. (C) CID-MS/MS fragmentation pattern obtained for NAA from grey matter in specimen 51.

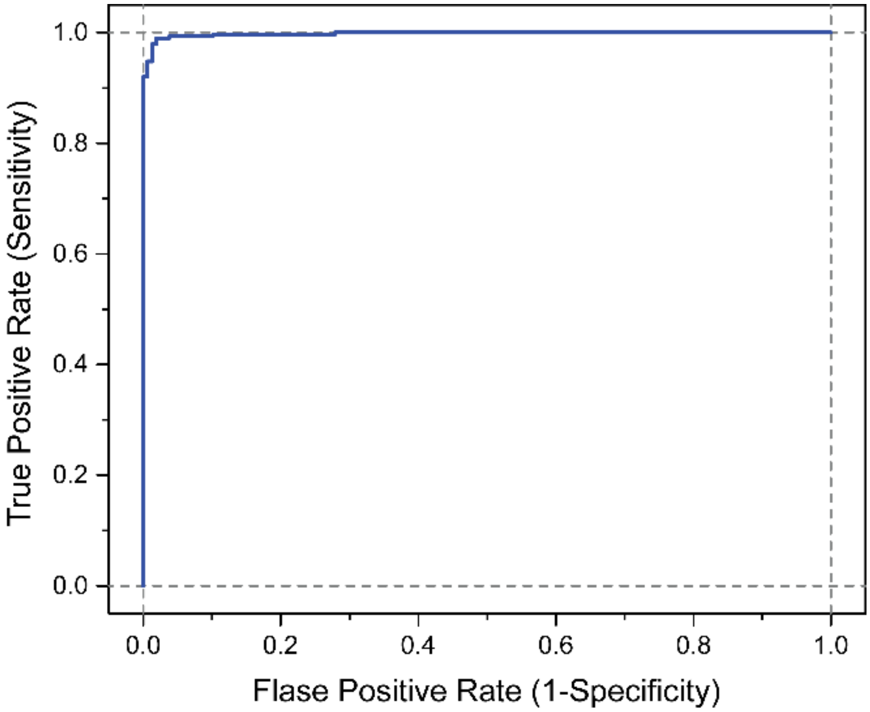

Figure 4-8. Receiver operating characteristic (ROC) curve of *m/z* 174 for brain parenchyma and glioma. The TIC normalized MS abundance collected in the negative ion mode metabolite profile was analyzed. The area under the curve was 0.998.

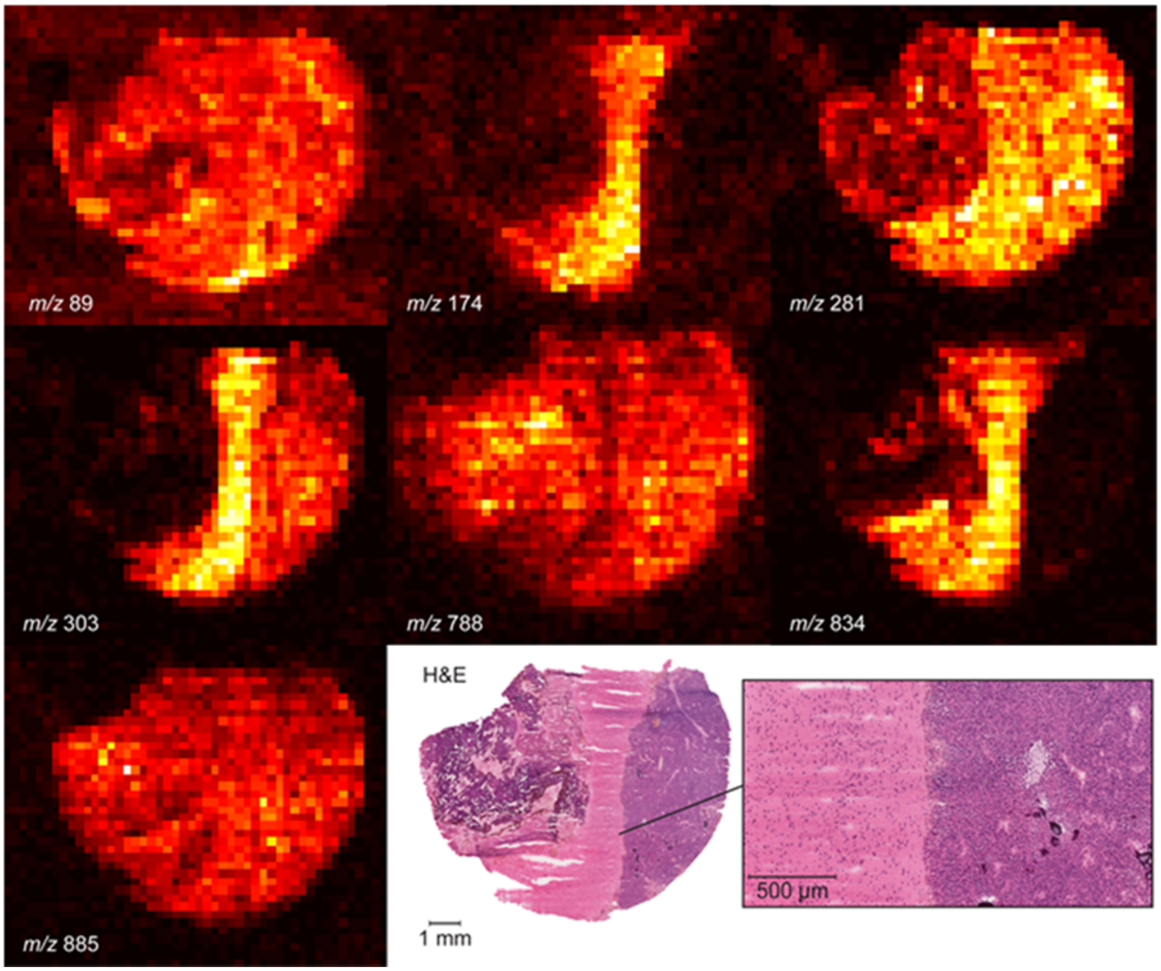

Figure 4-9. Specimen 20, negative ion mode DESI-MS ion images for *m/z* 89, 174, 281, 303, 788, 834, and 885. Ion images are compiled from metabolite (*m/z* 80 - 200) and lipid profiles (*m/z* 700 -1000), displayed in false-color, black to white (smallest to greatest intensity), and normalized to the maximum intensity of the ion plotted in each panel. H&E shows a region of cauterized tissue on the left and invasive meningioma on right with adjacent grey matter in between. Inset depicts the boundary between grey matter and meningioma.

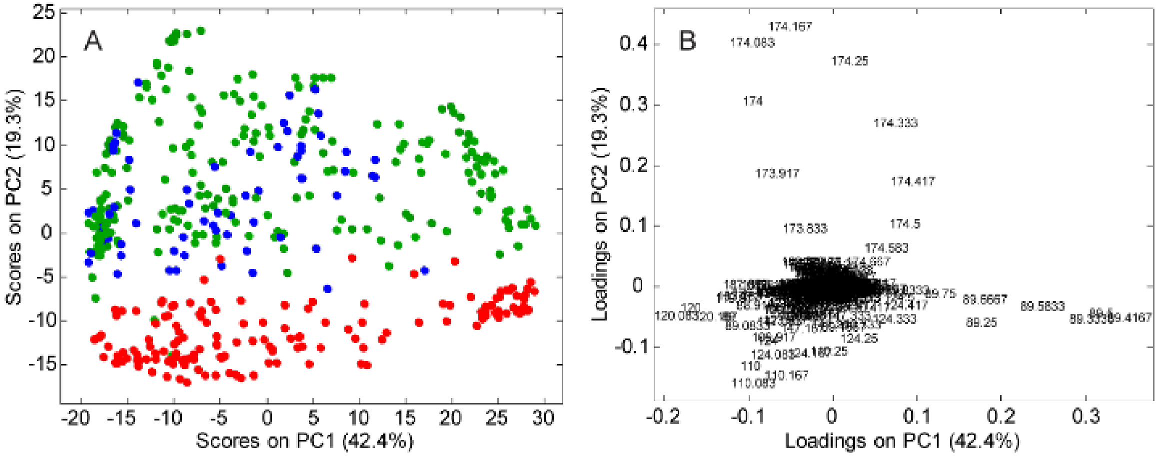

Figure 4-10. (A) PCA score plot using only negative ion mode metabolite profile information (*m/z* 80 - 200) for grey matter (green circles), white matter (blue circles), and glioma (red circles). (B) PCA loading plot with *m/z* annotated. Note the good separation of glioma but poor separation of grey and white matter from each other.

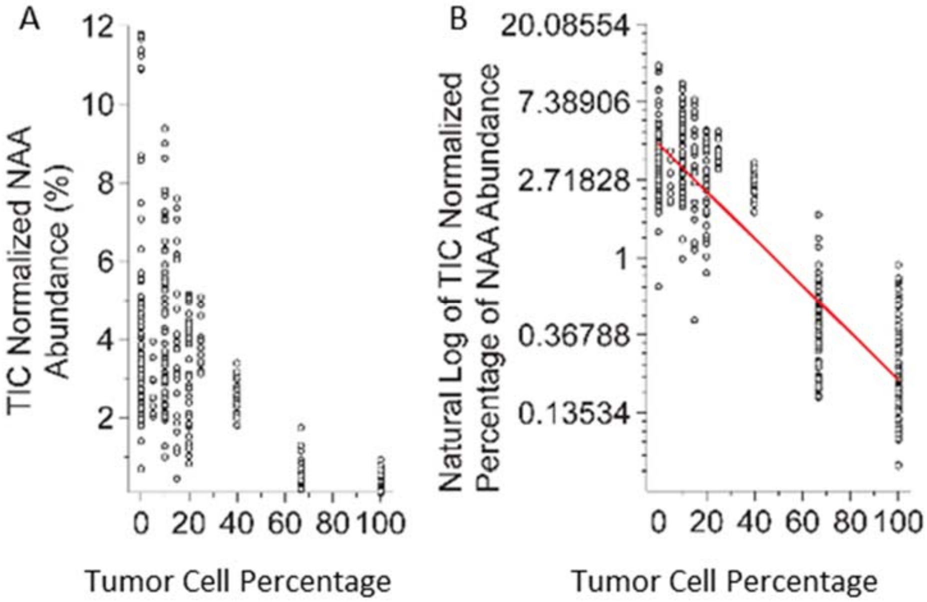

Figure 4-11. (A) The TIC normalized NAA abundance of grey matter, white matter, and glioma samples plotted versus tumor cell concentration. (B) Natural log of the TIC normalized NAA abundance versus tumor cell concentration with a line of regression (red line). The equation of the line was calculated as y = - 0.03x + 1.45 with a Pearson's r of - 0.89.

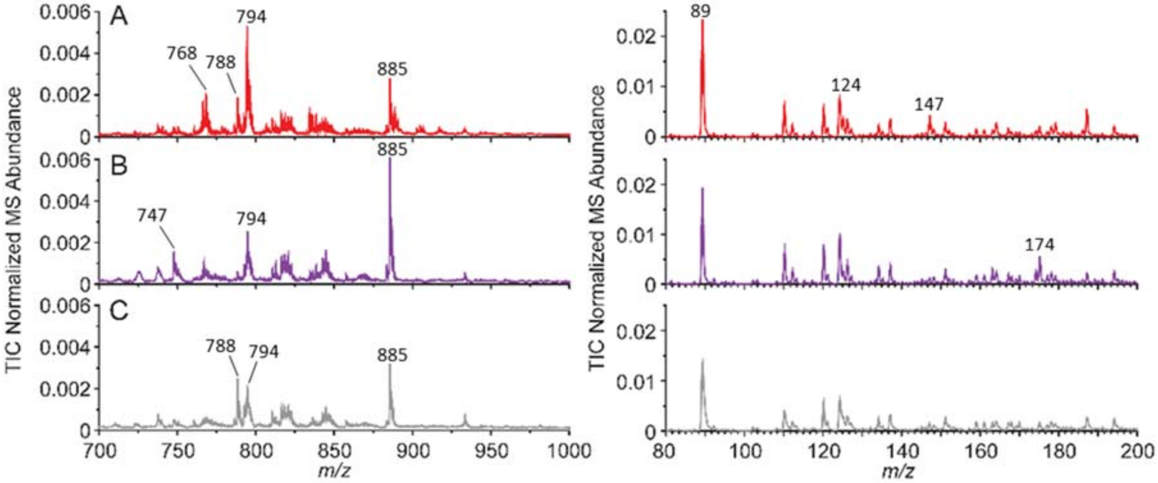

Figure 4-12. Average DESI mass spectra obtained from tissue sections for different tumor types. (A) Average lipid MS and (B) metabolite MS for glioma (red), pituitary tumors (purple), and meningiomas (grey). The primary ions were *m/z* 747 (PG 34:1), 768 (chloride adduct of PC 32:0), 788 (PS 36:1), 794 (chloride adduct of PC 34:1), 885 (PI 38:4), 89 (lactic acid), 147 (2-hydroxyglutaric acid), and 174 (n-acetyl-aspartic acid).

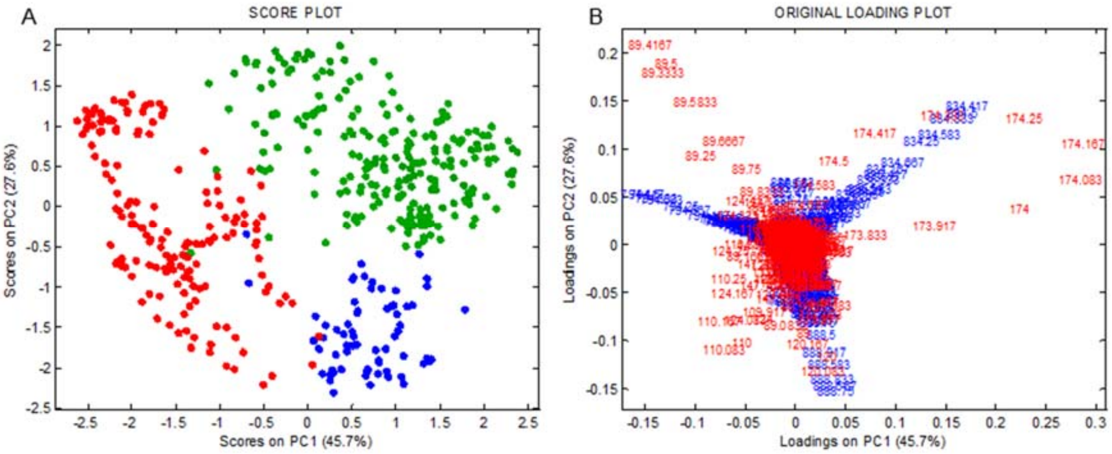

Figure 4-13. (A) PCA score plot resulting from mid-level data fusion of metabolite and lipid MS profiles. Grey matter (green), white matter (blue), and glioma (red). (B) PCA loading plot with metabolite ions (red) and lipid ions (blue).

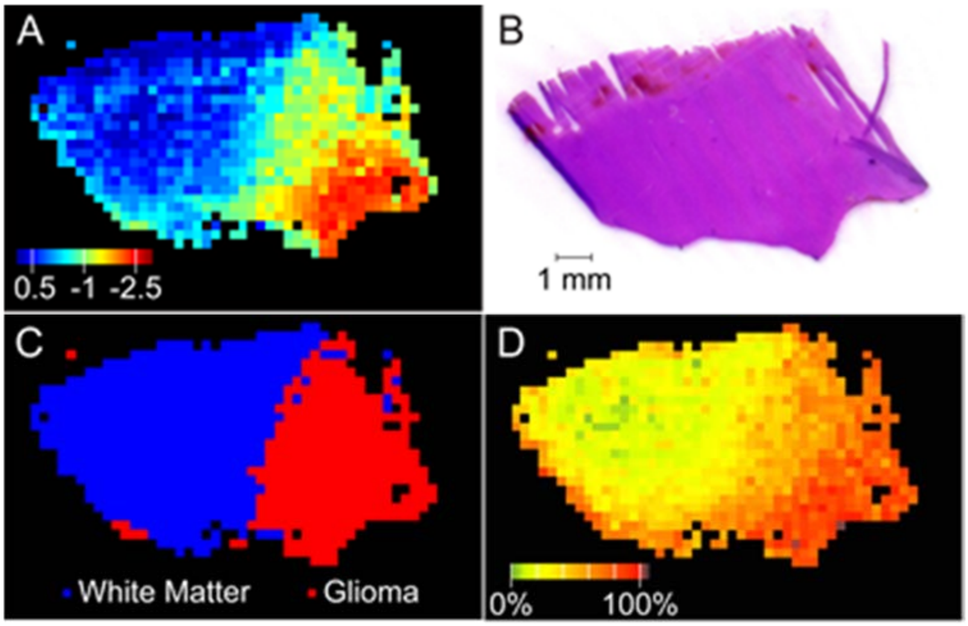

Figure 4-14. DESI-MS predictions for specimen 65 and corresponding H&E. (A) PCA projection, false-color, indicates PC1 score values. (B) Hematoxylin and eosin stain. (C) PCA-LDA prediction of class and (D) calculated tumor cell concentration based on NAA abundance.

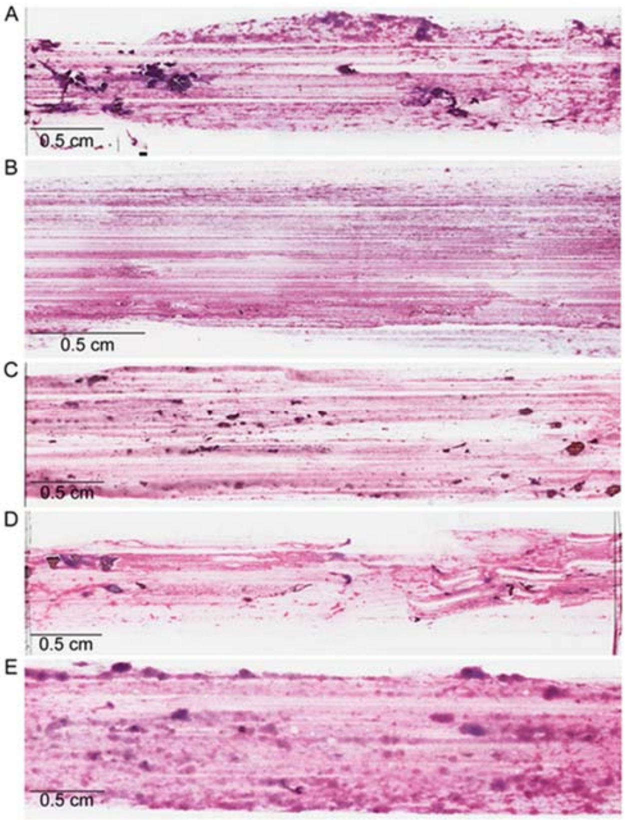

Figure 4-15. Examples of tissue smears analyzed by DESI and subsequently H&E stained: (A) specimen 51, (B) specimen 24, (C) specimen 20, (D) specimen 18, and (E) specimen 12.

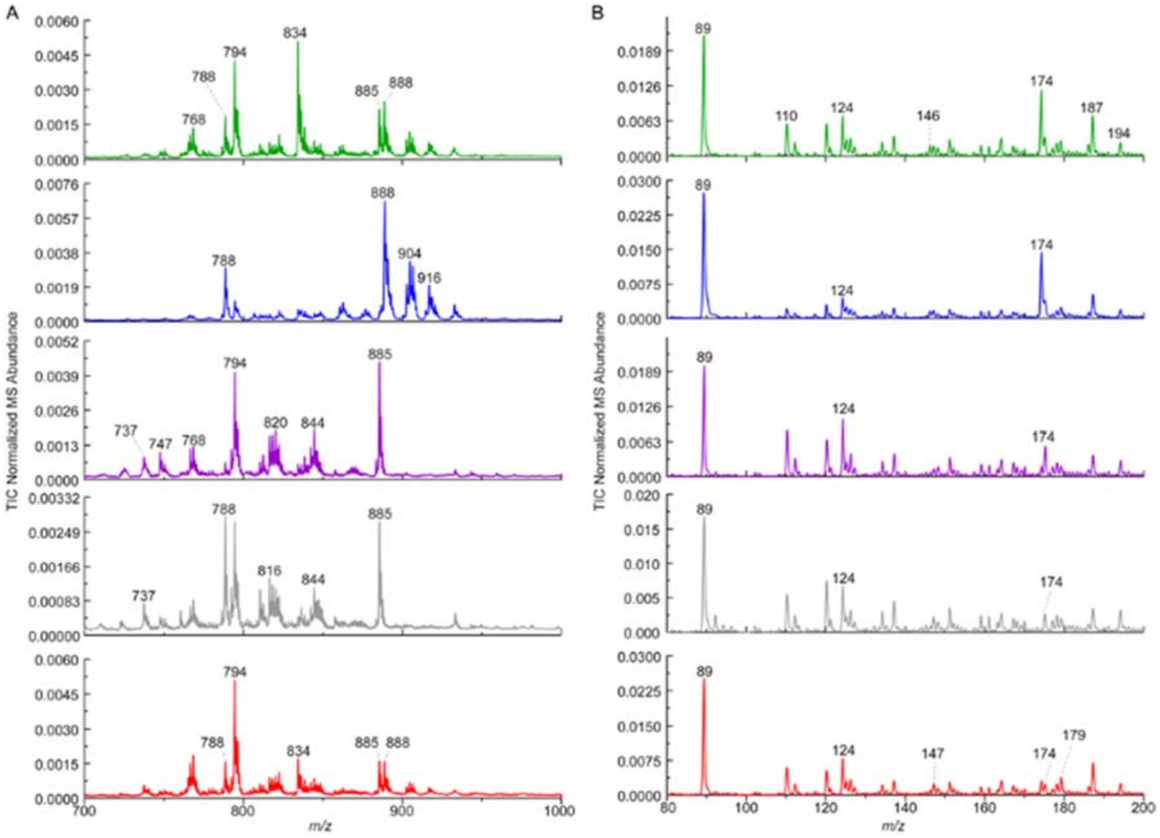

Figure 4-16. (A) Average DESI-MS lipid and (B) metabolite profile acquired from smears for grey matter (green), white matter (blue), pituitary (purple), meningioma (grey), and glioma (red). The primary ions were *m/z* 737, 747 (PG 34:1), 768 (chloride adduct of PC 32:0), 788 (PS 36:1), 794 (chloride adduct of PC 34:1), 834 (PS 40:6), 885 (PI 38:4), 888 ((3’-sulfo)GalCer 24:1), 89 (lactic acid), 147 (2-hydroxyglutaric acid), 174 (n-acetyl-aspartic acid), and 179 (C6 sugar).

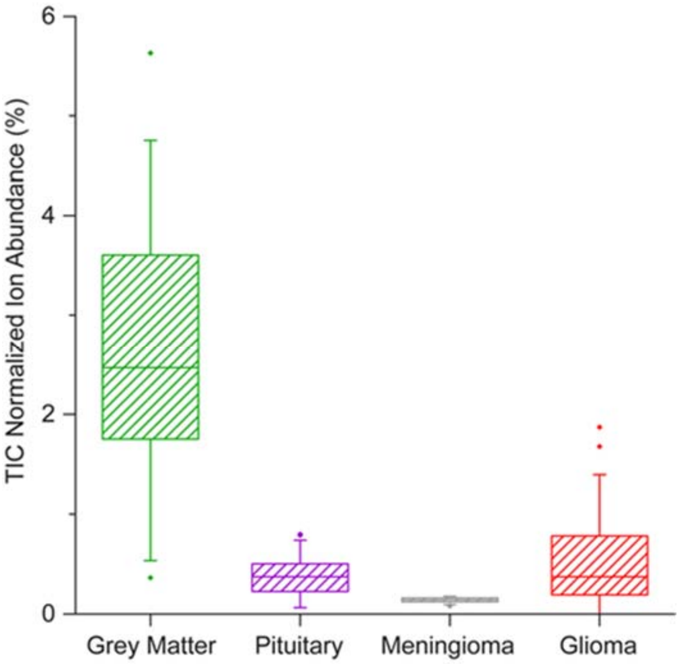

Figure 4-17. Box and whisker plot for *m/z* 174, NAA (negative ion mode), from the DESI-MS analysis of tissue smears. The box represents the interquartile range with median line and whiskers ±1.5 standard deviation with outliers represented by closed diamonds.

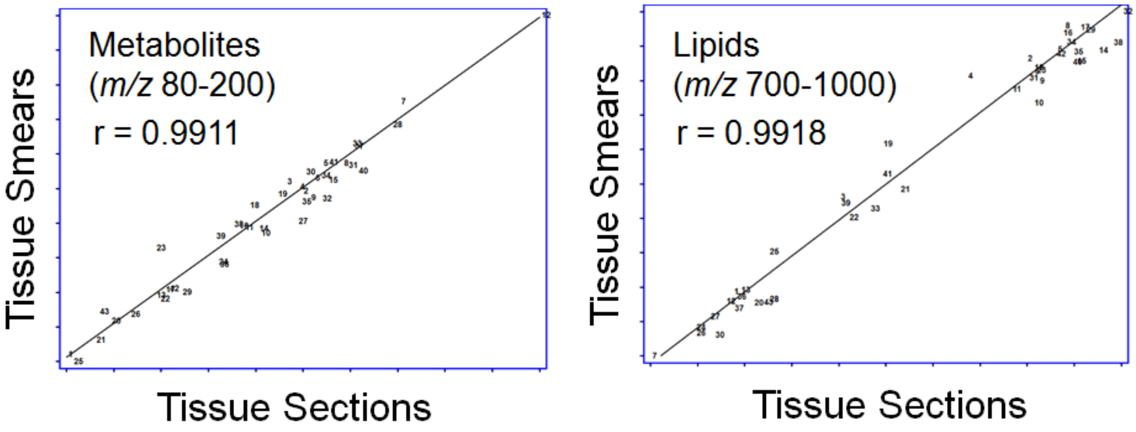

Figure 4-18. Correlation plot resulting from CCA performed between tissue sections and tissue smears upon (A) the metabolite MS profile and (B) the lipid MS profile.

Table 4-1. Tabulated DESI high resolution mass spectral data and ion identification for grey matter, white matter, and gliomas

			Grey Matter		White Matter		Glioma	
Name	Ion	Theoretical Mass	Mass Measured	Δ Mass (ppm)	Mass Measured	Δ Mass (ppm)	Mass Measured	Δ Mass (ppm)
Lactic acid	$[M\text{-}H]^-$	89.0239	89.0236	-3.4	89.0236	-3.4	89.0236	-3.4
2-hydroxyglutaric acid	$[M\text{-}H]^-$	147.0293	-	-	-	-	147.0288	-3.4
N-acetyl-aspartic acid	$[M\text{-}H]^-$	174.0402	174.0399	-1.7	174.0399	-1.7	174.0397	-2.9
C6 Sugar	$[M\text{-}H]^-$	179.0555	179.0552	-1.7	179.0552	-1.7	179.055	-2.8
Ascorbic acid	$[M\text{-}H]^-$	175.0242	175.0238	-2.3	175.0238	-2.3	175.0238	-2.3
Palmitic acid	$[M\text{-}H]^-$	255.2324	255.2322	-0.8	255.2324	0.0	255.2322	-0.8
Oleic acid	$[M\text{-}H]^-$	281.248	281.2479	-0.4	281.248	0.0	281.2479	-0.4
Stearic acid	$[M\text{-}H]^-$	283.2637	283.2635	-0.7	283.2636	-0.4	283.2635	-0.7
Arachidonic acid	$[M\text{-}H]^-$	303.2324	303.2322	-0.7	303.2323	-0.3	303.2322	-0.7
Docosahexaenoic acid	$[M\text{-}H]^-$	327.2324	327.2321	-0.9	327.2322	-0.6	327.2321	-0.9
PG 34:1	$[M\text{-}H]^-$	747.5176	747.5168	-1.1	747.5174	-0.3	-	-
PE 38:4	$[M\text{-}H]^-$	766.5386	766.5382	-0.5	-	-	766.5383	-0.4
PC 32:0	$[M+Cl]^-$	768.5309	-	-	-	-	768.5306	-0.4
PS 36:1	$[M\text{-}H]^-$	788.5441	788.5437	-0.5	788.5440	-0.1	788.5437	-0.5
PC 34:1	$[M+Cl]^-$	794.5466	794.5460	-0.8	794.5466	0.0	794.5462	-0.5
PS 40:6	$[M\text{-}H]^-$	834.5284	834.5279	-0.6	-	-	834.5280	-0.5
PI 38:4	$[M\text{-}H]^-$	885.5493	885.5486	-0.8	885.5492	-0.1	885.5486	-0.8
(3’-sulfo)GalCer 24:1	$[M\text{-}H]^-$	888.6234	-	-	888.6230	-0.5	-	-
(3’-sulfo)GalCer 24:1(OH)	$[M\text{-}H]^-$	904.6182	-	-	904.6181	-0.1	-	-

Table 4-2. Tabulated DESI high resolution mass spectral data and ion identification in meningiomas and pituitary tumors

			Meningioma		Pituitary Tumor	
Name	Ion	Theoretical Mass	Mass Measured	Δ Mass (ppm)	Mass Measured	Δ Mass (ppm)
Lactic acid	$[M-H]^-$	89.0239	89.0235	-4.5	89.0236	-3.4
2-hydroxyglutaric acid	$[M-H]^-$	147.0293	-	-	-	-
N-acetyl-aspartic acid	$[M-H]^-$	174.0402	-	-	-	-
C6 Sugar	$[M-H]^-$	179.0555	179.055	-2.8	179.0551	-2.2
Ascorbic acid	$[M-H]^-$	175.0242	-	-	175.0239	-1.7
Palmitic acid	$[M-H]^-$	255.2324	255.2323	-0.4	255.2323	-0.4
Oleic acid	$[M-H]^-$	281.248	281.2479	-0.4	281.2479	-0.4
Stearic acid	$[M-H]^-$	283.2637	283.2635	-0.7	283.2636	-0.4
Arachidonic acid	$[M-H]^-$	303.2324	303.2322	-0.7	303.2322	-0.7
Docosahexaenoic acid	$[M-H]^-$	327.2324	-	-	-	-
PG 34:1	$[M-H]^-$	747.5176	-	-	747.5172	-0.5
PE 38:4	$[M-H]^-$	766.5386	766.5381	-0.7	766.5383	-0.4
PC 32:0	$[M+Cl]^-$	768.5309	-	-	-	-
PS 36:1	$[M-H]^-$	788.5441	788.5436	-0.6	788.5440	-0.1
PC 34:1	$[M+Cl]^-$	794.5466	794.5461	-0.6	794.5456	-1.3
PS 40:6	$[M-H]^-$	834.5284	-	-	-	-
PI 38:4	$[M-H]^-$	885.5493	885.5486	-0.8	885.5488	-0.6
(3’-sulfo)GalCer 24:1	$[M-H]^-$	888.6234	-	-	-	-
(3’-sulfo)GalCer 24:1(OH)	$[M-H]^-$	904.6182	-	-	-	-

Table 4-3. Negative ion mode lipid profile PCA-LDA confusion matrix (5 deletion groups) for grey matter, white matter, and glioma with calculated sensitivity and specificity for each class.

		Histopathology		
		Grey Matter	White Matter	Glioma
DESI	Grey Matter	208	0	9
	White Matter	2	66	9
	Glioma	13	0	140
Sensitivity (%)		93.3	100.0	88.6
Specificity (%)		95.8	96.9	95.5

Table 4-4. Negative ion mode metabolite profile PCA-LDA confusion matrix (5 deletion groups) for grey matter, white matter, and glioma with calculated sensitivity and specificity for each class.

		Histopathology		
		Grey Matter	White Matter	Glioma
DESI	Grey Matter	129	25	0
	White Matter	86	38	1
	Glioma	8	3	157
Sensitivity (%)		57.8	57.6	99.4
Specificity (%)		88.6	76.7	93.8

Table 4-5. Negative ion mode lipid profile PCA-LDA confusion matrix (5 deletion groups) for glioma, meningioma, and pituitary tumors with calculated sensitivity and specificity for each class.

		Histopathology		
		Glioma	Meningioma	Pituitary
DESI	Glioma	155	0	0
	Meningioma	3	111	0
	Pituitary	0	0	154
Sensitivity (%)		98.1	100.0	100.0
Specificity (%)		100.0	99.0	100.0

Table 4-6. Mid-level fusion PCA-LDA confusion matrix (5 deletion groups, 2 principal components) for grey matter, white matter, and glioma with calculated sensitivity and specificity for each class.

		Histopathology		
		Grey Matter	White Matter	Glioma
DESI	Grey Matter	218	0	2
	White Matter	1	66	7
	Glioma	4	0	149
Sensitivity (%)		97.8	100.0	94.3
Specificity (%)		99.1	97.9	98.6

CHAPTER 5. FUSION OF POSITIVE AND NEGATIVE ION MODE LIPID PROFILES FOR DIFFERENTATION OF HUMAN BRAIN CANCER

5.1 Introduction

Ambient ionization mass spectrometry (MS) has the potential to improve tissue diagnosis and influence outcomes in patients undergoing surgical removal of cancer. Ambient ionization MS provides the opportunity to study biopsied tissue rapidly (seconds to minutes) and with minimal sample preparation (1). Currently, pathologic diagnosis of gliomas, the most common malignant brain tumor, is performed upon formalin-fixed surgical biopsies via histopathology. However, this cannot be done on a timescale amenable to surgical guidance. Frozen tissue histopathology is performed as an alternative to provide the surgeon information but can take upwards of 20 minutes per biopsy. Methodologies for rapid intraoperative molecular diagnosis are sparse, with noteworthy ongoing interest in Raman spectroscopy (2) and fluorescence (3); mass spectrometry, too, may meet this need. Several versions of ambient ionization MS have been tested for clinical applications. They include rapid evaporative MS for in vivo analysis of liver, lung, and colorectal cancers (4), desorption electrospray ionization (DESI) for detection of MRI contrast agents within tumors (5) and for analysis of frozen tissue sections, and substrate-based ambient ionization analysis of cancerous tissues; e.g., probe electrospray ionization (6) and touch spray (7, 8).

Lipids serve many physiological and structural functions and are increasingly being considered as disease markers in cancer. Previous studies of prostate (7), bladder (9), kidney (10), breast (11), lymphoma (12), and gastrointestinal cancer (13), amongst others, have demonstrated that DESI-MS lipid profiles (*m/z* values and corresponding relative ion abundances) in combination with multivariate statistics, allow differentiation of cancer from normal tissue as corroborated by traditional histopathologic diagnosis. Further, these lipid profiles are not prone to degradation in the native atmosphere over the timescale of analysis, and have so far proven to be sufficiently reproducible, provided the same DESI conditions and solvents are utilized (14). Lipid profiles acquired by DESI-MS analysis of human brain tumors have been studied previously; in particular those acquired in the negative ionization mode have been exploited for differentiating normal tissue from diseased (15) as well as for exploring the chemical differences among glioma grade. (16) Glioma subtype and tumor cell concentrations (i.e., relative percentage of tumor cells compared with normal cells) was also investigated. (17, 18). Differences in the positive ion mode DESI mass spectra between different glioma grades was previously noted, (16) but analysis of normal parenchyma and differentiation from diseased tissue using multivariate statistics was not undertaken.

Recent studies of oncometabolites in human brain tumors have demonstrated the usefulness of considering low molecular weight metabolites. Notable examples are 2-hydroxyglutaric acid (2-HG) (19) and N-acetyl-aspartic acid (NAA) (15). When the negative mode lipid profiles and additional sources of chemical information were used together, via data fusion, improved differentiation of cancer from normal brain parenchyma (i.e., grey and white matter) was obtained (15).

This study is founded on the hypothesis that the positive ion lipid profile obtained with DESI-MSI will provide complementary chemical information and, in combination with the negative ion lipid profile, improve differentiation of normal brain parenchyma and glioma. This manuscript reports sequentially acquired positive and negative ion mode DESI-MSI of tissue sections from 39 human subjects. Multivariate statistical analysis performed upon regions of interest (ROI) revealed that the positive and negative ion mode data contained differentiating information. Further, the information in the positive ion mode was nearly equivalent to the negative ion mode in regards to sensitivity and specificity. This work serves to establish the diagnostic potential of DESI-MS information in both the positive and negative ion modes, either or both of which can be transferred to intrasurgical measurements.

5.2 Experimental

5.2.1 Materials

Banked frozen tissue specimens from 39 human subjects were studied in accordance with Purdue IRB protocol (#1410015344). Specimens were cryosectioned (15 μm thickness) and thaw mounted onto glass microscope slides. All tissue sections were stored at –80°C prior to analysis. Tissue sections adjacent to those used in a prior study (15) were used in the study of the positive ion mode lipid profiles. Blind pathologic evaluation was subsequently performed on all tissue sections analyzed by DESI-MS. In most cases, the histopathologic evaluation did not change; however, some areas were slightly smaller or larger between two tissue sections. Pathology provided disease state (e.g. grey matter, white matter, or glioma), grade (sometimes), and tumor cell percentage (TCP).

5.2.2 Methods

5.2.2.1 Positive and Negative Ion Mode Lipid Profiles via DESI-MS Imaging

DESI-MSI was performed on a linear ion trap mass spectrometer as described in 5.2.2.1. The mass spectrometer was tuned for maximum transmission of *m/z* 786 (dioleoylphosphatidylcholine) and 735 (dipalmitoylphosphatidylcholine) in the negative and positive ion modes, respectively. Dimethylformamide-acetonitrile (1:1 v/v) was used for DESI-MS imaging. DESI source parameters are as follows: solvent flow rate, 1.0 µL min^{-1}; pressure of nitrogen gas, 160 PSI; applied high voltage, -5.0 kV negative mode and +4.5 kV in the positive mode; incident angle, 52°; spray-to-surface distance, 2 - 3 mm; spray-to-inlet distance, 5 - 7 mm. In-source collision energy (35V) was applied in the positive and negative mode. Images were collected in a series of rows by coordinating linear motion of the moving stage (431.034 µm s^{-1}) with MS duty cycle. The MS duty cycle was defined by the scan parameters: *m/z* 200-1000, injection time of 500 ms with 1 microscan, and automatic gain control (AGC) was disabled. A lateral spatial resolution (“x”) of 250 µm was defined, upon completion of a row the moving stage resets to the original “x” position while stepping 250 µm in “y”. This process was repeated in order to acquire data from the entire tissue surface. The positive-mode was chosen first as ions detected were typically sodium or potassium adducts, and by imaging for positive ions first we minimized any changes in adduct formation due to prior analysis. Conversely, this was less of a concern in the negative mode as many of the ions were detected as deprotonated species; however, important chloride adducts of PCs were also detected (e.g. *m/z* 794).

5.2.2.2 Data Analysis

ROI were selected in MATLAB (MathWorks, Natick, MA USA) based on histopathologic review of the tissue after MS analysis; each ROI selection was the average spectrum of 1 mm (4 pixels) by 1 mm (4 pixels), which permitted accurate correlation of the spatial and chemical information. The set of tissue used sections provided 585 ROI; 32 selections were removed as they contained significant amounts of ions related to Optimal Cutting Temperature Polymer in the spectra (S1 Fig). The remaining selections were examined by principal component analysis from *m/z* 700 - 1000; the exclusion of lower *m/z* values improved separation as the lower mass-to-charge signals (e.g., fatty acids) were more variable in intensity. Multivariate statistics was performed using MATLAB routines and is detailed in the supplementary information. Tentative attributions of *m/z* values to specific lipid structures were made based on

HRMS and MS/MS. The statistical results are independent of lipid identification: only the full scan mass-to-charge value and corresponding MS abundance are considered.

5.3 Results and Discussion

5.3.1 Sequential Positive and Negative Ionization Mode DESI-MS Imaging

Lipid metabolism has been shown to be significantly different in cancerous and non-cancerous cells and tissues due to the roles of lipids in cell growth, membrane fluidity, cell adhesion, and energy production (20). The analysis of biological specimens in both MS polarities provides greater coverage of the lipidome; i.e., the totality of lipids in a cell, tissue, or an organism. The lipids detected in this study are primarily membrane phospholipids including phosphatidylcholine (PC), phosphatidylethanolamine (PE), sphingomyelin (SM), ceramide (Cer), phosphatidylserine (PS), phosphatidylinositol (PI), and sulfatide (ST). Some classes of membrane lipids preferentially ionize in the positive ion mode (e.g., PC and SM) and others in the negative ion mode (e.g., phosphatidic acids, PI, and PS) depending largely on the functionality of the polar headgroup (21). We hypothesize that it is advantageous to maximize the acquired lipid information by acquiring data in both polarities to characterize different disease states (e.g., cancer) in order to increase diagnostic accuracy.

Janfelt et al. recently demonstrated acquisition of positive and negative DESI-MS data from the same specimen by alternating MS polarity every other line in the imaging experiment (22). Their solvent system (methanol-water 19:1) destroys tissue samples during analysis, precluding subsequent analysis or staining of the same tissue specimen. We modified their approach by using morphology preserving solvents (e.g., DMF-ACN [1:1]) which allowed the same tissue section to be imaged multiple times using DESI-MS and subsequently stained for histopathology. Further, the same tissue section was analyzed twice in succession, once in the positive and then in the negative ionization mode, with mass spectra from *m/z* 200 – 1000 being obtained from each MS image pixel. The acquisition of data in subsequent images, as opposed to line-by-line polarity switching (22), reduces problems that might arise from incomplete charge equilibration and thus spray stability is improved.

Representative DESI-MS ion images for an illustrative specimen, 3003EPE, are reported in Figure 5-1. Specimen 3003EPE is comprised of a glioma region near the bottom of the tissue section with adjacent grey and white matter regions, determined by histopathology, and marked approximately in Figure 5-1. Particular ions were relatively more abundant in different histological regions; for example, *m/z* 798 ($[\text{PC } 34{:}1 + \text{K}]^+$), 848 ($[\text{GalCer d}32{:}2 + \text{K}]^+$), and 772 ($[\text{PE P-}38{:}5 + \text{Na}]^+$), in the positive ion mode (Figure 5-1) appear to be relatively more abundant in grey matter, white matter, and glioma, respectively. The selected ion images are a small sampling of the many ions that appear to be differentially abundant in the different histologic regions. Negative ions characteristic of grey matter (*m/z* 834, PS 40:6), white matter (*m/z* 888, (3’-sulfo)GalCer 24:1), and glioma (*m/z* 794, chloride adduct of PC 34:1) were also observed at different abundances (Figure 5-1). The distributions of *m/z* 834 and *m/z* 888 in grey and white matter, respectively, agree with prior DESI-MSI studies of human (15) and other mammalian brains (23), as well as other ambient ionization methods such as scanning probe electrospray ionization (24). The combination of the positive and negative mode ion images provided visually distinct regions which matched well with histopathologic evaluation.

5.3.2 Positive Ion Mode Lipid Profiles of Human Brain Matter and Gliomas

The average positive mode lipid profiles for grey matter, white matter, and glioma are visually different (Figure 5-2, respectively). Grey matter is associated with a greater abundance of *m/z* 772 ($[\text{PC } 32{:}0 + \text{K}]^+$) and 798 ($[\text{PC } 34{:}1 + \text{K}]^+$). White matter appears to have greater abundances of *m/z* 750 ($[\text{GalCer d}36{:}1 + \text{K}]^+$ and $[\text{PE P-}36{:}2 + \text{Na}]^+$), 832 ($[\text{GalCer d}32{:}2 + \text{Na}]^+$), and 848 ($[\text{GalCer d}32{:}2 + \text{K}]^+$). Interestingly, gliomas appear to have greater abundances of *m/z* 754 ($[\text{PC } 32{:}1 + \text{Na}]^+$), 756 ($[\text{PC } 32{:}0 + \text{Na}]^+$), and 782 ($[\text{PC } 34{:}1 + \text{Na}]^+$). Tentative identifications were based on high resolution MS and MS/MS, Table 5-1. The data show that in some cases multiple lipid species are present in a single nominal mass peak (e.g., *m/z* 750, $[\text{PE P-}36{:}2 + \text{Na}]^+$), while other peaks are principally due to a single lipid species (e.g., *m/z* 754, $[\text{PC } 32{:}1 + \text{Na}]^+$). The measured profiles were consistent within classes given potential biological and analytical variation. The differences between classes were typically greater than the standard deviation of the average spectrum for ions important in distinguishing the class. The observed increase in total PC abundance is consistent with magic angle spinning nuclear magnetic analysis of glioma tissue (25) and reported changes in PC metabolism. (26, 27) A greater abundance of SMs and ceramides in white matter versus grey matter has also been reported (28). Plasmalogens (e.g., 750) have been reported to compose approximately 50% and 85% of the PE fraction in grey and white matter, respectively (29, 30). In addition, multiple metal adducts of the same lipid (e.g., *m/z* 782 and 798) were detected and are likely due to differences in the concentration of the adducting species (e.g., Na^+ and K^+) and that of the analyte (e.g., PC 34:1), matrix effects, and intrinsic ionization efficiency differences. Regardless, the differences in ion abundance are consistent between classes and appear to differentiate normal parenchyma from glioma.

The positive ion mode data were analyzed by principal component analysis (PCA), an unsupervised multivariate statistical method, resulting in separation of grey matter (green points), white matter (blue points), and glioma (red points) (Fig 2). Separation of the groups in the PCA score plot of principal component 1 (PC1) vs PC2 (Figure 5-2) was less clear than separation in the PCA score plot of PC2 vs PC3 (Fig 2F). The ions contributing to the observed separation in the PCA score plot are displayed in the corresponding PCA loading plots (Figure 5-2). The ions displayed in the PCA loading plots recapitulate differences in the average mass spectra for grey matter, white matter, and gliomas (Fig 2A–C, respectively). Linear discriminant analysis (LDA) was performed after compression of the variables by PCA to estimate the predictive ability of the positive ionization mode DESI-MSI data. PCA-LDA cross validation (six principal components, five deletion groups) resulted in an average sensitivity and specificity of all classes (grey matter, white matter, and glioma) of 93.2% and 96.6%, respectively. The sensitivity and specificity of each class is tabulated in Table 5-2. These values only provide an estimate of prediction performance; a study with a larger sample set is required for further validation but is beyond the scope of this paper.

5.3.3 Negative Ion Mode Lipid Profiles of Human Brain Matter and Gliomas

The presence of *m/z* 834 ([PS 40:6 – H]$^-$) and 888 ([3′-sulfo GalCer 24:1 – H]$^-$) are indicative of grey and white matter, respectively (Figure 5-3). Additional predominant ions include *m/z* 788 (PS 36:1), 794 ([PC 34:1 + Cl]$^-$), 885 (PI 38:4), and 906 ((3′-sulfo) GalCer 24:0(2OH)). Gliomas appear to have suppressed levels of *m/z* 834 and 888 relative to the grey and white matter average spectra, and therefore appear to have a visually distinct lipid profile (Figure 5-3). Tentative identifications are based on previously published results (15, 17). PCA was performed on the negative ionization mode DESI-MSI data, and the resulting score and loading plots are displayed in Figure 5-3. The separation of grey matter (green points), white matter (blue points), and glioma (red points) as well as their lipid profiles are consistent with previous results (15) which utilized the same tissue specimens. The similarity of the results is encouraging because analyses were performed one year apart. The continuum of points observed between the main grey and white matter groupings in the PCA score plot of Figure 5-3, reflect mixtures of grey and white matter that are present in normal neuroanatomy (31). Similarly, the points which fall in between the normal parenchyma and glioma groupings represent glioma infiltration into adjacent matter which is well known (32, 33). Points (ROIs) falling in between the main groups had convoluted lipid profiles and support the presence of mixed compositions of grey, white matter, and glioma. For example, Figure

5-4 shows an illustrative mass spectrum for a mixture of grey and white matter. In spite of the continuum between grey matter, white matter, and glioma, good separation is observed in additional PCA score plots; e.g., PC2 vs PC3 (Figure 5-3). The PCA loading plots (Figure 5-3) display the importance of specific ions in the separations seen in the PCA score plots.

Negative ionization mode PCA-LDA cross validation (six PCs, five deletion groups) resulted in an average sensitivity of 94.1% and specificity of 97.4%. The sensitivity and specificity of individual classes can be found in Table 5-3. The average values are consistent with unreported PCA-LDA results from our prior study which lie within ~5% (15). Overall, the average positive and negative ionization mode sensitivity and specificity values are similar and appear to be equivalently useful in separating grey matter, white matter, and gliomas. The notable differences when comparing the classes individually are as follows: the sensitivity of gliomas in the positive mode was higher than the negative mode (93.0% versus 88.1%), respectively, while the sensitivity of white matter was lower (89.8%, positive mode, versus 95.9%, negative mode). The specificity of grey matter was greater in the negative mode than the positive mode (98.8% versus 92.2%); the specificity of white matter was higher in the positive mode, 99.7%, than in the negative mode, 93.9%. Comparison of the positive and negative mode cross validation results show that each mode provides complementary diagnostic information, while the average sensitivity and specificity of all classes are similar.

5.3.4 Fusion of Positive and Negative Mode Lipid Profiles

Midlevel data fusion was applied considering the first six principal components. PCA of the fused data resulted in clearer separation of grey matter, white matter, and glioma, as shown in Figure 5-5. The improved separation reduced overlap between the groupings (e.g., grey matter and glioma). Separation was also noted in additional PCA score plots (Figure 5-7). Interestingly, the glioma class was split into two subgroups, one closely associated with the white matter group and one more closely associated with the grey matter group (approximately delineated left-to-right at a PC1 score of 0 in Figure 5-5). The glioma subgroups were not apparent in the positive or negative mode lipid profiles individually or in our prior study in which data for the lipids and metabolites in the negative ion mode were fused (15). The ROIs of each glioma subgroup were averaged and are displayed in Figure 5-6. The negative mode lipid profile of the grey matter–associated glioma subgroup was similar to previously reported glioma profiles (15, 18) and contained neither *m/z* 834 nor 888 at any appreciable abundance. The negative mode lipid profile of the white matter–associated glioma subgroup was similar to the negative mode white matter lipid profile. The positive mode lipid profiles for the two subgroups were visually different from those of normal grey and white matter. The PCA loading plot (Figure 5-5) offers a basic understanding of the correlation between positive and negative ions; vectors of similar direction indicate a positive correlation; e.g., *m/z* 798 (positive mode) and 834 (negative mode) are important in separating grey matter. Similarly, *m/z* 832 (positive mode) and 888 (negative mode) are important in separating white matter. The loading plot does not reveal deeper relationships (e.g., biological reason) for the correlation between ions, only that they are correlated in separating the groups.

PCA-LDA was performed on the fused data (six principal components, five deletions groups) and resulted in the following cross validation results (Table 5-4). The average sensitivity and specificity of all classes was 94.7% and 97.6%, respectively. These values are not substantially different than the positive or negative mode separately. However, the sensitivity and specificity of individual classes was improved with no value falling below 90%. Fusion of the data in some cases did slightly decrease the sensitivity or specificity of individual classes compared to the positive or negative mode results; e.g., specificity of white matter: fused (95.1%), positive mode (99.7%), and negative mode (93.9%). The PCA-LDA results support that information in the positive and negative lipid profiles are complementary and aid in more confidently distinguishing grey matter, white matter, and glioma.

5.3.5 DESI-MS Detection of Tumor Cell Percentage

Tumor cell percentage (TCP), previously dubbed tumor cell concentration, is a means by which to measure glioma infiltration. Its interrelationship with the lipid profiles is poorly understood except that it is partially responsible for the spread of points in the PCA score plots between groupings. The TCP, estimated via histopathology, was plotted (Figure 5-8); the PCA score plot indicated that the majority of the grey matter associated glioma subgroup was of medium to high TCP (regions defined as $33\%<x<67\%$ and $>67\%$, respectively) whereas the white matter associated glioma subgroup was comprised of ROIs with low (<33%) to medium TCP. The grey matter associated glioma subgroup was better separated than the white matter associated glioma subgroup from their respective normal groupings, potentially the effect of a relatively higher TCP. Further, tumor grade and TCP are not completely independent as gliomas of higher grade (WHO III and IV) tend to have greater TCP; differences between tumor grades, plotted in Figure 5-8, cannot be commented upon in this study due to the low number of low grade gliomas (WHO I and II).

The complex nature of the molecular diagnosis of gliomas is illustrated in specimen 3003KDE which contained regions of different TCP (40–60%). Illustrative ROI mass spectra are displayed in Figure 5-9. The positive and negative spectra of the ROI associated with 60% TCP is less reminiscent of white matter than the spectra from the 40% TCP region. The ROIs of 3003KDE were projected onto the fusion PCA score plot (Figure 5-10) using a technique similar to that described in Bagnaso et al. (34) The ROIs associated with lower TCP in 3003KDE were projected within the white matter group while the ROIs associated with 60% TCP were projected within the white matter–associated glioma subgroup. Similarly, specimen 3003ETP, a heterogeneous tissue section, was comprised of a higher TCP glioma region (~80%) and a lower density tumor (10% TCP) in mostly grey matter (one small area of white matter was also present) (Figure 5-11). The ROI associated with the 80% TCP region of 3003ETP lay within the grey matter associated glioma subgroup, while the ROI associated with the 10% TCP grey matter region lay within the grey matter group. Note, ROI 13 lay between the grey matter and white matter groups and corresponds to a selection near a grey and white matter boundary.

Lipid changes associated with glioma, detected in the positive and negative mode lipid profiles, appear to be too attenuated to be a useful discriminator in areas of lower tumor cell percentage. Given that the future objective of this work is to assist in surgical resection, it is necessary to measure TCP levels at the surgical resection margin which may be in the 10–40% range, although no current information exists as to the actual proportion of tumor cells at the surgical margin. Current practice determines resection completeness via contrast enhanced MRI, which is an improvement over visual inspection (35); however, this methodology relies on uptake of radiocontrast agent, can be confounded by intracranial volume changes, and cannot be used to interrogate specific regions that the neurosurgeon finds pathologically suspicious. For glioblastoma patients, there is controversy as to the effect of completeness of tumor resection and patient survival because the infiltrative nature of glioblastoma renders total surgical resection an impossible task with current surgical techniques (36). Even in tissues that appear histologically normal, malignant glioma cells can be isolated and cultured. Indeed, the site of tumor recurrence is often within two centimeters of the resection margin from non-enhancing areas observed in MRI (37, 38). However, studies have shown that near-total tumor resection for low grade glioma patients significantly increases patient survival and time to malignant progression (39, 40). Optimization and evaluation of the DESI-MS methodology to assist the surgeon in checking discrete areas within the operative field for residual tumor, via the determination of TCP based on DESI-MS lipid profiles, is the subject of future work.

5.3.6 DESI-MS Analysis of Morphologically Effaced Tissue Sections

DESI-MSI could also be used to complement glioma diagnosis (particularly on frozen sections) as tumors commonly efface normal tissue morphology such that the background parenchyma cannot be definitively identified. For example, we found in specimen 3003UVH that the DESI-MS data could be used to determine the background parenchyma when histopathology was inconclusive (Figure 5-12). Chemically, it was quite clear that the background parenchyma of specimen 3003UVH was white matter due to the presence of *m/z* 888. Such lipid information provided by DESI-MSI could be useful in clarifying current histopathologic evaluation and potentially enhance detection of glioma infiltration in tissue sections.

5.4 Conclusions

The serial acquisition of DESI-MS images in the positive and negative modes provided spatial and chemical information (i.e., lipid profiles) that differentiated human grey matter, white matter, and gliomas. The positive ion mode lipid profiles are reproducible and allow differentiation of grey matter, white matter, and gliomas with an average sensitivity and specificity of 93.2% and 96.6%, respectively. The inclusion of normal brain parenchyma samples and differentiation via multivariate statistics expand upon prior work which explored the differences in the positive mode lipid profile between different glioma grades and subtypes (16). The positive ion mode lipid profiles yielded approximately the same differentiation ability as the negative ion lipid profiles. The repeatability of the acquired lipid profiles is illustrated by the similarity of the negative ion mode PCA, average mass spectra, and PCA-LDA cross validation results with that of a prior study (15). Our hypothesis was supported as the complementary chemical information obtained from the positive and negative mode analyses slightly improved PCA separation of grey matter, white matter, and glioma when used together via data fusion. The fused data analyzed by PCA-LDA provided an average sensitivity of 94.7% and specificity of 97.6%, and the individual class values all exceeded 90%. Diagnosis of effaced glioma tissue specimens is complex, but DESI-MS lipid profiles were able to suggest, chemically, the background matter in such specimens. It is foreseeable that providing pathologists with supplemental DESI-MSI information would increase their diagnostic confidence. Regarding use in the surgical resection of gliomas, we observed the influence of glioma infiltration (assessed as TCP) on the lipid profiles and discussed the possible uses and limitations of this measurement. The limited ability of the lipid profiles to determine lower TCP emphasizes the need for further improvement to the current DESI-MS and multivariate statistical methods. One candidate solution is to combine the negative and positive ion mode lipid profiles with chemical measurements of oncometabolites, such as NAA, that distinguish normal and cancerous neural tissue with high sensitivity and specificity. We envision that the intraoperative use of DESI-MS, collecting positive and negative mode lipid and metabolite data, will comprise an *ex vivo* tool to check discrete areas of tissue which are pathologically ambiguous by visual inspection, potentially augmenting current surgical practice.

5.5 Acknowledgements

I would like to acknowledge the equal contribution of Clint M. Alfaro to study design, data collection, and data analysis. Thanks is owed to Dr. Valentina Pirro for her assistance with bioinformatics. The final member of the Purdue team that I would like to thank is my advisor, Dr. R. Graham Cooks. I would also like to thank Dr. Aaron A. Cohen-Gadol (neurosurgeon) and Dr. Eyas M. Hattab (neuropathologist) for the contributions to this study.

5.6 References

1. Ifa DR, Eberlin LS. Ambient Ionization Mass Spectrometry for Cancer Diagnosis and Surgical Margin Evaluation. Clinical chemistry. 2016;62(1):111-23.

2. Jermyn M, Mok K, Mercier J, Desroches J, Pichette J, Saint-Arnaud K, et al. Intraoperative brain cancer detection with Raman spectroscopy in humans. Sci Transl Med. 2015 Feb 11;7(274):274ra19. PubMed PMID: 25673764.

3. Diaz RJ, Dios RR, Hattab EM, Burrell K, Rakopoulos P, Sabha N, et al. Study of the biodistribution of fluorescein in glioma-infiltrated mouse brain and histopathological correlation of intraoperative findings in high-grade gliomas resected under fluorescein fluorescence guidance. J Neurosurg. 2015 Jun;122(6):1360-9. PubMed PMID: 25839919. Epub 2015/04/04. eng.

4. Balog J, Sasi-Szabo L, Kinross J, Lewis MR, Muirhead LJ, Veselkov K, et al. Intraoperative tissue identification using rapid evaporative ionization mass spectrometry. Sci Transl Med. 2013 Jul 17;5(194):194ra93. PubMed PMID: 23863833. English.

5. Tata A, Zheng J, Ginsberg HJ, Jaffray DA, Ifa DR, Zarrine-Afsar A. Contrast agent mass spectrometry imaging reveals tumor heterogeneity. Analytical chemistry. 2015;87(15):7683-9.

6. Mandal MK, Saha S, Yoshimura K, Shida Y, Takeda S, Nonami H, et al. Biomolecular analysis and cancer diagnostics by negative mode probe electrospray ionization. Analyst. 2013;138(6):1682-8.

7. Kerian K, Jarmusch A, Pirro V, Koch M, Masterson T, Cheng L, et al. Differentiation of prostate cancer from normal tissue in radical prostatectomy specimens by desorption electrospray ionization and touch spray ionization mass spectrometry. Analyst. 2015;140(4):1090-8.

8. Alfaro CM, Jarmusch AK, Pirro V, Kerian KS, Masterson TA, Cheng L, et al. Ambient ionization mass spectrometric analysis of human surgical specimens to distinguish renal cell carcinoma from healthy renal tissue. Analytical and Bioanalytical Chemistry. 2016:1-8.

9. Dill AL, Eberlin LS, Costa AB, Zheng C, Ifa DR, Cheng L, et al. Multivariate statistical identification of human bladder carcinomas using ambient ionization imaging mass spectrometry. Chemistry-a European Journal. 2011;17(10):2897-902.

10. Dill AL, Eberlin LS, Zheng C, Costa AB, Ifa DR, Cheng L, et al. Multivariate statistical differentiation of renal cell carcinomas based on lipidomic analysis by ambient ionization imaging mass spectrometry. Analytical and Bioanalytical Chemistry. 2010;398(7-8):2969-78.

11. Calligaris D, Caragacianu D, Liu X, Norton I, Thompson CJ, Richardson AL, et al. Application of desorption electrospray ionization mass spectrometry imaging in breast cancer margin analysis. Proceedings of the National Academy of Sciences. 2014;111(42):15184-9.

12. Jarmusch AK, Kerian KS, Pirro V, Peat T, Thompson CA, Ramos-Vara JA, et al. Characteristic lipid profiles of canine non-Hodgkin's lymphoma from surgical biopsy tissue sections and fine needle aspirate smears by desorption electrospray ionization–mass spectrometry. Analyst. 2015;140(18):6321-9.

13. Eberlin LS, Tibshirani RJ, Zhang J, Longacre TA, Berry GJ, Bingham DB, et al. Molecular assessment of surgical-resection margins of gastric cancer by mass-spectrometric imaging. Proceedings of the National Academy of Sciences. 2014;111(7):2436-41.

14. Dill AL, Eberlin LS, Costa AB, Ifa DR, Cooks RG. Data quality in tissue analysis using desorption electrospray ionization. Analytical and bioanalytical chemistry. 2011;401(6):1949-61.

15. Jarmusch AK, Pirro V, Baird Z, Hattab EM, Cohen-Gadol AA, Cooks RG. Lipid and metabolite profiles of human brain tumors by desorption electrospray ionization-MS. Proceedings of the National Academy of Sciences. 2016:201523306.

16. Eberlin LS, Dill AL, Golby AJ, Ligon KL, Wiseman JM, Cooks RG, et al. Discrimination of human astrocytoma subtypes by lipid analysis using desorption electrospray ionization imaging mass spectrometry. Angewandte Chemie. 2010;122(34):6089-92.

17. Eberlin LS, Norton I, Dill AL, Golby AJ, Ligon KL, Santagata S, et al. Classifying human brain tumors by lipid imaging with mass spectrometry. Cancer research. 2012;72(3):645-54.

18. Eberlin LS, Norton I, Orringer D, Dunn IF, Liu X, Ide JL, et al. Ambient mass spectrometry for the intraoperative molecular diagnosis of human brain tumors. Proceedings of the National Academy of Sciences. 2013;110(5):1611-6.

19. Santagata S, Eberlin LS, Norton I, Calligaris D, Feldman DR, Ide JL, et al. Intraoperative mass spectrometry mapping of an onco-metabolite to guide brain tumor surgery. Proceedings of the National Academy of Sciences. 2014;111(30):11121-6.

20. Santos CR, Schulze A. Lipid metabolism in cancer. Febs Journal. 2012;279(15):2610-23.

21. Wang C, Wang M, Han X. Applications of mass spectrometry for cellular lipid analysis. Molecular BioSystems. 2015;11(3):698-713.

22. Janfelt C, Wellner N, Hansen HS, Hansen SH. Displaced dual-mode imaging with desorption electrospray ionization for simultaneous mass spectrometry imaging in both polarities and with several scan modes. Journal of Mass Spectrometry. 2013;48(3):361-6.

23. Eberlin LS, Ferreira CR, Dill AL, Ifa DR, Cooks RG. Desorption electrospray ionization mass spectrometry for lipid characterization and biological tissue imaging. Biochimica et Biophysica Acta (BBA)-Molecular and Cell Biology of Lipids. 2011;1811(11):946-60.

24. Otsuka Y, Naito J, Satoh S, Kyogaku M, Hashimoto H, Arakawa R. Imaging mass spectrometry of a mouse brain by tapping-mode scanning probe electrospray ionization. Analyst. 2014;139(10):2336-41.

25. Righi V, Roda JM, Paz J, Mucci A, Tugnoli V, Rodriguez-Tarduchy G, et al. 1H HR-MAS and genomic analysis of human tumor biopsies discriminate between high and low grade astrocytomas. NMR biomed. 2009;22(6):629-37.

26. Bogdanovic E. IDH1, lipid metabolism and cancer: Shedding new light on old ideas. Biochimica et Biophysica Acta (BBA)-General Subjects. 2015;1850(9):1781-5.

27. Jain M, Nilsson R, Sharma S, Madhusudhan N, Kitami T, Souza AL, et al. Metabolite profiling identifies a key role for glycine in rapid cancer cell proliferation. Science. 2012;336(6084):1040-4.

28. O'Brien JS, Sampson EL. Lipid composition of the normal human brain: gray matter, white matter, and myelin. Journal of lipid research. 1965;6(4):537-44.

29. Braverman NE, Moser AB. Functions of plasmalogen lipids in health and disease. Biochimica et biophysica acta. 2012 Sep;1822(9):1442-52. PubMed PMID: 22627108. Epub 05/26. eng.

30. Han X, Holtzman DM, McKeel DW, Jr. Plasmalogen deficiency in early Alzheimer's disease subjects and in animal models: molecular characterization using electrospray ionization mass spectrometry. J Neurochem. 2001 May;77(4):1168-80. PubMed PMID: 11359882. Epub 05/22. eng.

31. Paus T, Collins D, Evans A, Leonard G, Pike B, Zijdenbos A. Maturation of white matter in the human brain: a review of magnetic resonance studies. Brain research bulletin. 2001;54(3):255-66.

32. Swanson KR, Alvord EC, Jr., Murray JD. A quantitative model for differential motility of gliomas in grey and white matter. Cell proliferation. 2000 Oct;33(5):317-29. PubMed PMID: 11063134. Epub 11/04. eng.

33. Claes A, Idema AJ, Wesseling P. Diffuse glioma growth: a guerilla war. Acta neuropathologica. 2007;114(5):443-58.

34. Bagnasco L, Zotti M, Sitta N, Oliveri P. A PCA-based hyperspectral approach to detect infections by mycophilic fungi on dried porcini mushrooms (boletus edulis and allied species). Talanta. 2015;144:1225-30.

35. Senft C, Bink A, Franz K, Vatter H, Gasser T, Seifert V. Intraoperative MRI guidance and extent of resection in glioma surgery: a randomised, controlled trial. The lancet oncology. 2011;12(11):997-1003.

36. Keles GE, Anderson B, Berger MS. The effect of extent of resection on time to tumor progression and survival in patients with glioblastoma multiforme of the cerebral hemisphere. Surgical neurology. 1999 Oct;52(4):371-9. PubMed PMID: 10555843. Epub 11/11. eng.

37. Giese A, Westphal M. Treatment of malignant glioma: a problem beyond the margins of resection. Journal of cancer research and clinical oncology. 2001 Apr;127(4):217-25. PubMed PMID: 11315255. Epub 04/24. eng.

38. De Bonis P, Anile C, Pompucci A, Fiorentino A, Balducci M, Chiesa S, et al. The influence of surgery on recurrence pattern of glioblastoma. Clinical neurology and neurosurgery. 2013;115(1):37-43.

39. Smith JS, Chang EF, Lamborn KR, Chang SM, Prados MD, Cha S, et al. Role of extent of resection in the long-term outcome of low-grade hemispheric gliomas. Journal of Clinical Oncology. 2008;26(8):1338-45.

40. Berger MS, Deliganis AV, Dobbins J, Keles GE. The effect of extent of resection on recurrence in patients with low grade cerebral hemisphere gliomas. Cancer. 1994 Sep 15;74(6):1784-91. PubMed PMID: 8082081. Epub 09/15. eng.

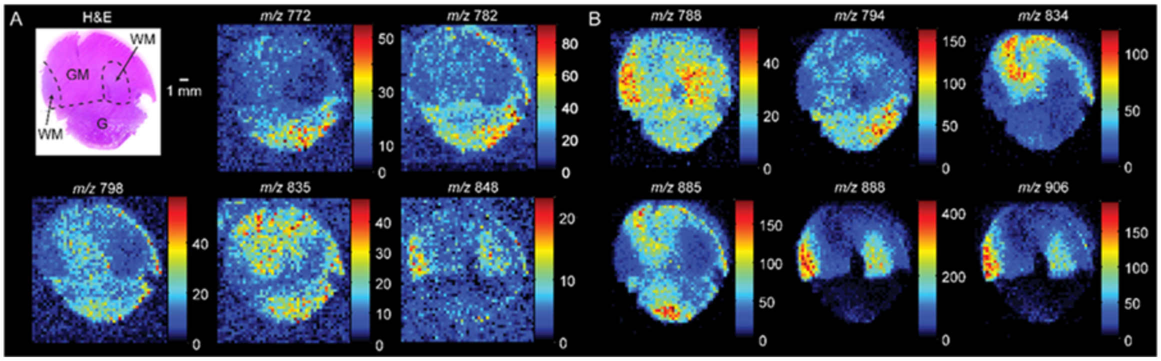

Figure 5-1. (A) Representative positive ionization mode ion images of specimen 3003EPE and (B) representative negative mode ion images. The false-color ion images are scaled to the greatest intensity of the ion plotted in each image, the scale bar indicates the absolute MS abundance (counts) detected. Scanned H&E-stained tissue sections with regions of grey matter (GM), white matter (WM), and glioma (G) approximated based on histopathology.

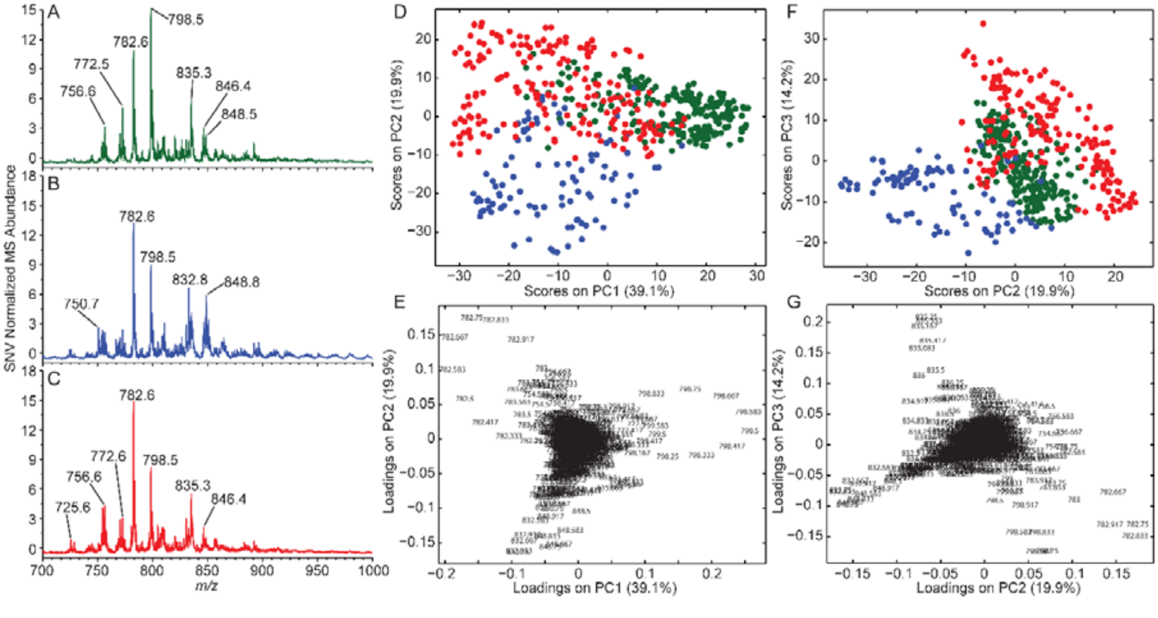

Figure 5-2. Average positive ion mode DESI spectra (*m/z* 700 – 1000) for (A) grey matter, n=223; (B) white matter, n=98; and (C) gliomas, n=185. (D and F) PCA score plots: grey matter (green), white matter (blue), and glioma (red). (E and G) PCA loading plots with ion *m/z* annotated.

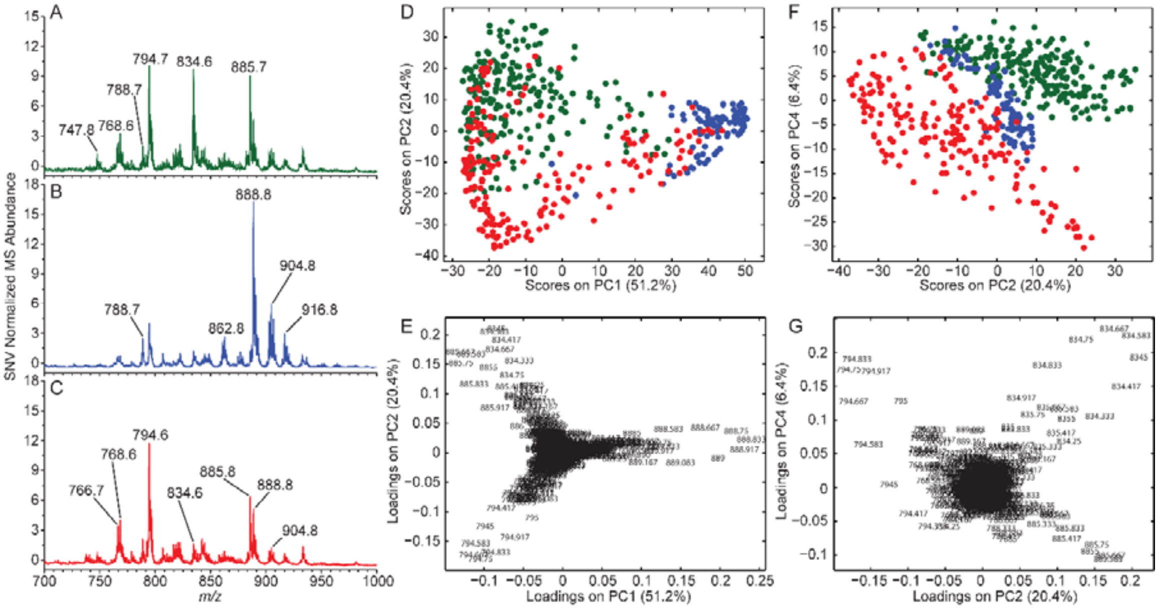

Figure 5-3. Average negative-mode DESI spectra (*m/z* 700 – 1000) for (A) grey matter, n=223; (B) white matter, n=98; and (C) gliomas, n=185. (D and F) PCA score plots and corresponding (E and G) PCA loading plots. Grey matter, white matter, and glioma are green, blue, and red in the PCA score plot, respectively. The *m/z* of each ion is annotated in the PCA loading plot.

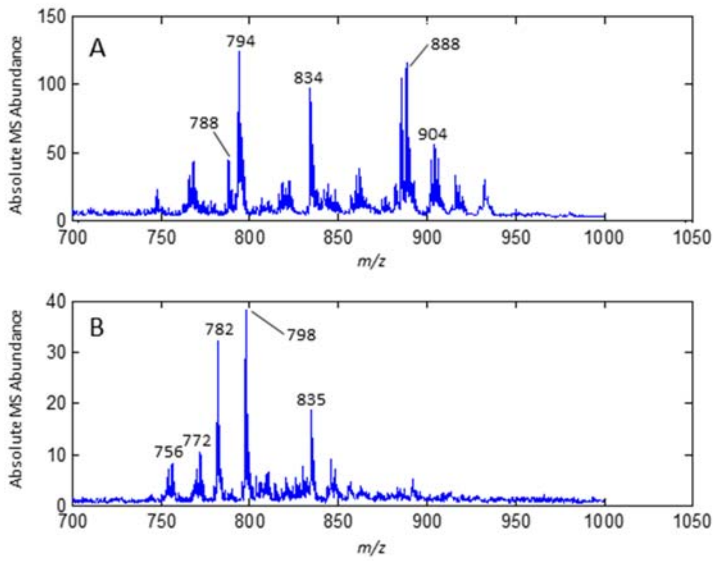

Figure 5-4. Illustrative (A) negative and (B) positive ion mode DESI-MS spectra (*m/z* 700 – 1000) from a ROI of mixed grey and white matter composition. Both *m/z* 834 and 888 are abundant in the negative ion mode. Similarly, the positive mode lipid profile appears to be a combination of grey and white matter.

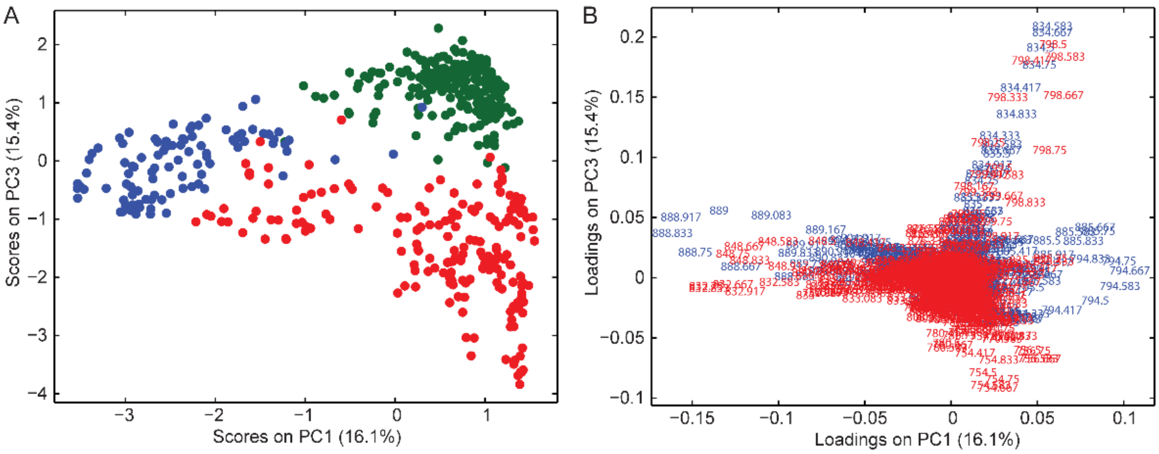

Figure 5-5. (A) Midlevel data fusion PCA score plot (*m/z* 700 – 1000) and (B) loading plots. Score plot symbols: Grey matter, n=223 (green); white matter, n=98 (blue); and glioma (red), n=185. Loading plot values: negative mode (blue) and positive mode (red).

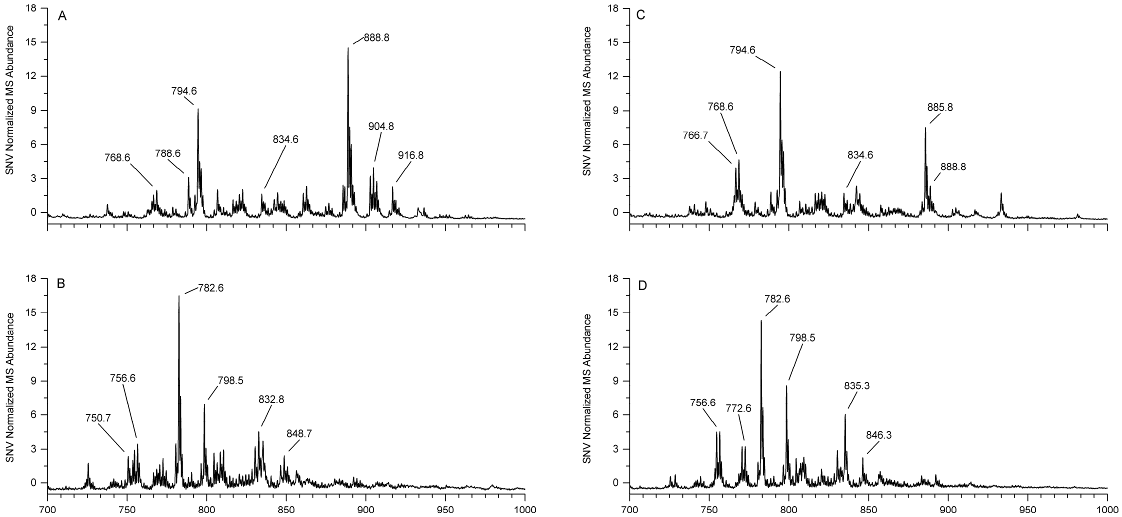

Figure 5-6. (A) Negative and (B) positive mode average of the white matter associated glioma subgroup. (C) Negative mode average of the grey matter associated glioma subgroup. (D) Positive mode average of the grey matter associated glioma subgroup. Major ions are annotated.

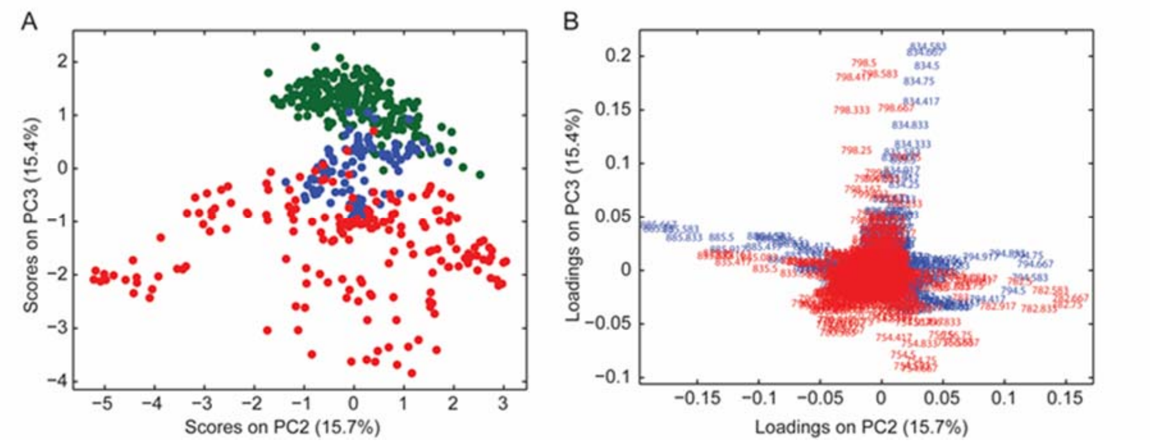

Figure 5-7. (A) Mid-level data fusion PCA score plot (*m/z* 700 – 1000), PC2 vs PC3, and (B) loading plots. Score plot symbols: Grey matter, n=223 (green); white matter, n=98 (blue); and glioma (red), n=185. Loading plot values: negative-mode (blue) and positive-mode (red).

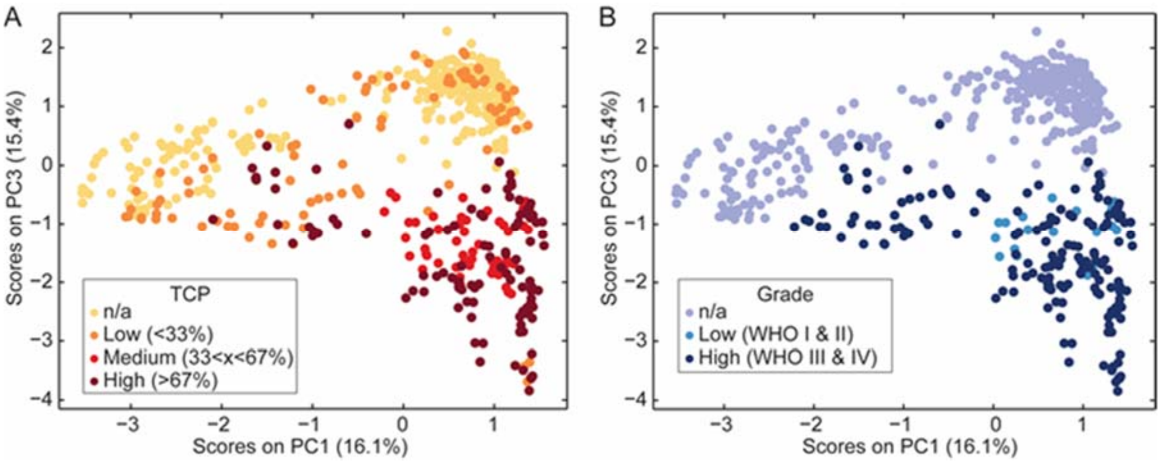

Figure 5-8. (A) PCA score plot (*m/z* 700 – 1000), PC1 vs PC3, for tumor cell percentage (TCP): n/a (yellow), normal grey or white matter; low (orange), <33%; medium (red), 33%<x<67%; high (dark red), >67%. (B) PCA score plot for glioma grade: n/a (blue heather), normal grey or white matter; low grade (light blue), glioma WHO grade I or II; high grade (dark blue), glioma WHO grade III or IV.

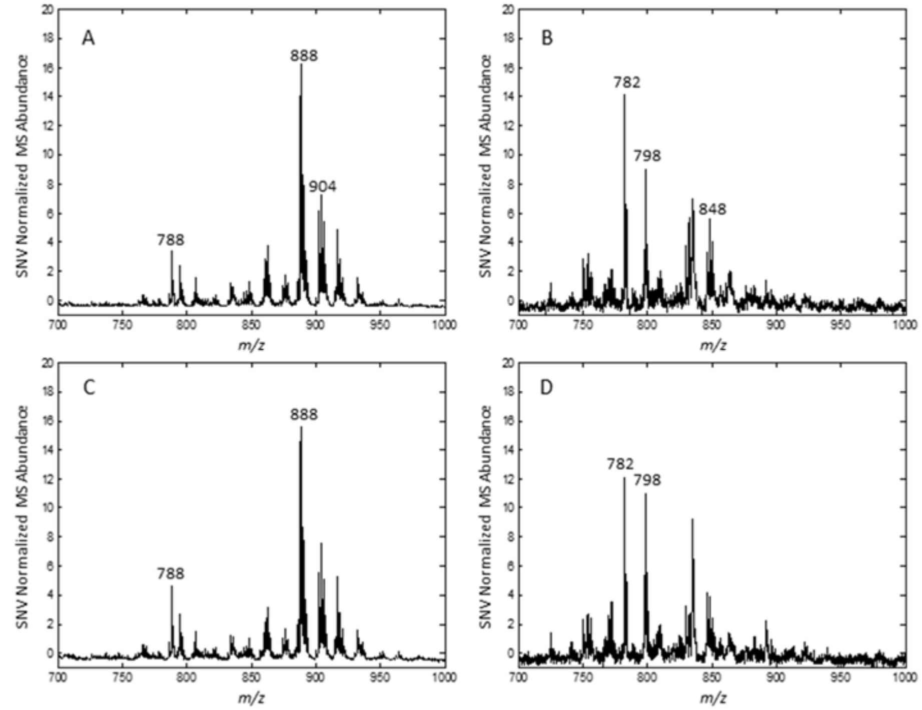

Figure 5-9. (A) Negative and (B) positive ion mode lipid profiles (*m/z* 700 – 1000) of ROI #1 with 40% TCP. (C) Negative and (D) positive ion mode lipid profiles of ROI #5 with 60% TCP. Note, that the 40% TCP spectra look more reminiscent of normal white matter while the 60% TCP spectra appear more like the white matter associate glioma subgroup, e.g. altered ratio between *m/z* 794 ([PC 34:1 + Cl]$^-$) and *m/z* 888 ((3'-sulfo)GalCer 24:1)) in the negative ion mode and altered ratio of *m/z* 798 ([PC 34:1 + K]$^+$ or [PE P-40:6 + Na]$^+$) and *m/z* 848 ([GalCer d32:2 + K]$^+$) in the positive mode.

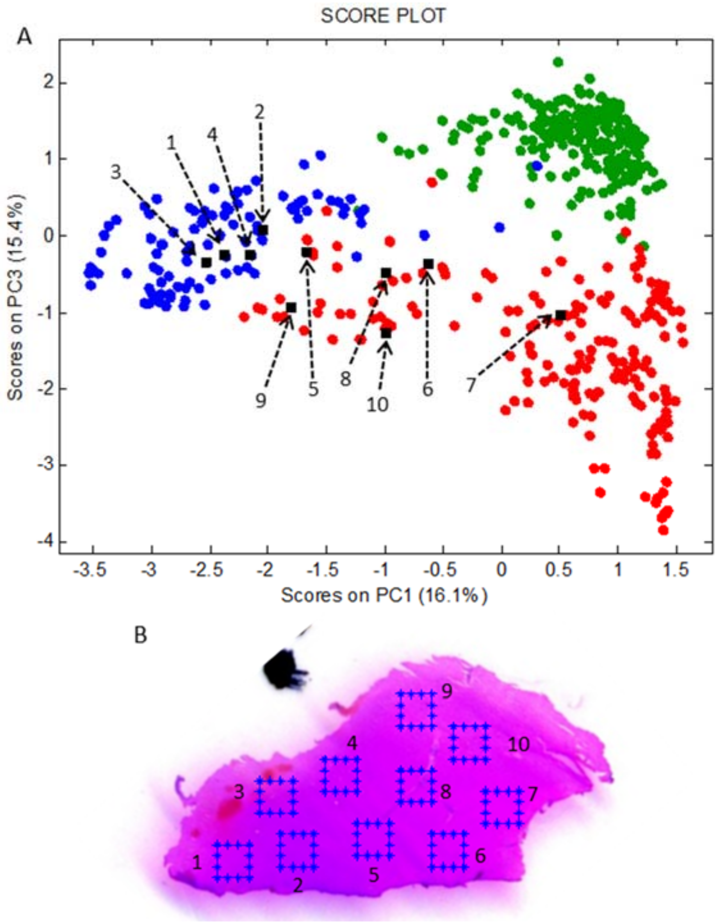

Figure 5-10. (A) Mid-level data fusion PCA score plot (*m/z* 700 – 1000), PC1 vs PC3, with ROI of 3003KDE projected (black squares). The points annotated correspond to specific ROIs indicated on the H&E stained tissue in (B). Score plot symbols: Grey matter, n=223 (green); white matter, n=98 (blue); and glioma (red), n=185.

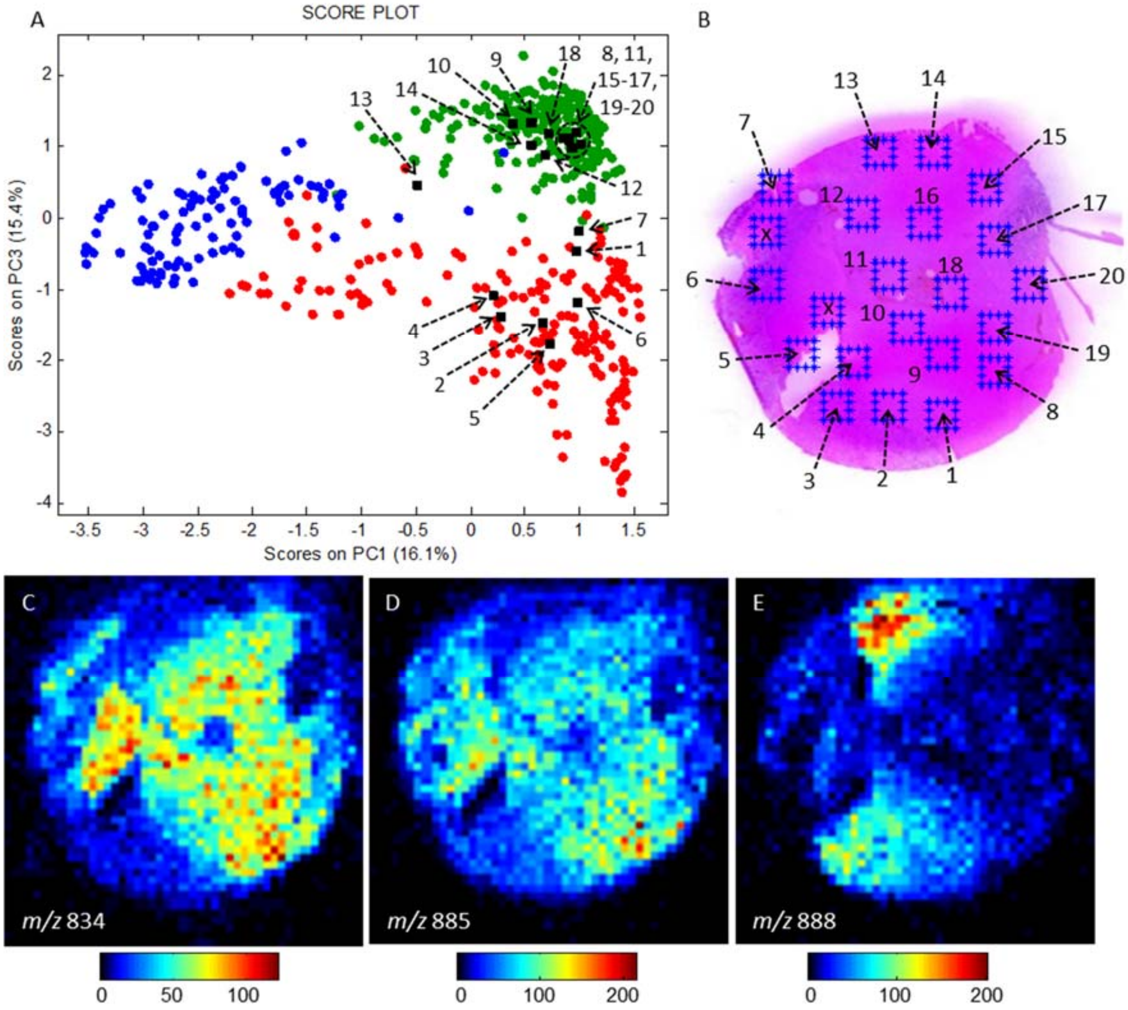

Figure 5-11. (A) Mid-level data fusion PCA score plot (*m/z* 700 – 1000), PC1 vs PC3, with ROI of 3003ETP projected (black squares). Score plot symbols: Grey matter, n=223 (green); white matter, n=98 (blue); and glioma (red), n=185. (B) ROI are annotated upon the H&E stained tissue section. (C-E) Selected negative ion mode ion images of *m/z* 834 (PS 40:6), 885 (PI 38:4), and 888 ((3’-sulfo)GalCer 24:1), respectively, plotted in false-color with corresponding scale bar (absolute MS abundance). Note, the regions of predominately normal grey (*m/z* 834) and white (*m/z* 888) contain approximately 10% tumor cells.

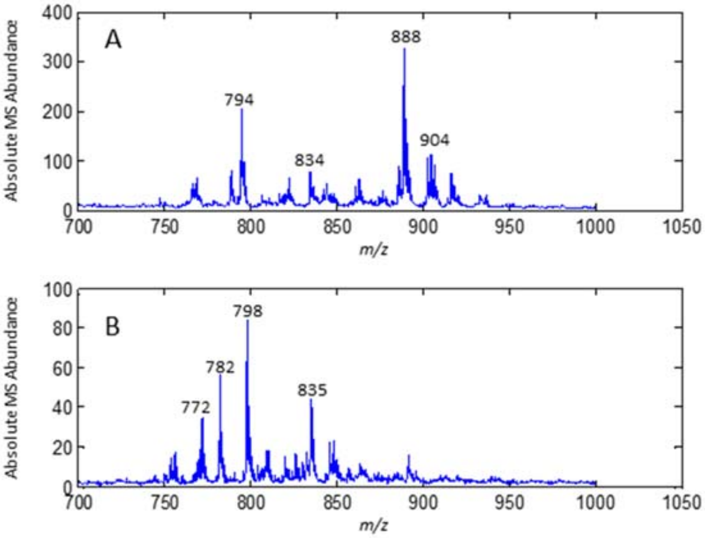

Figure 5-12. (A) Negative and (B) positive ion mode lipid profile (*m/z* 700 – 1000) from a specimen 30003UVH that was effaced, morphologically. The spectra appear similar to that of white matter (via *m/z* 888 detection) and suggest the background parenchyma is white matter.

Table 5-1. HRMS and MS/MS data for selected ions detected in positive mode DESI-MSI of brain tissue and glioma specimens.

Tentative Ion Identification	Theoretical Mass (Monoisotopic)	Measured Mass	Mass Error (ppm)	Major MS^2 Fragment Ions	MS^3 Fragment Ions
[PE(P-36:2)+Na]$^+$	750.5408	750.5407	-0.1865	707 (-43)	707->609, 587, 441
[GalCer(d36:1)+Na]$^+$	750.5854	750.5855	0.1332	732 (-18), 588 (-162), 570 (-180)	588->570
[PC(32:1)+Na]$^+$	754.5357	754.5362	0.6627	695 (-59), 571 (-183)	695->571, 549
[PC(32:0)+Na]$^+$	756.5514	756.5530	2.1149	697 (-59), 573 (-183)	697->573, 551
[PC(32:0)+K]$^+$	772.5253	772.5281	3.6245	713 (-59)	713->589, 551
[PE(P-38:5)+Na]$^+$	772.5252	772.5281	3.7125	729 (-43)	729->631, 489
[PC(34:1)+Na]$^+$	782.5670	782.5679	1.1705	723 (-59)	723->599, 577
[PC(34:1)+K]$^+$	798.5410	798.5415	0.6224	739 (-59), 615 (-183)	739->615, 577
[PE(P-40:6)+Na]$^+$	798.5408	798.5415	0.8728	755 (-43)	755->657, 487
[PC(36:2)+Na]$^+$	808.5827	808.5851	3.0226	749 (-59), 625 (-183)	749->625, 603
[GalCer(d32:2)+Na]$^+$	832.6636	832.6642	0.6701	814 (-18), 670 (-162), 652 (-180)	670->652
[GalCer(d32:2)+K]$^+$	848.6376	848.6390	-1.5979	686 (-162), 668 (-180)	686->668

Table 5-2. Positive ion mode PCA-LDA confusion matrix (six principal components, five deletion groups) for grey matter, white matter, and glioma with calculated sensitivity and specificity for each class.

		Histopathology		
		Grey matter	White matter	Glioma
DESI	Grey matter	216	9	13
	White matter	1	88	0
	Glioma	6	1	172
	Sensitivity (%)	96.9	89.8	93.0
	Specificity (%)	92.2	99.7	97.7

Table 5-3. Negative ion mode PCA-LDA confusion matrix (six principal components, five deletion groups) for grey matter, white matter, and glioma with calculated sensitivity and specificity for each class.

		Histopathology		
		Grey matter	White matter	Glioma
DESI	Grey matter	219	2	1
	White matter	4	94	21
	Glioma	0	2	163
	Sensitivity (%)	98.2	95.9	88.1
	Specificity (%)	98.8	93.9	99.4

Table 5-4. Data fusion PCA-LDA confusion matrix with calculated sensitivity and specificity for grey matter, white matter, and glioma. The average sensitivity, 94.7%, and specificity, 97.6%, is the mean of the values for the individual classes.

		Histopathology		
		Grey matter	White matter	Glioma
DESI	Grey matter	216	2	1
	White matter	5	94	15
	Glioma	2	2	169
	Sensitivity (%)	96.9	95.9	91.4
	Specificity (%)	98.9	95.1	98.7

CHAPTER 6. INTRASURGICAL ANALYSIS OF HUMAN GLIOMAS BY DESORPTION ELECTROSPRAY IONIZATION – MASS SPECTROMETRY

6.1 Introduction

A primary treatment for brain cancer is surgery, where the goal is to maximize the extent of tumor resection while minimizing neurological damage. (1) Reliable intrasurgical tools, i.e. within the operating room, for near real time tissue diagnosis are lacking. Mass spectrometry might provide rapid intrasurgical determination of disease state, i.e. normal versus tumor, at discrete points near the surgical margin. (2) Frozen section histopathology remains the gold standard for obtaining intrasurgical information such as type of tumor (e.g. glioma) and grade (e.g. low grade). This information is currently obtained outside of the operating room taking upwards of 20 minutes per sample which includes sectioning, staining, and expert interpretation. Tissue smears, in addition to tissue sections, are used currently to obtain pathologic information from surgical biopsies during tumor resection. Smears are used when rapid pathologic feedback is beneficial during surgical resection of tumors. However, pathologic evaluation of tissue smears is inherently less accurate than frozen tissue sections due to some loss of morphological information. (3) Ambient ionization - mass spectrometry (MS) allows rapid acquisition of molecular information from tissue. The application of ambient ionization– MS in surgery is divided between offline and online approaches. (2) The offline approach follows current protocols, e.g. biopsy, but inserts MS measurement in the sequence prior to histopathology Ideally, analysis is transparent to morphology/cytology allowing for subsequent analysis by pathology – improving correlation via supporting pathology. One alternative online approach, the iKnife or intelligent scalpel, rapidly acquires MS data in vivo but is destructive so cannot be corroborated by pathology. (4) Regardless of the MS method, the chemical information provided is crucial in decision-making and both procedures have potential surgical applications.

Human brain tumors have been studied using desorption electrospray ionization (DESI) – MS imaging since 2010. (5-8) More recently, the ability to differentiate normal brain matter from tumors (glioma, meningioma, and pituitary tumor) was demonstrated using frozen tissue sections and tissue smears. (9) DESI-MS analysis of tissue smears is a substantial departure from DESI-MS imaging which requires tissue freezing and sectioning prior to analysis. The lipid and metabolite MS profiles acquired from tissue smears are highly similar to those acquired from tissue sections. (9) A DESI-MS method and intrasurgical MS system, one that is used within the operating room, has been developed that rapidly analyzes (<3 minutes per sample) tissue smears. DESI-MS predicted disease state, i.e. normal or tumor, was compared to pathologic evaluation performed on the same sample analyzed. Additionally, tumor cell percentage (TCP), i.e. relative amount of tumor cells compared to normal cells, was predicted via DESI-MS measurement of N-acetyl-aspartic acid (NAA) and compared with pathology. The preliminary data from the first four cases are discussed.

6.2 Experimental

6.2.1 Human Subjects

Subjects were enrolled in an IRB approved study (IU #1410342262) in which biopsied tissue, removed following standard protocols, was analyzed intrasurgically at Indiana University Health Methodist Hospital in Indianapolis, IN. Tissue biopsies were provided by the surgeon, Dr. Aaron A. Cohen-Gadol; the location (stereotactic position) and location relative to the tumor resection was annotated, e.g. frontal margin. Magnetic resonance imaging data was collected in accordance with regulations and following HIPPA authorization.

6.2.2 Methods

6.2.2.1 Intrasurgical DESI Mass Spectrometer

We assembled and modified a commercial linear ion trap mass spectrometer (LTQ, Thermo) such that the following features, not available in commercial instruments, have be added for use in the operating room: encasement of the entire system (MS, vacuum pumps, computer, etc.) using a stainless steel surface that can be sanitized, additional vacuum pump noise reduction, integrated computer system with sealed keyboard, and enclosed custom DESI ion source, including custom moving stage, small nitrogen and helium gas tanks with regulators, and power converter (240 to 120V). Further, the custom

DESI source is encased by an electrostatic dissipative housing that reduces solvent vapor release and functions as a high voltage safety barrier.

6.2.2.2 Tissue Smearing and DESI-MS Analysis

Biopsied tissue was smeared on a glass microscope slide using a 3D printed device, illustrated in Figure 6-1, detailed in Jarmusch et al. (9) The smeared tissue was then immediately analyzed by DESI-MS. DESI-MS was performed using equal parts dimethylformamide-acetonitrile (v/v) which preserved tissue morphology for subsequent pathology. (10) Additional source parameters are as follows: AGC activated, solvent flow rate, 1.0 µL min^{-1}; pressure of nitrogen gas, 160 PSI; ±5.0 kV (depending on ionization mode); incident angle, 52°; spray-to-surface distance, 2 - 3 mm; spray-to-inlet distance, 5 - 7 mm. Each tissue smear was analyzed by DESI-MS collecting five different types of mass spectra, i.e. negative mode lipid profile, negative mode metabolite profile, MS/MS of N-acetyl-aspartic acid, MS/MS of 2-hydroxyglutaric acid, and positive mode lipid profile. Each MS scan type was performed by moving the DESI-MS spray spot in a series of three lines across the narrowest dimension of the microscope slide, stepping 12.5 mm (along the longest dimension) between lines – this process was repeated for the next MS scan type offsetting the original spot by 250 microns.

6.2.2.3 Pathology

Tissue smears analyzed by DESI-MS were stained after analysis using hematoxylin and eosin (H&E). Blind histopathologic evaluation of tissue smears was performed by Dr. Eyas M. Hattab and the following information was provided when possible: disease state (normal grey matter, normal white matter, glioma, or other), tumor cell percentage (estimated percentage), and any additional comments.

6.2.2.4 Data Handling and Multivariate Statistics

DESI-MS spectra were acquired using XCalibur 2.0 (.raw) and converted into .mzXML files, and then imported into MATLAB (MathWorks, Inc., Natick, MA, USA). In-house MATLAB routines were used to process all MS data. Prediction of disease state was performed using a PCA-LDA model built using DESI-MS data obtained from frozen tissue sections, discussed in Jarmusch et al. (9) Tumor cell percentage was predicted via NAA abundance. (9) MRI stereotactic data were recorded anonymously using an intraoperative guidance system (StealthStation, Medtronic).

6.3 Results and Discussion

A DESI-MS method for the analysis of tissue smears has been implemented at Indiana University Health Methodist Hospital in Indianapolis, Indiana for the intrasurgical analysis of human glioma. Tissue biopsies were taken from subjects undergoing tumor resection, following standard protocols, and were analyzed intrasurgically using a custom MS system. The biopsy tissue was analyzed by DESI-MS immediately following smearing.

The following types of MS scans were collected from each smear: negative mode lipid profile, negative mode metabolite profile, MS/MS of N-acetyl-aspartic acid, MS/MS of 2-hydroxyglutaric acid, and positive mode lipid profile (data are neither shown nor discussed for the latter three MS scan types). The total data acquisition time was ~2.75 minutes per smear. Tissue smears were stained after analysis and blindly evaluated by pathology.

DESI-MS negative mode lipid and metabolite profiles were used to predict the disease state (i.e. grey matter, white matter, or glioma) and tumor cell percentage (TCP) of each biopsy. The preliminary results from the intrasurgical study have been very encouraging, provided only that enough tissue was present on the slide. The spectra are of high quality and highly reminiscent of data obtained in vitro upon frozen tissue sections and tissue smears. Smears of poor cellularity yielded poor DESI-MS spectra and are equally uninformative pathologically – in practice such smears would not be used to render a diagnosis. DESI-MS prediction of disease state was corroborated by pathology with a few exceptions. Over 4 cases and 25 unique biopsies have been analyzed. Blind pathologic evaluation determined that 21/25 biopsies were glioma with the remaining number being infiltrative margin (4/25). DESI predicted that 19/25 were glioma and the remaining 6 as either grey or white matter – DESI prediction of disease state matched pathology 92% of the time. The majority of the glioma smears contained >67% tumor cells while the infiltrative margin smears frequently contained <33%. DESI-MS correctly predicted grey matter and white matter in the pathologically-defined infiltrative margin smears (1 each), grey or white matter was not specified by the pathologist in two infiltrative margin samples, Table 6-1. Two smeared biopsies from the same case were predicted as white matter by DESI (35% TCP) which differed from pathology. Pathology determined that these particular smears were gliomas, containing an estimated TCP of 50%. While the categorical call of disease state differed, the tumor cell percentages were similar (within 15%). The pathologic call and DESI-MS prediction of these smears should be regarded as being similar rather than incorrect; the difference is a question of definition.

Case 6 is illustrative of the intrasurgical data being collected. Biopsies #2-4 and #7 were projected onto the PCA score plot, annotated black points (Figure 6-2). The location of each biopsy was recorded stereotactically during surgery, displayed in Figure 6-3. Biopsy #2 was from the frontal margin but contained a large percentage of tumor cells (histopathology 90%, DESI-MS predicted 93%); in this instance, the TCP remained relatively high while approaching the surgical margin. In contrast, biopsies #3 (pathology 15% - DESI-MS 11%) and #7 (pathology 15% - DESI-MS 30%) contained relatively few tumor cells, and were correctly predicted by DESI-MS as grey and white matter, respectively. The location of the projected biopsy #3 and #7 in the PCA score plot visually indicated the matter into which the glioma was infiltrating. Note, the projected location of the biopsies are relatively close to the glioma class (red) which likely reflects some small fraction of tumor cells. Biopsy #4 is representative of the majority of the tumor volume – pathologically diagnosed as high-grade glioma with 70% TCP and DESI-MS predicted glioma with 76% TCP (prediction of grade by DESI is the objective of a future study). The average difference (absolute) between pathologic evaluation and DESI-MS prediction of

TCP was 12.5% for all biopsies in case 6, and was 17.9% in all of the 25 unique biopsies analyzed in four cases, Table 6-1. The importance of understanding TCP in combination with the pathologic diagnosis is evident as TCP appears to be heterogeneous within the tumor volume.

6.4 Conclusions

The preliminary data obtained from four initial cases indicates DESI-MS can differentiate disease states and predict tumor cell percentage intrasurgically. The creation of high quality tissue smears and their analysis was a critical development that makes DESI-MS analysis feasible in less than three minutes. In the initial cases, DESI-MS analysis of all biopsies from a particular case was completed before the traditional histopathologic protocols provided information to the surgeon. The biopsies from Case 6 illustrated the heterogeneity of gliomas and how the developed method could be used to detect residual tumor cells in the infiltrative margin biopsies. The current MS system is capable of near real-time feedback, requiring only statistics to be performed on the same computer – we intend to perform such data analysis when it becomes responsible and permitted by IRB approval.

6.5 Acknowledgements

The implementation of this method was no small feat. The contributions of the Purdue team Professor R. Graham Cooks, Dr. Valentina Pirro, Dr. Zane Baird, and Clint M. Alfaro have helped transfer this technology from the laboratory into the operating room.

The excitement, willingness, and contribution of our surgeon collaborator, Dr. Aaron A. Cohen-Gadol, is immeasurable – it is surgeons such as Dr. Cohen-Gadol who are necessary for developing these new tools. Kudos to the surgical team, particularly Suzann Moore, and the clinical research nurses for their assistance in the study. I would be remiss to not mention the contributions of Dr. Eyas M. Hattab, neuropathologist, in providing expert pathologic evaluation of the specimens and his expert insight.

6.6 References

1. Lacroix M, Abi-Said D, Fourney DR, Gokaslan ZL, Shi W, DeMonte F, et al. A multivariate analysis of 416 patients with glioblastoma multiforme: prognosis, extent of resection, and survival. Journal of neurosurgery. 2001;95(2):190-8.

2. Ifa DR, Eberlin LS. Ambient Ionization Mass Spectrometry for Cancer Diagnosis and Surgical Margin Evaluation. Clinical chemistry. 2016;62(1):111-23.

3. Tilgner J, Herr M, Ostertag C, Volk B. Validation of intraoperative diagnoses using smear preparations from stereotactic brain biopsies: intraoperative versus final diagnosis—influence of clinical factors. Neurosurgery. 2005;56(2):257-65.

4. Balog J, Sasi-Szabo L, Kinross J, Lewis MR, Muirhead LJ, Veselkov K, et al. Intraoperative tissue identification using rapid evaporative ionization mass spectrometry. Sci Transl Med. 2013 Jul 17;5(194):194ra93. PubMed PMID: 23863833. English.

5. Eberlin LS, Dill AL, Golby AJ, Ligon KL, Wiseman JM, Cooks RG, et al. Discrimination of human astrocytoma subtypes by lipid analysis using desorption electrospray ionization imaging mass spectrometry. Angewandte Chemie. 2010;122(34):6089-92.

6. Eberlin LS, Norton I, Dill AL, Golby AJ, Ligon KL, Santagata S, et al. Classifying human brain tumors by lipid imaging with mass spectrometry. Cancer research. 2012;72(3):645-54.

7. Eberlin LS, Norton I, Orringer D, Dunn IF, Liu X, Ide JL, et al. Ambient mass spectrometry for the intraoperative molecular diagnosis of human brain tumors. Proceedings of the National Academy of Sciences. 2013;110(5):1611-6.

8. Santagata S, Eberlin LS, Norton I, Calligaris D, Feldman DR, Ide JL, et al. Intraoperative mass spectrometry mapping of an onco-metabolite to guide brain tumor surgery. Proceedings of the National Academy of Sciences. 2014;111(30):11121-6.

9. Jarmusch AK, Pirro V, Baird Z, Hattab EM, Cohen-Gadol AA, Cooks RG. Lipid and metabolite profiles of human brain tumors by desorption electrospray ionization-MS. Proceedings of the National Academy of Sciences. 2016:201523306.

10. Eberlin LS, Ferreira CR, Dill AL, Ifa DR, Cheng L, Cooks RG. Nondestructive, histologically compatible tissue imaging by desorption electrospray ionization mass spectrometry. ChemBioChem. 2011;12(14):2129-32.

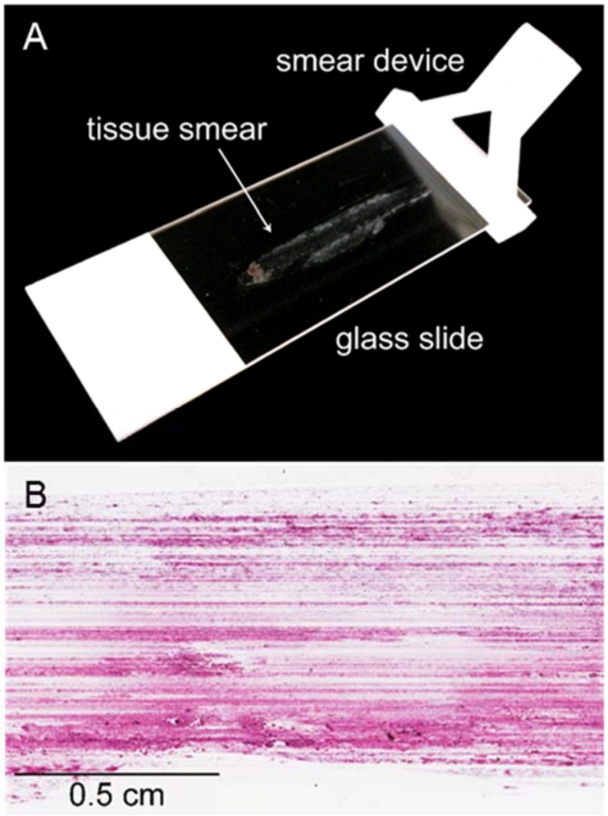

Figure 6-1. (A) Photograph of 3D printed smear device being used to smear tissue. (B) Illustrative tissue smear after DESI-MS analysis and H&E staining.

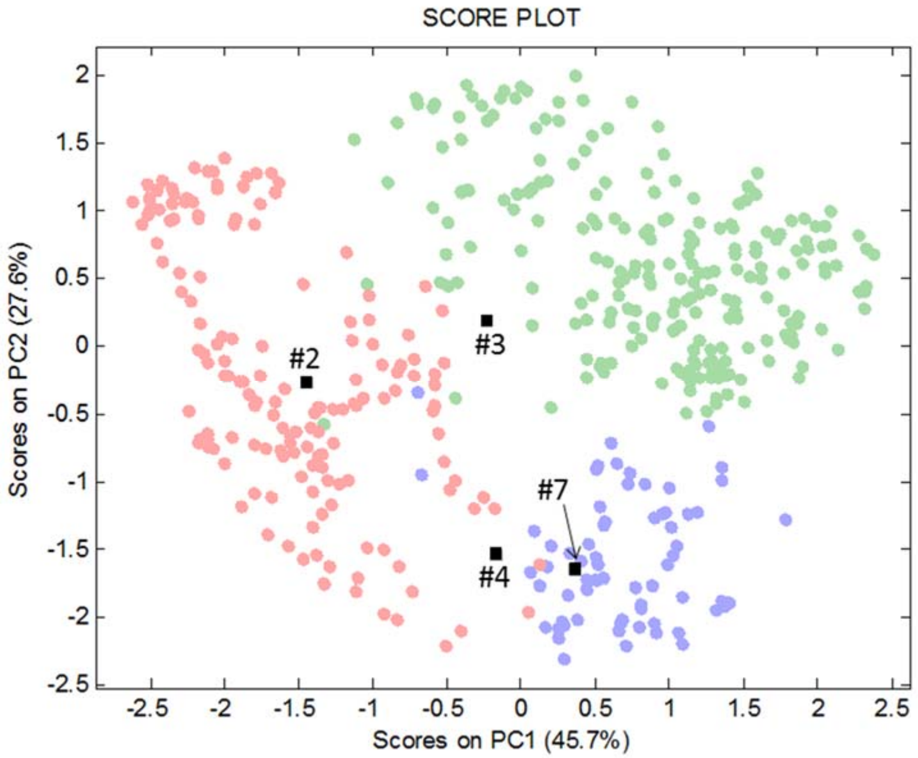

Figure 6-2. Projection of Case 6 biopsies #2-4 and #7 (black squares) onto the negative ion mode metabolite and lipid data fusion PCA score plot. Grey matter (green), white matter (blue), and glioma (red).

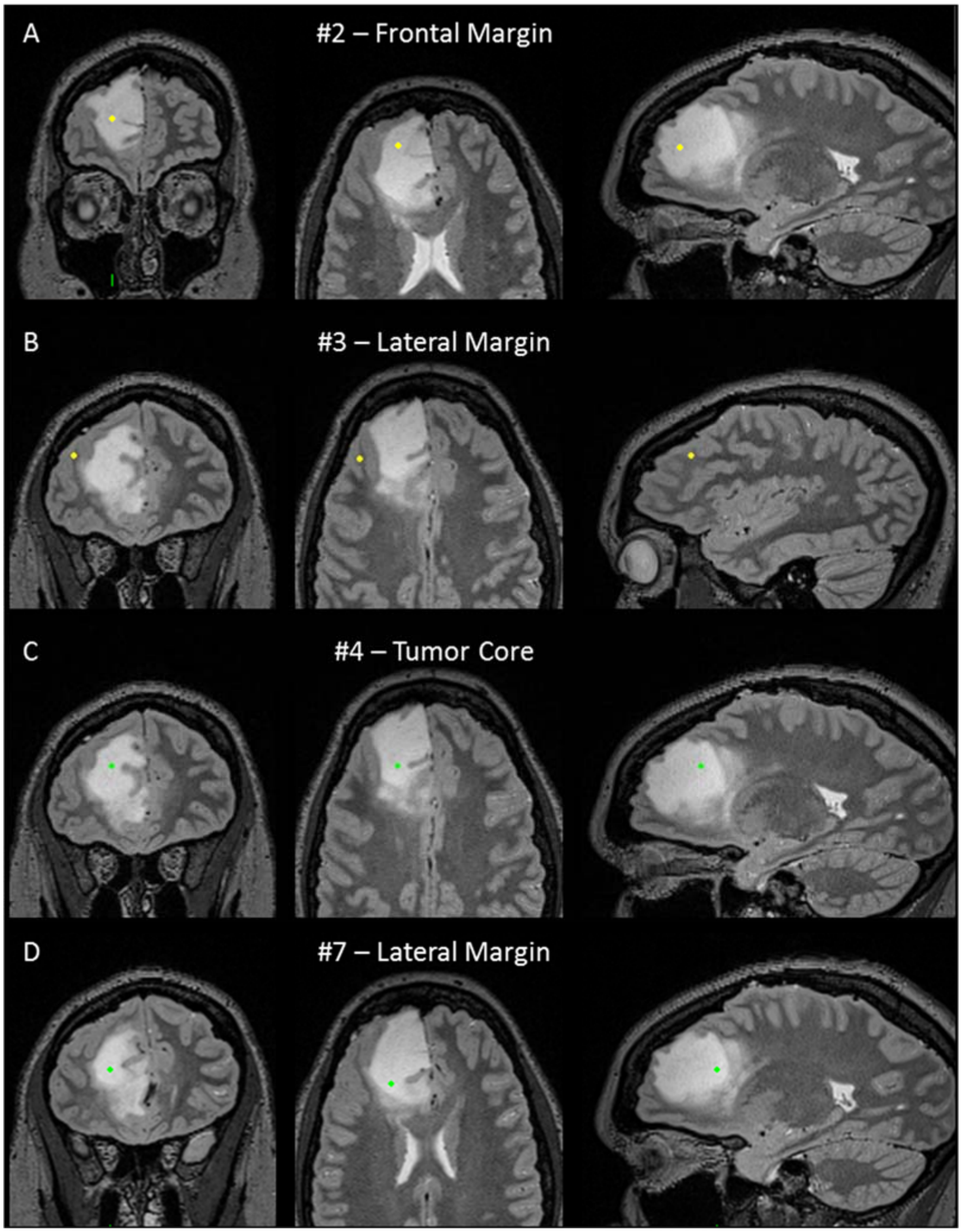

Figure 6-3. T2-weighted magnetic resonance images with stereotactic location, colored point, of Case 6 biopsies (A) #2, (B) #3, (C) #4, and (D) #7. The location (provided by surgeon), relative to tumor mass, is annotated. The bright region corresponds to the location of the high-grade glioma.

Table 6-1. Tabulated Pathologic Information and DESI-MS Predictions from Intrasurgical Cases 4 – 7. Replicate smears made from the same tissue biopsy have been excluded from the table.

	Pathology		DESI-MS Prediction		Absolute Difference in TCP (%)
Sample ID	Diagnosis	TCP (%)	Diagnosis	TCP (%)	
CASE4_1	Glioma	50	Glioma	100	50
CASE4_2	Glioma	20	Glioma	58	38
CASE4_3	Glioma	70	Glioma	56	14
CASE4_4	Glioma	50	Glioma	100	50
CASE4_5	Glioma	90	Glioma	100	10
CASE4_7	Glioma	90	Glioma	100	10
CASE4_9	Glioma	30	Glioma	95	65
CASE5_1	Glioma	90	Glioma	100	10
CASE5_3	Glioma	60	Glioma	63	3
CASE5_4	Glioma	80	Glioma	90	10
CASE5_5	Glioma	50	Glioma	80	30
CASE5_6	Glioma	60	Glioma	62	2
CASE5_7	Glioma	80	Glioma	73	7
CASE5_8	Glioma	80	Glioma	91	11
CASE6_1	Glioma	50	Glioma	76	26
CASE6_2	Glioma	90	Glioma	93	3
CASE6_3	Inf. Margin (Grey Matter)	15	Grey Matter	11	4
CASE6_4	Glioma	70	Glioma	76	6
CASE6_5	Glioma	50	Glioma	71	21
CASE6_7	Inf. Margin (matter not specified)	15	White Matter	30	15
CASE7_1	Glioma	90	Glioma	70	20
CASE7_2	Inf. Matter (matter not specified)	10	Grey Matter	0	10
CASE7_3	Glioma	50	White Matter	35	15
CASE7_4	Glioma	50	White Matter	35	15
CASE7_5	Inf. Margin (White matter)	10	White Matter	12	2

CHAPTER 7. PERSPECTIVE

New tools in diagnostic medicine are crucial for improving pathology and surgery. Pathology requires detailed information for use in diagnosis which is currently obtained via histopathologic evaluation of tissue biopsies and genetic testing; however, this process is fairly lengthy and ultimately renders a subjective decision. Surgery seeks to answer simple diagnostic questions (e.g. “is this cancerous or not”) but contends with much more difficult practical questions, such as “what is the relative good, compared to harm, in surgically removing tissue.” There exists few tools aside from magnetic resonance imaging that can assist surgeons during surgical removal of tumors. Analytical measurements provide objective information that can assist pathology via chemical-based diagnosis and surgery through rapid tissue assessment, intrasurgically. Notable analytical methods currently being developed include Raman spectroscopy, infrared spectroscopy, and fluorescence. Ambient ionization – mass spectrometry (MS) also has great potential to fulfill unmet needs in pathology and surgery. Reduced analysis time, primarily due to relaxed sample preparation requirements, using ambient ionization coupled with the molecular specificity and sensitivity of MS is a potentially powerful capable combination. Further, many of the MS manufactures have or are currently developing MS products that meet the criteria for Federal Drug Administration medical device approval which likely foreshadows widespread adoption of MS technology in medicine.

A large body of scientific work supports the potential of using ambient ionization – MS for cancer diagnosis. Numerous human cancers have been studied using ambient ionization – MS and in all cases the pattern of lipids detected in the MS profile can be used to differentiate normal from cancerous tissue. It is interesting that the lipid profiles of each organ and the corresponding cancer of that organ also differ from one another. The lack of similarity in the lipid profiles of different organs is not surprising as each has a unique anatomy and physiology, viz. liver is very different from brain in both form and function; however, the dissimilarity of lipid profiles between cancers was not necessarily expected. Cancer biology suggest that cancer originates from a series of mutations – some mutations are more frequent, e.g. KRAS, PTEN, AKT, mTOR, NF-κB, etc. Therefore, one might expect the downstream metabolism, including lipid metabolism, to be show overall similarities in cancer. This is not the observation of the ambient ionization – MS studies, but there are some commonalities such as the overall increase in phosphatidylcholines, altered cholesterol metabolism and storage (e.g. cholesterol esters), and altered phosphatidylinositols.

More recently, additional metabolite information is being sought to assist in differentiating normal from cancerous tissue. N-acetyl-aspartic acid, a small molecule metabolite (less than *m/z* 200), has proven to be extremely important in differentiating human gliomas from normal brain parenchyma. 2-hydroxyglutaric acid, a downstream metabolite of IDH mutation in gliomas, is important for prognosis. The utility of small molecules metabolites detected by ambient ionization – MS for cancer detection will likely be explored in future studies.

We sought to acquire differentiating molecular information rapidly within the operating room. Two methods, touch spray and DESI, were developed for this purpose. The molecular differences between normal and cancerous tissue were detected via direct tissue analysis in vitro by touch spray ionization (TS) or by analyzing sectioned or smeared tissue using desorption electrospray ionization (DESI). The physical form of the tissue, e.g. in vitro sampling, sectioned, or smeared, was inconsequential in differentiating normal from cancerous tissue; however, the spectra acquired by TS and DESI differed due to differences in ionization processes. Touch spray is intended for in vivo sampling within surgery to assist in determine the disease state of discrete areas that a surgeon finds suspicious. The TS methodology aligns closely with standard online intrasurgical methods, in vivo sampling and rapid analysis (seconds). The use of tissue smears for intraoperative analysis falls under the offline intrasurgical analysis, and does not require major modification to current practice. We imagine that intrasurgical MS analysis of smeared biopsy tissue can offer the surgeon reliable pathologic information on a timescale ten times faster than current pathology, which can also be corroborated via standard pathologic evaluation. TS and DESI have potential for impacting surgical treatment of tumors. The culmination of my research is the development and implementation of an intrasurgical DESI-MS analysis method and multivariate classification system for human brain tumors. Preliminary results from the intrasurgical study are very promising and have thus far proven to correlate well with pathology. We expect that similar results will be obtained over the planned 50 subjects to be enrolled in that study. The implementation of this technology in additional hospitals around the world is expected. Positivity impacting the lives of cancer patients via better molecular-based tissue diagnosis using ambient ionization –MS is very close to becoming a reality.

VITA

VITA

Alan Keith Jarmusch was born in Youngstown, Ohio in 1988, son of Albert Keith and Linda Fay Jarmusch. He grew up in Canfield, Ohio and graduated from Canfield High School in 2007 with honors. Alan attended the University of North Carolina at Greensboro in Greensboro, North Carolina where he majored in Biochemistry. Nadja B. Cech served as his academic and undergraduate research mentor. In her lab, Alan studied the alkaloid constituents of *Echinacea purpurea and Achnatherum* robustum by mass spectrometry. The study of natural products using mass spectrometry introduced Alan to analytical chemistry and influenced his decision to pursue graduate studies. He was awarded the American Chemical Society's Undergraduate Analytical Chemistry Award in 2010 and won the 2nd prize for Outstanding Undergraduate Research Project (2011). Alan graduated in 2011, *cum laude*, receiving a Bachelor of Science degree in biochemistry, and was recognized with the award for Best Graduate in Class (chemistry or biochemistry). Graduate study planted him back in the Midwest at Purdue University, mentored by Henry B. Hass Distinguished Professor R. Graham Cooks. While at Purdue, Alan was nominated for Graduate Teaching Assistant of the Year, received numerous travel grants and poster prizes, and was recognized as the Alice Watson Kramer Research Scholar in

2016. Alan plans to begin postdoctoral research at the University of California, San Diego mentored by Professor Pieter C. Dorrestein.

PUBLICATIONS

Analyst

PAPER

Cite this: *Analyst*, 2015, **140**, 6321

Characteristic lipid profiles of canine non-Hodgkin's lymphoma from surgical biopsy tissue sections and fine needle aspirate smears by desorption electrospray ionization – mass spectrometry†

Alan K. Jarmusch,‡[a] Kevin S. Kerian,‡[a] Valentina Pirro,[a] Tyler Peat,[b]
Craig A. Thompson,[b] José A. Ramos-Vara,[b] Michael O. Childress[c] and
R. Graham Cooks*[a]

Received 27th April 2015,
Accepted 27th July 2015

DOI: 10.1039/c5an00825e

www.rsc.org/analyst

Canine non-Hodgkin's lymphoma (NHL) is a heterogeneous group of cancers representing approximately 15% of all canine cancers. Further, canine NHL mimics human disease in regards to histopathology and clinical behavior and could function as a comparative model. Diagnosis is currently performed by histopathological evaluation of surgical biopsy specimens and fine needle aspirate (FNA) cytology, an alternative and less invasive method for diagnosis. Desorption electrospray ionization – mass spectrometry (DESI-MS) imaging was performed on tissue sections of surgical biopsies and FNA smears. Mass spectra acquired from normal lymph nodes and NHL tumors were explored using multivariate statistics (*e.g.* principal component analysis). Tissue sections yielded a predicted sensitivity of 100% for normal and 93.1% for tumor. Further, preliminary results suggest B-cell and T-cell lymphoma can be discriminated (CV sensitivity of 95.5% and 85.7%, respectively). Normal and B-cell NHL FNA samples analyzed by DESI produced spectra that were similar to spectra obtained from surgical biopsies. FNA samples were evaluated using a PCA-LDA classification system built using tissue section data, exploring if the chemical information obtained from the different sample types is similar and whether DESI-MS performed on FNA samples is of diagnostic value. FNA prediction rate for normal (85.7%) and B-cell NHL (89.3%) indicated that DESI-MS analysis of FNA, not previously explored, could provide rapid preliminary diagnosis. Certainly, MS provides complementary molecular information to be used in conjunction with histopathology/cytology, potentially improving diagnostic confidence. The methodology outlined here is applicable to canine NHL, further supports canine models of human NHL, and translation to humans is envisioned.

Introduction

Non-Hodgkin's lymphoma (NHL) is a diverse group of cancers, afflicting canines and humans. Rates of NHL in canines exceed that in humans;[1] nevertheless, NHL is the seventh most common human cancer in the United States resulting in an estimated 20 000 deaths in 2014.[2] NHL can be broadly defined into two subgroups, B-cell and T-cell, correlated to the lymphocyte immunophenotypes from which the cancer originated. B-cell lymphomas are the more common of the two, particularly diffuse large B-cell lymphoma, thus they are the primary focus of this study. Canine lymphoma is currently being considered as a meaningful comparative model for human NHL, while important in its own right.[1,3] The gold standard for diagnosis of NHL is histopathological evaluation of surgically removed lymph node (whole or in part), which is commonly supported by immunohistochemical (IHC) analysis. Histopathological diagnosis is based on morphological and cytological features, such as morphological growth pattern, nuclear size and shape, and mitotic index.[4,5] A less invasive alternative to surgical biopsy is fine needle aspirate (FNA) biopsy, performed using a hypodermic needle that is inserted

---

[a] *Department of Chemistry and Center for Analytical Instrumentation Development, Purdue University, 560 Oval Drive, West Lafayette, IN 47907, USA. E-mail: cooks@purdue.edu; Tel: +765-494-5263*

[b] *Department of Comparative Pathobiology, College of Veterinary Medicine, Purdue University, West Lafayette, IN 47907, USA*

[c] *Department of Veterinary Clinical Sciences, College of Veterinary Medicine, Purdue University, West Lafayette, IN 47907, USA*

† Electronic supplementary information (ESI) available. See DOI: 10.1039/c5an00825e

‡ Authors contributed equally to this work.

into a suspicious lymph node. A small amount of cellular material is removed, expelled onto a microscope slide, and smeared to form a cellular monolayer which may be evaluated using light microscopy following cytochemical or immunocytochemical staining. FNA smears are suitable for screening and rapid preliminary diagnosis; however, smaller sample size and destruction of nodal architecture, a result of smearing, can result in higher rates of false negatives and inconclusive diagnoses.[6] FNA does have advantages over surgical biopsy and histopathology, in that it is less expensive, less invasive, and less technically demanding.[7,8] Both canines and humans with NHL may be significantly debilitated at the time of initial cancer diagnosis, and a minimally invasive diagnostic technique may be better suited to these patients than surgical biopsy. Therefore, identifying methods to enhance the quality of diagnostic information afforded by FNA smears would be worthwhile.

A promising method for improving the diagnostic yield of FNA biopsies is desorption electrospray ionization – mass spectrometry (DESI-MS), an ambient ionization technique which allows for chemical analysis of surfaces, including tissue, at native atmospheric conditions (temperature, pressure, and humidity). The mechanism of analyte desorption and ion generation has been extensively studied.[9,10] Briefly, a stream of charged droplets impact the surface, create a thin film of solvent allowing analyte dissolution. Subsequent charged droplet impact sputters small analyte containing droplets which undergo evaporation and Coulombic fission generating ions *via* electrospray-like processes. DESI can be operated in an imaging mode, allowing chemical information to be mapped in two or more spatial dimensions.[11–16] DESI-MS imaging has been applied previously in canine bladder cancer[17] and human cancers, including those of the liver,[18] brain,[19] kidney,[20] prostate,[21] and other organs.[22] DESI-MS has been applied to human brain tissue smears obtained during surgery,[23] while differing from FNA smears in regards to collection and pathological evaluation. The analysis of lipids that compose cells, structurally and functionally, and tissue has been the focus of the previously mentioned studies, allowing for differentiation of cancer from normal tissue without exception. The lipid profile, *i.e.* type of lipid and quantity as reflected in the measured mass spectrum, varies with cell metabolism and signaling and is indicative of disease state. The use of multivariate statistics for pattern recognition, such as principal component analysis (PCA) followed by supervised classification techniques (*e.g.* linear discriminant analysis, LDA), allows for visualization and classification of differences between samples and complex relationships within large datasets.

In this paper we explore characteristic endogenous lipids using DESI-MS from surgical biopsy tissue sections and FNA smears for disease state differentiation (*i.e.* normal *vs.* tumor) in canine NHL. DESI-MS imaging of tissue sections detected lipid profiles indicative of disease state, which established a data set with which to compare FNA smears. Needle biopsies analyzed directly[24] or indirectly by ambient ionization – mass spectrometry have neither been demonstrated to be of diagnostic use nor shown to yield similar information to that of tissue section. The characteristic lipid profiles obtained from surgical biopsies and FNAs corroborate histopathology and cytology while providing unique chemical insight. Comparison between previous data regarding the significant lipids in human NHL and this canine study provide molecular support for a canine comparative model.

Methods

Specimens

Specimens were provided by the College of Veterinary Medicine, Purdue University. All NHL specimens were collected from pet dogs presented to the Purdue University Veterinary Teaching Hospital (PUVTH) for medical treatment of their cancer. At the time of presentation, fine needle aspirate samples were collected from an affected lymph node in each dog using a 22 gauge hypodermic needle. FNA samples were expelled onto glass slides, allowed to air dry, and then stored at −80 °C until the time of DESI-MS analysis. Immediately following FNA, all dogs with NHL underwent surgical biopsy of the same affected peripheral lymph node. A portion of each biopsy was fixed in 10% neutral buffered formalin and submitted for histopathologic confirmation of NHL. The residual portion of each dog's lymph node biopsy was snap frozen in liquid nitrogen, and the samples were stored at −80 °C until the time of DESI-MS analysis. Additional information pertaining to specimen 12, a metastatic carcinoma, can be found in the ESI.† Lymph node samples from healthy, purpose-bred research dogs served as normal controls. All control animals had been humanely euthanized as part of an academic laboratory course within the Purdue College of Veterinary Medicine Doctor of Veterinary Medicine degree curriculum. Surgical lymph node biopsy and FNA samples of peripheral lymph nodes were collected immediately post-mortem from all control animals in identical fashion to that described for pet dogs with NHL. All lymph nodes from control animals were confirmed to be histologically normal following light microscopic review of H&E stained sections from formalin-fixed tissues by a board-certified veterinary pathologist. All medical and surgical procedures conducted on both control animals and pet dogs were approved by the Purdue Animal Care and Use Committee (1111000308 and 1211000780).

DESI-MS analysis

Frozen surgical biopsy specimens were cryosectioned at 15 μm thickness using a Cryotome FSE (Thermo, Waltham, MA, USA) and thaw mounted on glass microscope slides (Gold Seal Rite-On Microscope Slides, Thermo). Prior to analysis, the slides were allowed to come to room temperature and briefly dried using an electronic desiccator (VWR, Desi-Vac Container, Radnor, PA, USA) for approximately 10 minutes to remove any frozen condensation resulting from storage. FNA smears were also dried for ∼10 minutes prior to analysis, for the same reason, and analyzed under the same conditions. Normal and tumor samples were randomized over multiple days of analysis, surgical biopsy tissue sections and specimen matched

FNA were analyzed on the same day. DESI-MS was performed using a lab built prototype ionization source coupled to a linear ion trap mass spectrometer (LTQ, Thermo). DESI-MS was carried out in the negative ion mode using equal parts dimethylformamide (DMF) and acetonitrile (ACN), preserving tissue morphology and allowing subsequent histopathology to be performed on the analyzed tissue section.[25] DESI analysis was performed using the following major parameters: automatic gain control (AGC) off, maximum ion injection time of 250 ms with 2 microscans, 5 kV spray voltage, 180 PSI N_2 (gas), incident spray angle was 52°, capillary temperature of 275 °C, spray-to-surface distance ~2 mm, and spray-to-MS inlet distance ~8 mm. Identical DESI-MS conditions were used to acquire high resolution mass spectrometry data on an orbitrap mass spectrometer (Exactive, Thermo). HRMS was interpreted using XCalibur and monoisotopic formulae masses were calculated in Isopro3. Sample slides were analyzed by securing them to the moving stage. The MS scan rate was coordinated with the moving stage speed in the "*x*" dimension (*i.e.* rows), defining resolution (200 μm). Upon the completion of each row, the moving stage was stepped vertically in 200 μm increments defining the "*y*" resolution. The typical time required for DESI imaging of a tissue section was less than 20 minutes. Illustrative is specimen 42, ~20 min, with an imaging area approximately 8.4 mm (width) by 7.6 mm (height), including the entirety of the tissue section roughly 6.2 mm (width) by 5.8 mm (height) in dimension.

Pathology

Histopathologic review, with tumor subtyping according to World Health Organization criteria,[4] was performed on formalin-fixed lymph node tissue sections as part of routine clinical diagnosis, see ESI Table 1.† The clinical diagnosis was used for DESI-MS data correlation. Samples demonstrating spatially heterogeneous chemical features were evaluated post DESI-MS analysis and annotated by histopathologic review of frozen tissue sections. There were no cases in which histopathology review differed between frozen and formalin-fixed tissue sections. The annotated regions were used to define areas associated with non-malignant morphological features, unless otherwise noted.

Cytology

Following DESI-MS analysis, all FNA slides were stained with Wright's stain and evaluated by light microscopy. FNA slides were reviewed by an expert veterinary cytopathologist, who interpreted the nature of the sample (*i.e.* lymphoma *vs.* non-lymphoma), the distribution of cells within the sample (*i.e.* homogenous *vs.* heterogeneous distribution of cellular material within the smear), the density of cells within the sample (*i.e.* densely cellular *vs.* sparsely cellular), and whether significant red blood cell contamination of the sample was present.

Data analysis

DESI-MS ion images. Surgical biopsy and FNA smear data acquired using XCalibur 2.0 (.raw) were converted with an in-house program into files compatible with BioMap software (http://www.maldi-msi.org). BioMap was used to generate 2D ion images (retaining spatial relationships and displaying relative mass spectral abundance of particular mass-to-charge ratios), select regions of interest (ROI) based on pathology, and export data for multivariate analysis. An in-house MatLab (MathWorks, Inc., Natick, MA, USA) routine was used to explore chemical features present in two dimensional DESI ion images. PCA was performed upon MS hyperspectral datacubes, the composite of spatial dimension ("*x*" and "*y*"), *m*/*z* value, and corresponding *m*/*z* intensity, and plotted using an interactive brushing procedure,[26] see ESI† for more details.

Multivariate analysis. PCA was used to explore DESI-MS data and visualize the grouping of samples resulting from chemical similarity.[27] Multivariate analysis of tissue sections was performed using in-house MatLab routines. The mass range was truncated (*m*/*z* 700 – 1000) for statistics, as it was empirically found to contain less analytical variability, providing more consistent and clear separation with regards to disease state (*i.e.* normal *vs.* tumor). Two specimens were excluded from statistics: one lymphoma sample (due to poor MS signal) and a metastatic carcinoma. MS data were normalized by the total ion current (TIC) and column-centered (*i.e.* mean-centered). Neither background subtraction nor a smoothing algorithm was applied to the MS data before PCA. LDA was performed for discriminant classification after unsupervised data compression by PCA (*i.e.* PCA-LDA), as reported elsewhere.[28] The first 8 principal components (PCs), accounting for ~90% of total data variation, were used. Classification rates report the correct classification of samples in the final PCA-LDA model. Cross validation (CV) with 5 deletion groups was used to test the prediction ability, reported as CV sensitivity and specificity. Sensitivity was calculated as the percent of the objects in the evaluation sets correctly accepted by the model. Specificity was calculated as the percent of the objects of other categories correctly rejected by the model. Average DESI mass spectra obtained from FNA smears were compared with those of surgical biopsy *via* multivariate statistics. A linear discriminant model (*i.e.* PCA-LDA) was built in PARVUS (University of Genova, Italy) using mass spectra from surgical biopsy tissue sections, to which FNA smear mass spectra were classified. The results and prediction rates are tabulated.

Results and discussion

DESI-MS imaging of lymph node tissue sections

Surgically excised lymph node biopsies were sectioned and analyzed by DESI-MS imaging, providing chemical and spatial information concurrently. The methodology employed follows that of histopathological evaluation of tissue, while providing molecular information. Tissue diagnosis by DESI-MS is performed with a spatial resolution larger than traditional histopathology (hundreds of microns *versus* tens of microns); however, it provides chemical information otherwise unobtainable by traditional histopathology. DESI-MS analysis of tissue sections aims to explore and establish the lipid profiles indicative of normal and NHL tumor subtypes. Negative mode DESI mass spectra showed ionized fatty acids (*e.g.* oleic acid, *m*/*z* 281), fatty acid dimers, and glycerophospholipids from *m*/*z* 700 – 1000 (*e.g.* PI(38:4), *m*/*z* 885), ESI Fig. 1 and Table 2.† The major glycerophospholipids (GPL) ions observed included major structural and signaling lipid classes: phosphatidylinositols (PI), phosphatidylserines (PS), phosphatidylethanolamines (PE), and phosphatidylglycerols (PG). The majority of lymphoma-containing tissue sections displayed a conserved pattern of lipids (*i.e.* ion, *m*/*z*, and corresponding relative abundance), or lipid profile, that contrasted markedly with that of normal tissue, and varied more slightly between B-cell and T-cell subtypes. Minute analytical variances in the lipid profile and signal intensity were attributed to freezing and sectioning artifacts. These small areas contributed insignificantly upon averaging and did not compromise the ability to ascertain MS information.

DESI-MS ion images, two dimensional spatial distribution of *m*/*z versus* the corresponding ion abundance represented in false-color, revealed the majority of samples to be chemically homogenous, *i.e.* to have similar lipid profiles. Diffuse large B-cell lymphoma, Fig. 1A was particularly homogenous, spatially and chemically, following the propensity of this cancer to diffusely obliterate normal lymph node architecture. Normal samples were also relatively homogenous in regards to chemical composition and spatial distribution. Interestingly, regions of normal lymph node anatomy, *e.g.* cortex and medulla, yielded nearly identical lipid profiles although differing in absolute MS intensity. The similarity of the lipid profile was unexpected as anatomical distribution of B-cell and T-cell lymphocytes is known to differ in lymph nodes: B-cells are found in densely packed follicles within the cortex and T-cells are present in the surrounding paracortex. The medulla contains a mixture of plasma cells, macrophages, and T-cells. The absolute MS signal intensity varied between the cortex and medulla, the latter yielded less signal. This intensity difference might result from the anatomical differences between the two regions that are not detected, such as the greater density of blood vessels and vascular sinuses within the lymph node medulla, which reduces the overall cellular density. The spatial resolution of DESI-MS data acquisition used does not allow for such anatomical structures to be visualized. MS imaging at higher resolution (<200 μm), possible by secondary-ion MS, matrix-assisted laser desorption, DESI, and nanoDESI,[12–14,16,29] could visualize these anatomical regions with a non-linear increase in analysis time (analysis time increases with the reciprocal of the square of spatial resolution); however, investigation of normal lymph node anatomy is beyond the scope of the intended application.

Differences in the chemical information within analyzed tissue sections, disregarding previously discussed MS intensity differences, were noted in some of the normal and tumor specimens. In all of these instances (independent of tissue disease state, *i.e.* normal *versus* tumor) the difference resulted from the presence of perinodal adipose tissue, as determined by *post hoc* histopathology. Specimen 31 is illustrative, Fig. 1B, a tissue section comprised primarily of a B-cell tumor with smaller regions of non-neoplastic, perinodal adipose tissue. The tumor regions have a common lipid profile that is homo-

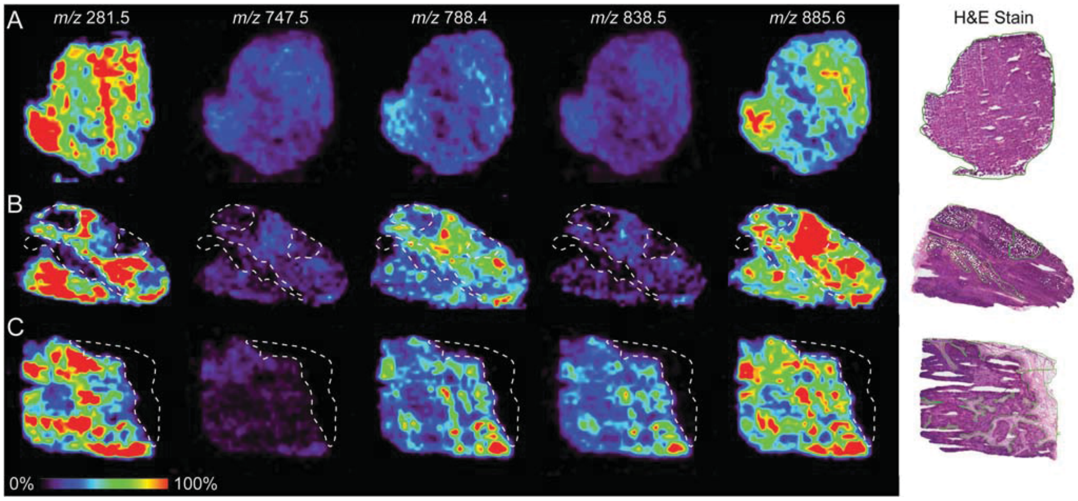

Fig. 1 Selected negative mode DESI-MS ion images displaying the distribution of ions *m*/*z* 281.5, 747.5, 788.4, 838.5, and 885.6 and the corresponding H&E stain. (A) Specimen 18 is representative of B-cell lymphoma samples in regards to chemical and spatial homogeneity. (B) Specimen 31, B-cell lymphoma, contained small regions of perinodal adipose (outlined). (C) Specimen 42, illustrative of normal samples. The large region of perinodal adipose (outlined) was chemically difference than that of normal lymph node tissue.

genous throughout the tumor region; however, the lipid profile of small regions corresponding to perinodal adipose tissue (outlined) are significantly different and overall lower in absolute intensity as seen in the ion images (particularly *m*/*z* 281.5). The chemical difference of this region was further explored using PCA and an interactive brushing procedure, see ESI Fig. 2.† The PCA score plot, displaying each pixel of specimen 31, indicated three groups: B-cell lymphoma associated pixels (red selection), perinodal adipose associated pixels (green selection), and background associated pixels (black). The results of visual interpretation and PCA correlated well with the pathological assessment, considering the differences in spatial resolution of MS imaging and histopathology. Perinodal adipose tissue was also detected in some normal lymph nodes, for example specimen 42, as shown in Fig. 1C. The difference in the lipid profile was again evident between the two tissue types with negative mode GPL signal only noted in the lymph node parenchyma. The lack of GPL signal in adipose tissue is likely correlated to adipocytes (*i.e.* fat cells), which typically possess a large cytoplasmic volume to GPL membrane surface area ratio. Further, adipocytes contain greater levels of triglycerides and cholesteryl esters which are not readily detected in the negative mode with the solvent conditions chosen; however, previous DESI experiments have detected such compounds in positive ion mode from biological material with relative ease as silver adducts.[30]

Differentiating lipid profiles in NHL tissue sections

The lipid profiles of tissue sections were explored for molecular-based differentiation of disease state (normal *versus* tumor) and NHL tumor subtype (*i.e.* B-cell *versus* T-cell). The average DESI mass spectrum (from *m*/*z* 700 – 1000) of normal lymph node (n = 22), B-cell lymphoma (n = 22), and T-cell lymphoma (n = 7) tissue sections, green, blue, and gold respectively, are displayed in Fig. 2A–C. The ratio of MS abundance of *m*/*z* 788.3, 838.3, and 885.5 indicated, visually, molecular differences between disease states. Nearly all B-cell samples were diagnosed as diffuse large B-cell lymphoma, differences in the lipid profile are noted in comparison to the average normal spectrum. A small number of T-cell lymphoma tissue sections were analyzed, diagnosed as peripheral T-cell lymphoma, not otherwise specified (n = 4) and T-zone lymphoma (n = 3). Spectral differences were also noted between normal and T-cell NHL, but the limited number of samples and multiple T-cell subtypes preclude definitive conclusions. Less abundant peaks present in B-cell and T-cell lymphoma also differed in abundance from normal samples including *m*/*z* 747.4, 773.3, 786.4, 812.4, 883.5. These ions and their altered relative abundance mirror those reported previously by Eberlin *et al.* in murine and human lymphoma specimens.[31] One metastatic carcinoma, specimen 12, was analyzed and yielded different lipid profiles from normal and lymphoma with

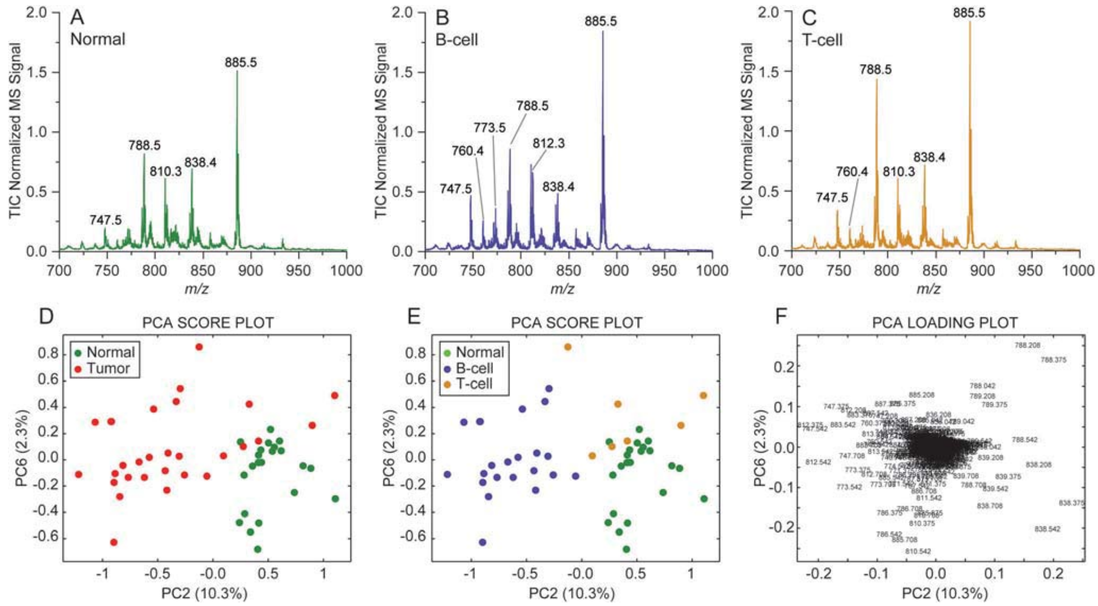

Fig. 2 Average negative mode DESI mass spectrum of tissue sections: (A) normal lymph node (n = 22), (B) B-cell lymphoma (n = 22), and (C) T-cell lymphoma (n = 7). (D) PCA score plot of normal (green) and tumor (red) samples. (E) PCA score plot of normal (green), B-cell lymphoma (blue), and T-cell lymphoma (gold) samples. (F) PCA loading plot corresponding to panel D&E with *m*/*z* annotated.

strong alterations in m/z 819, 834, 865, and 867 (ESI Fig. 3†). Abbassi-Ghadi and coworkers have previously analyzed metastatic tumors in lymph nodes by DESI, concluding that the chemical information corresponded to that of the primary tumor and had clearly different from adjacent normal lymph node.[32] Extrapolating from that work, the lipid profile of specimen 12 might correlate with that of the primary tumor; however, biopsies of the primary tumor were not available for analysis.

Principal component analysis was performed on the average spectrum of each tissue section, offering an unbiased method for qualitatively assessing the molecular information associated with the pathology-defined condition. Disease state differentiation (normal *vs.* tumor) was the initial level of diagnostic information explored. Normal lymph node (green) and tumor (red) samples were appropriately grouped as shown in Fig. 2D. Dispersion of the tumor samples in the PCA score plot, compared with the normal samples, is indicative of greater chemical heterogeneity within lymphoma – matching known diversity of the disease.[1] The dispersion of the lymphoma samples appears to be related to tumor immunophenotype, Fig. 2E: normal (green), B-cell lymphoma (blue), and T-cell lymphoma (gold). The PCA loading plot, displayed in Fig. 2F, aided in understanding which lipids from m/z 700 – 1000 contributed most to PC2 and PC6 computations (see ESI Fig. 4† for additional information). Distinguishing NHL subtypes represents a deeper level of diagnostic information, which commonly requires IHC/ICC; the chemical information obtained by DESI may circumvent or augment such protocols. The separation of B-cell and T-cell lymphoma is suggested in Fig. 2E; however, expansion of NHL subtypes is necessary to confirm this initial report. More detailed exploration of the chemical differences was performed by iterative study of the relationship between disease states rather than together as in Fig. 2. For example, the chemical difference between B-cell and T-cell NHL tumors is more apparent upon removal of normal samples (ESI Fig. 5†). The separation noted must be taken as preliminary, particularly for T-cell tumors, based on the relatively small sample size and known genetic diversity of lymphomas. The ability to subtype tumors using DESI-MS has been previously demonstrated, *e.g.* brain and kidney tumors,[19,20] but has not been previously reported in lymphoma. Diagnostic information acquired by DESI would serve to support pathological diagnosis, particularly relating to tumor subtyping as an alternative to IHC.

The discriminatory performance of DESI-MS in determining disease state and subsequently tumor subtype from tissue sections was explored *via* PCA-LDA. The classification rate in PCA-LDA model creation was 100% for normal and tumor. Cross-validation was performed resulting in the predicted sensitivity and specificity results displayed in Table 1. Further, PCA-LDA was performed separately taking the lymphoma subtypes into consideration, modelling classification rates were 100%, 99% and 94% for normal, B-cell, and T-cell respectively. CV indicated two misclassifications (T-cell predicted as normal, and B-cell predicted as T-cell). The predicted sensitivity and specificity for NHL subtyping is tabulated in Table 2. The CV sensitivity of T-cell lymphoma (85.7%) was relatively poor in comparison to the other states (normal, 100% and B-cell lymphoma, 95.5%), likely the result of a smaller sample size (n = 7) or the presence of two different subtypes (*i.e.* peripheral and T-zone).

Table 1 CV results of DESI-MS in discriminating disease state (normal *vs.* tumor) in tissue sections

		Pathological diagnosis	
		Normal	Tumor (B- & T-cell NHL)
DESI-MS prediction	Normal	22	2
	Tumor (B- & T-cell NHL)	0	27
CV sensitivity (%)		100.0	93.1
CV specificity (%)		93.1	100

Table 2 CV results for NHL subtyping of tissue sections by DESI-MS

		Pathological diagnosis		
		Normal	B-cell NHL	T-cell NHL
DESI-MS prediction	Normal	22	0	1
	B-cell NHL	0	21	0
	T-cell NHL	0	1	6
CV sensitivity (%)		100	95.5	85.7
CV specificity (%)		96.4	100	97.7

DESI-MS imaging of fine needle aspirates

Histopathological evaluation of surgically excised lymph nodes, the gold standard for lymphoma diagnosis, is an invasive procedure and therefore not suitable for rapid preliminary diagnosis of NHL. Fine needle aspirate biopsy is a less expensive, less invasive, and less technically demanding method, and therefore a reasonable alternative. FNA tend to be less reliable than surgical biopsy, in part due to the limited discriminatory ability of cytology in comparison to histopathology. However, DESI-MS analysis of FNA smears provided molecular information that is similar to that of tissue sections and offers an alternative to FNA cytology, aimed at enhancing diagnostic capability.

FNA smears, prepared using standard protocols, were analyzed without any pre-treatment. DESI-MS was performed on a small area of the smear, not the entirety of the smear, representing a time reducing strategy for preliminary diagnosis. It was assumed that aspiration and subsequent smearing, was sufficiently homogenizing. The MS data obtained from FNA smears were highly reminiscent of those for surgical biopsy tissue sections. The average mass spectra for normal and B-cell lymphoma are displayed in Fig. 3, with more detail provided in ESI Fig. 6.† The chemical information obtained from FNA appears to be identical in nature to that of tissue sections

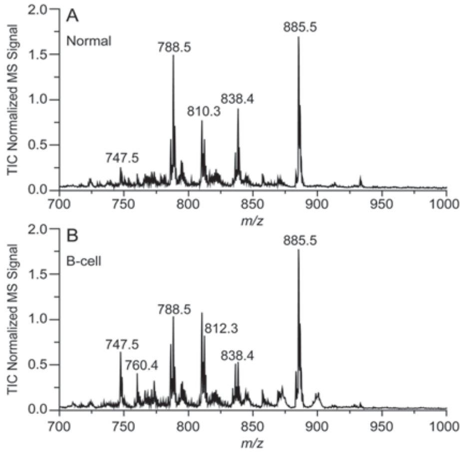

Fig. 3 Average (−)DESI-MS spectrum for (A) normal FNA (*n* = 7) and (B) B-cell lymphoma FNA (*n* = 28).

suggesting that the type of sample does not impact ability to acquire chemical information correlated to disease state. The strategy of using DESI spectra obtained from tissue sections serves as an important reference in this case, having been used previously in cancer diagnosis,[17–23] thus allowing evaluation of FNA as a new type of sample for the same DESI methodology.

Unsurprisingly, subtle differences do exist between tissue sections and FNA smears which did not preclude acquisition of mass spectral information but rather influenced data quality. FNA smears were nearly always chemically homogenous, *i.e.* the lipid profile was similar in all areas of the smear, supporting the assumption of sufficient homogenization, while difference in the signal intensity were common (ESI Fig. 7†). Two major variables in FNA smears were found to affect MS intensity: the quantity of cellular material aspirated and the degree of dilution due to smearing. The effect of quantity is noted in ESI Fig. 8† in which the heterogeneity present in the ion image results from variable amount of material – signal intensity is correlated with material quantity. The second variable is the degree of smearing of the aspirated sample which dilutes the cellular material on the glass slide. This dilution is necessary for cytologic evaluation using light microscopy, in which morphologic evaluation of isolated cells is desirable, but is deleterious for chemical analysis by DESI-MS. Slight modification to current FNA protocols that compensate for these effects is likely to increase DESI reproducibility, MS data quality, and capability for molecular diagnosis. Additionally, differences in the lipid profile were noted in cases of obvious blood contamination of the aspirated sample, resulting in a visually red coloration to the smear. The presence of blood contamination significantly increased one particular lipid, *m*/*z* 810, which corresponds to PS(40:6), a major membrane constituent of erythrocytes[33] and therefore easily detected. Minor blood contamination did not seem to compromise the ability to determine disease state. Subsequent staining of FNA smears (Wright's stain) analyzed by DESI and evaluation by light microscopy, indicated cellular damage, which could result from physical damage during smearing or freeze thaw cycle. Certainly, DESI has the potential to produce the observed cellular damage *via* physical (*e.g.* pneumatic) forces or chemical fixation (*i.e.* organic solvent). An expert cytopathologist commented that the morphologic changes in the cells appeared similar to those commonly observed in samples exposed to formalin, a common chemical fixative, which supports the latter reason for the observed effect. This observation is quite interesting in that it contrasts the preservation of morphology during analysis of histologic tissue sections – no effect on histomorphology is noted using dimethylformamide-acetonitrile as a DESI solvent system. One biological reason for this observation is the presence of stromal tissue and extracellular matrix in histologic sections, which may minimize the cellular damage of DESI analysis relative to what was observed in FNA smears, which would presumably contain less of these protective elements.

Differentiation of disease state using FNA smears

The chemical information obtained using DESI-MS from FNA smears was evaluated by multivariate statistics, undertaken to determine FNA's potential diagnostic performance and explore how translatable the chemical information obtained from tissue sections are to FNA smears. In clinical practice, the information relevant in FNA evaluation is the presence or absence of tumor, and serves only to provide a rapid, preliminary diagnosis which requires subsequent confirmation by more accurate methods such as histopathology. PCA-LDA was applied and performed by building a classification training set using tissue section data and evaluating the FNA smear data. PCA-LDA prediction rates are displayed in Table 3. Prediction of normal was 85.7% and tumor was 89.3%. The preliminary results displayed indicate that DESI-MS analysis of FNA smears has diagnostic potential. Further, the results support that the chemical information relevant to disease state is equivalently detected by DESI-MS. FNA smears, neither adapted nor optimized for MS analysis, provided reasonable classification results, provided that FNA smears are known to be less reliable than surgical biopsy samples evaluated by histopathology.

Table 3 PCA-LDA prediction of FNA smears analyzed by DESI-MS

		Pathological diagnosis[a]	
		Normal	B-cell NHL
DESI-MS prediction	Normal	6	3
	B-cell NHL	1	25
PCA-LDA prediction rate		85.7%	89.3%

[a] Note four ROIs were taken for specimen 8, 13, and 19, and two ROIs from specimen 35.

Beyond the rapid molecular diagnosis of NHL by DESI-MS *via* FNA analysis, the envisioned application, has the potential for rapid tumor subtyping. PCA cross-validation of tissue sections indicated the possibility for tumor subtyping; however, this could not be explored based on FNA sample numbers. Surely, this requires a larger and more diverse sample set, particularly with knowledge of NHL tumor heterogeneity. The primary goal of FNA analysis by DESI was demonstrated: rapid molecular-based dichotomous delineation of disease state (*i.e.* normal and tumor), which has potential to be a significant advancement in the rapid diagnosis of non-Hodgkin's lymphoma.

Conclusion

Differences in the lipid profile, acquired by DESI-MS, allowed differentiation of normal lymph node and NHL tumors in tissue sections (obtained by surgical biopsy) and FNA smears. DESI-MS imaging of tissue sections allowed chemical information to be obtained and explored. Normal lymph node tissue was chemically homogenous while differences in absolute signal were noted between regions of normal lymph node anatomy, *e.g.* medulla and cortex. Tumor samples were generally homogenous, particularly diffuse large B-cell lymphoma samples, matching known histomorphology. Multivariate statistics allowed for differentiation of normal and tumor tissue sections yielding an overall predicted CV sensitivity of 96%. Further, subtyping of NHL tumors is suggested with an equal rate of predicted classification.

FNA smears, previously unexplored for use in diagnosis using ambient ionization – mass spectrometry, provided the same chemical information relevant to disease state differentiation detected from tissue sections. FNA smear data applied to a tissue section-based classification system yielded an average prediction rate of 87.5% for disease states. MS signal was dependent on the composition (*e.g.* blood contamination), aspirated material quantity and smearing. The act of smearing of FNA, while ideal for cytology, dilutes the cellular material necessary for DESI-MS lipid analysis. Improvement in the protocols for FNA preparation, with tailoring specifically for MS analysis is likely to improve results. The molecular information detected from FNA smears are not subject to the same set of problems (*e.g.* physical damage of cells) experienced in cytopathology, and therefore could improve diagnostic yield. Cellular damage was noted after DESI analysis upon FNA samples, effecting only subsequent pathology and not the molecular information. The reason for this damage is presently unknown, but might result from chemical damage. Analysis of FNA material by other ambient methods such as PESI or paper spray ionization represents another possible direction of development.[34] The direct aspiration of material onto paper for PS analysis eliminates smearing and may provide additional advantages in regards to MS analysis. The informative but less invasive collection of FNA smears, also performed during diagnosis of other cancers, particularly those of the breast, thyroid, and salivary gland, is clearly best suited to answer the question of rapid preliminary diagnosis, "Is this sample normal or cancerous?"

DESI-MS analysis of tissue sections provided a means of exploring and establishing the lipid profiles indicative of normal lymph node and NHL tumors. FNA smears mimic those changes, primarily in GPL composition, which are certainly related to cellular and morphological changes that occur with NHL. The polar lipids detected in the negative ion mode represent only a fraction of metabolites, and further study of the metabolome may reveal additional diagnostic information. The subtype prevalence, clinical behavior, and chemical changes in GPL emulate that of human NHL,[31] supporting development of canine comparative models. The methodology outlined here is applicable to dogs while translation to humans is foreseeable.

Acknowledgements

The authors thank Dr Christina Ferreira and Dr Paolo Oliveri for their contributions. Funding support was provided by Purdue University Center for Cancer Research SIRG Program, Award 8000062024.

References

1 D. Ito, A. M. Frantz and J. F. Modiano, *Vet. Immunol. Immunopathol.*, 2014, **159**, 192–201.
2 NIH-NCI, SEER Stat Fact Sheets: Non-Hodgkin Lymphoma, 2014.
3 L. Marconato, M. E. Gelain and S. Comazzi, *Hematol. Oncol.*, 2013, **31**, 1–9.
4 V. E. Valli, M. San Myint, A. Barthel, D. Bienzle, J. Caswell, F. Colbatzky, A. Durham, E. Ehrhart, Y. Johnson and C. Jones, *Vet. Pathol.*, 2011, **48**, 198–211.
5 F. Ponce, T. Marchal, J. Magnol, V. Turinelli, D. Ledieu, C. Bonnefont, M. Pastor, M. Delignette and C. Fournel-Fleury, *Vet. Pathol.*, 2010, **47**, 414–433.
6 S. T. Hehn, T. M. Grogan and T. P. Miller, *J. Clin. Oncol.*, 2004, **22**, 3046–3052.
7 D. K. Das, *Diagn. Cytopathol.*, 1999, **21**, 240–249.
8 O. Landgren, A. Porwit MacDonald, E. Tani, M. Czader, G. Grimfors, L. Skoog, A. Ost, C. Wedelin, U. Axdorph and E. Svedmyr, *Hematology J.*, 2004, **5**, 69–76.
9 A. Venter, P. E. Sojka and R. G. Cooks, *Anal. Chem.*, 2006, **78**, 8549–8555.
10 A. B. Costa and R. Graham Cooks, *Chem. Phys. Lett.*, 2008, **464**, 1–8.
11 J. Oetjen, K. Veselkov, J. Watrous, J. S. McKenzie, M. Becker, L. Hauberg-Lotte, J. H. Kobarg, N. Strittmatter, A. K. Mróz, F. Hoffmann, D. Trede, A. Palmer, S. Schiffler, K. Steinhorst, M. Aichler, R. Goldin, O. Guntinas-Lichius, F. von Eggeling, H. Thiele, K. Maedler, A. Walch, P. Maass,

P. C. Dorrestein, Z. Takats and T. Alexandrov, *Gigascience*, 2015, **4**, 20.
12 R. D. Addie, B. Balluff, J. V. Bovée, H. Morreau and L. A. McDonnell, *Anal. Chem.*, 2015, **87**, 6426–6433.
13 A. Bodzon-Kulakowska and P. Suder, *Mass Spectrom. Rev.*, 2015, DOI: 10.1002/mas.21468.
14 C. Wu, A. L. Dill, L. S. Eberlin, R. G. Cooks and D. R. Ifa, *Mass Spectrom. Rev.*, 2013, **32**, 218–243.
15 X. Xiong, W. Xu, L. S. Eberlin, J. M. Wiseman, X. Fang, Y. Jiang, Z. Huang, Y. Zhang, R. G. Cooks and Z. Ouyang, *J. Am. Soc. Mass Spectrometry*, 2012, **23**, 1147–1156.
16 J. C. Vickerman, *Analyst*, 2011, **136**, 2199–2217.
17 A. L. Dill, D. R. Ifa, N. E. Manicke, A. B. Costa, J. A. Ramos-Vara, D. W. Knapp and R. G. Cooks, *Anal. Chem.*, 2009, **81**, 8758–8764.
18 J. M. Wiseman, S. M. Puolitaival, Z. Takáts, R. G. Cooks and R. M. Caprioli, *Angew. Chem., Int. Ed.*, 2005, **117**, 7256–7259.
19 L. S. Eberlin, I. Norton, D. Orringer, I. F. Dunn, X. Liu, J. L. Ide, A. K. Jarmusch, K. L. Ligon, F. A. Jolesz and A. J. Golby, *Proc. Natl. Acad. Sci. U. S. A.*, 2013, **110**, 1611–1616.
20 A. L. Dill, L. S. Eberlin, C. Zheng, A. B. Costa, D. R. Ifa, L. Cheng, T. A. Masterson, M. O. Koch, O. Vitek and R. G. Cooks, *Anal. Bioanal. Chem.*, 2010, **398**, 2969–2978.
21 K. S. Kerian, A. K. Jarmusch, V. Pirro, M. Koch, T. Masterson, L. Cheng and R. G. Cooks, *Analyst*, 2015, **140**, 1090–1098.
22 L. S. Eberlin, R. J. Tibshirani, J. Zhang, T. A. Longacre, G. J. Berry, D. B. Bingham, J. A. Norton, R. N. Zare and G. A. Poultsides, *Proc. Natl. Acad. Sci. U. S. A.*, 2014, **111**, 2436–2441.
23 S. Santagata, L. S. Eberlin, I. Norton, D. Calligaris, D. R. Feldman, J. L. Ide, X. Liu, J. S. Wiley, M. L. Vestal and S. H. Ramkissoon, *Proc. Natl. Acad. Sci. U. S. A.*, 2014, **111**, 11121–11126.
24 J. Liu, R. G. Cooks and Z. Ouyang, *Anal. Chem.*, 2011, **83**, 9221–9225.
25 L. S. Eberlin, C. R. Ferreira, A. L. Dill, D. R. Ifa, L. Cheng and R. G. Cooks, *ChemBioChem*, 2011, **12**, 2129–2132.
26 V. Pirro, L. S. Eberlin, P. Oliveri and R. G. Cooks, *Analyst*, 2012, **137**, 2374–2380.
27 R. Bro and A. K. Smilde, *Anal. Methods*, 2014, **6**, 2812–2831.
28 C. R. Ferreira, V. Pirro, L. S. Eberlin, J. E. Hallett and R. G. Cooks, *Anal. Bioanal. Chem.*, 2012, **404**, 2915–2926.
29 J. Laskin, B. S. Heath, P. J. Roach, L. Cazares and O. J. Semmes, *Anal. Chem.*, 2011, **84**, 141–148.
30 V. Pirro, P. Oliveri, C. R. Ferreira, A. F. González-Serrano, Z. Machaty and R. G. Cooks, *Anal. Chim. Acta*, 2014, **848**, 51–60.
31 L. S. Eberlin, M. Gabay, A. C. Fan, A. M. Gouw, R. J. Tibshirani, D. W. Felsher and R. N. Zare, *Proc. Natl. Acad. Sci. U. S. A.*, 2014, **111**, 10450–10455.
32 N. Abbassi-Ghadi, K. Veselkov, S. Kumar, J. Huang, E. Jones, N. Strittmatter, H. Kudo, R. Goldin, Z. Takáts and G. Hanna, *Chem. Commun.*, 2014, **50**, 3661–3664.
33 K. Leidl, G. Liebisch, D. Richter and G. Schmitz, *Biochim. Biophys. Acta, Mol. Cell Biol. Lipids*, 2008, **1781**, 655–664.
34 C. H. Lin, W. C. Liao, H. K. Chen and T. Y. Kuo, *Bioanalysis*, 2014, **6**, 199–208.

Lipid and metabolite profiles of human brain tumors by desorption electrospray ionization-MS

Alan K. Jarmusch[a], Valentina Pirro[a], Zane Baird[a], Eyas M. Hattab[b], Aaron A. Cohen-Gadol[c], and R. Graham Cooks[a,1]

[a]Department of Chemistry and Center for Analytical Instrumentation Development, Purdue University, West Lafayette, IN 47907; [b]Department of Pathology and Laboratory Medicine, Indiana School of Medicine, Indianapolis, IN 46202; and [c]Department of Neurological Surgery, Indiana University School of Medicine, Indianapolis, IN 46202

This contribution is part of the special series of Inaugural Articles by members of the National Academy of Sciences elected in 2015.

Contributed by R. Graham Cooks, December 21, 2015 (sent for review November 24, 2015; reviewed by Richard N. Zare and Arash Zarrine-Afsar)

Examination of tissue sections using desorption electrospray ionization (DESI)-MS revealed phospholipid-derived signals that differ between gray matter, white matter, gliomas, meningiomas, and pituitary tumors, allowing their ready discrimination by multivariate statistics. A set of lower mass signals, some corresponding to oncometabolites, including 2-hydroxyglutaric acid and *N*-acetylaspartic acid, was also observed in the DESI mass spectra, and these data further assisted in discrimination between brain parenchyma and gliomas. The combined information from the lipid and metabolite MS profiles recorded by DESI-MS and explored using multivariate statistics allowed successful differentiation of gray matter (n = 223), white matter (n = 66), gliomas (n = 158), meningiomas (n = 111), and pituitary tumors (n = 154) from 58 patients. A linear discriminant model used to distinguish brain parenchyma and gliomas yielded an overall sensitivity of 97.4% and a specificity of 98.5%. Furthermore, a discriminant model was created for tumor types (i.e., glioma, meningioma, and pituitary), which were discriminated with an overall sensitivity of 99.4% and a specificity of 99.7%. Unsupervised multivariate statistics were used to explore the chemical differences between anatomical regions of brain parenchyma and secondary infiltration. Infiltration of gliomas into normal tissue can be detected by DESI-MS. One hurdle to implementation of DESI-MS intraoperatively is the need for tissue freezing and sectioning, which we address by analyzing smeared biopsy tissue. Tissue smears are shown to give the same chemical information as tissue sections, eliminating the need for sectioning before MS analysis. These results lay the foundation for implementation of intraoperative DESI-MS evaluation of tissue smears for rapid diagnosis.

ambient ionization | MS imaging | multivariate statistics | pathology | neurosurgery

MS is increasingly being used in medicine (e.g., in clinical chemistry, pharmaceutical development, and proteomics). Ambient ionization methods generate ions under atmospheric conditions, with minimal to no sample preparation (1). Desorption electrospray ionization (DESI), an ambient method that uses a spray of charged solvent as the projectile, provides rapid chemical information while preserving tissue and cellular morphology, allowing subsequent histopathology on the same specimen (2). This feature allows integration of DESI-MS into current workflows and postacquisition pathology. DESI-MS has been used to study prostate cancer (3), bladder cancer (4), kidney cancer (5), seminoma (6), lymphoma (7), gastrointestinal cancer (8), and others. In each case, the recorded pattern of lipid signals allows the differentiation of cancer from normal tissue. DESI-MS has been previously used to explore chemical differences among glioma subtypes, grades, and tumor cell concentrations (relative percentage of tumor compared with parenchyma) (9, 10). Meningiomas have also been studied previously and were distinguished from normal dura mater (11).

The incidence of brain tumors is approximately the same as that of non-Hodgkin's lymphoma, melanoma, and urinary bladder cancer in adults over 20 y of age, and it is even more prevalent among children. Gliomas (30%), meningiomas (33%), and pituitary tumors (15%) account for the majority of brain tumors in adults (12). The brain parenchyma is comprised of glia (e.g., astrocytes and oligodendrocytes) and neurons. In many cases, surgical resection is the most effective treatment option; however, surgery must contend with the dilemma of maximizing tumor excision while minimizing unintended neurological deficits. MRI, a critical imaging method, aids in defining the location and size of the tumor (13). The nuclear spin of hydrogen is exploited by MRI, allowing visualization of different anatomical structures (e.g., T1-weighted MRI) or pathologies (e.g., T2-weighted and contrast-enhanced MRI). Additional information can be obtained by positron emission tomography, functional MRI, diffusion weighted imaging, fluid-attenuated inversion recovery, and magnetic resonance spectroscopic imaging (MRSI). Raman spectroscopy performed in vivo seeks to provide chemical information that allows rapid identification of cancerous tissue (14). Fluorescence imaging uses appropriate molecular labels to visualize tumors during surgery (15, 16). The information provided by these methods is used primarily to visualize the tumor and assist in surgical resection. Histopathology performed on frozen tissue sections and tissue smears is the most common source of important pathologic information, specifically the type of tumor (e.g., glioma) and grade (e.g., low grade), which is provided during surgery. This pathologic analysis is often repeated for infiltrative tumors to guide the extent of resection at the tumor margins. Currently, this information is obtained outside of the operating room, taking upward of 20 min per sample and prolonging surgery. Histopathology relies heavily on morphologic and cytologic features revealed by staining of

Significance

Brain tumors can lead to a significant source of morbidity and mortality. The primary treatment is microsurgical resection, and the extent of resection is associated with length of survival. Unfortunately, reliable intraoperative tools for diagnosis and safe maximal resection of the tumor mass are lacking. Mass spectra (lipid and metabolite profiles) can be used to distinguish between healthy and diseased tissues by comparison of patterns of peak intensities using multivariate statistics. This experiment can be done on a timescale amenable to intraoperative analysis using tissue smears. These data can provide surgeons with near real-time pathologic information and guide the intraoperative resection of the tumor at the difficult to detect peritumoral borders.

Author contributions: A.K.J., V.P., and R.G.C. designed research; A.K.J., V.P., Z.B., E.M.H., and A.A.C.-G. performed research; A.K.J. and V.P. analyzed data; and A.K.J., V.P., Z.B., E.M.H., A.A.C.-G., and R.G.C. wrote the paper.

Reviewers: R.N.Z., Stanford University; and A.Z.-A., University of Toronto.

The authors declare no conflict of interest.

[1]To whom correspondence should be addressed. Email: cooks@purdue.edu.

This article contains supporting information online at www.pnas.org/lookup/suppl/doi:10.1073/pnas.1523306113/-/DCSupplemental.

cellular structures (e.g., nucleus and cytoplasm). However, brain tumors exhibit large genetic variability and genomic instability, which remain invisible to microscope-based pathology. Auxiliary testing, frequently immunohistochemistry or genetic sequencing, supports pathologic diagnosis and has been used to estimate treatment response (as in pharmacogenomics). Genetic testing remains time-consuming [reporting of isocitrate dehydrogenase (IDH) mutation status, a prognostic marker, can take weeks], creating delay in pathologic diagnosis and rendering treatment. However, recently, Shankar et al. (17) reported a genotyping method for IDH and telomerase reverse transcriptase mutations, with results available in 60 min.

Previous studies (3–11) have shown tissue discrimination by mass spectral profiles (*m/z* values and associated abundances) characteristic of different tissue types, including different disease states. Rapid and direct analysis of tissue provides molecular information on multiple compounds and is obtained on a time-scale of seconds to a few minutes. In this way, ambient ionization MS profiling stands in stark contrast to "-omics" techniques, which are based on separation (e.g., liquid chromatography) before MS and in which complex samples are extensively processed (e.g., by desalting, extraction, and derivatization) to reveal, in detail, the particular compounds present. Both the time required for analysis and the complexity of high-performance hyphenated MS systems mean that they are not amenable to intraoperative use.

The potential diagnostic value of using ambient ionization and MS profiles, especially those based on lipids (18), is increasingly being recognized as reflected by a growing number of studies. Detection of metabolites by ambient ionization has also proven useful in the detection of genetic mutations, such as IDH, but it remains underexplored for potential diagnostic value. Differences in the lipid composition of renal cell carcinoma (19) and colon cancer (20) from their respective normal parenchyma were detected by positive ion probe electrospray ionization-MS. Touch spray, a probe method allowing user-guided sampling, serves to differentiate prostate cancer from normal tissue based on glycerophospholipid distributions (3). Similar methods of ionization have been used for the detection of lipids from lung (21) and brain cancer (22). DESI-MS imaging of stereotactically registered brain tumor samples (23) gave results that correlated with histopathology and illustrated the potential for determining tumor cell concentration near the resection margins (10). The analysis of gastric cancer surgical margins has been reported recently, including pixel by pixel classification of heterogeneous tissue sections (8). Brain and other cancers have been investigated using rapid evaporative ionization-MS, a method that provides lipid-based differentiation between cancerous and normal tissue and has been performed in vivo on patients undergoing surgical resection with promising results; however, electrocauterization is destructive and should be used with discretion (24). Establishing a robust classification method is of vital importance and best implemented by including normal tissue. Obtaining normal tissue is particularly difficult in the case of brain tumors, in which absolute normal rarely exists for scientific study. Currently, intraoperative DESI-MS analysis is limited by the need for freezing and cryosectioning before analysis; therefore, we describe the use of tissue smears as a means to quickly acquire differentiating chemical information. There is little doubt that development of molecular techniques that rapidly discriminate cancerous tissue would be of great benefit to supplement intraoperative decision-making and pathologic evaluation.

Results and Discussion

DESI-MS Imaging of Human Brain Tissue Sections. We explore the chemical information obtained from banked frozen brain tissue sections by DESI-MS performed in the imaging mode. Negative ionization DESI-MS images were recorded using different MS tune methods consecutively from the same tissue section. The main features of the MS profiles in the ranges *m/z* 200–1,000 and *m/z* 80–200 were found to be associated with glycerophospholipids and metabolites, respectively, and are referred to throughout as the lipid and the metabolite profiles, respectively. These two MS profiles, containing many ions with relative abundances characteristic of tissue type, were evaluated separately and also, together by data fusion. Appropriate selection of the DESI-MS solvent allowed acquisition of multiple images from the same tissue section while preserving tissue morphology for subsequent histopathology, allowing correlation of chemical, spatial, and pathologic information (2).

Differentiation of Gliomas and Brain Parenchyma. The chemical differences between brain parenchyma and gliomas were explored by comparing the molecular information obtained in the two MS profiles and evaluating their ability in differentiating disease state (i.e., normal vs. tumor). DESI-MS imaging revealed that gray and white matter mass spectra differ and could be defined spatially (*SI Appendix*, Fig. S1); however, areas of mixed composition were also noted. Gray matter (Fig. 1*A*) is comprised of glia and mostly unmyelinated neurons, and it is associated with a very abundant peak at *m/z* 834 identified by high-resolution MS and MS/MS fragmentation as phosphatidylserine (PS) with 40 carbons with 6 units of unsaturation (40:6); predominant acyl chains are 18:0 (stearic acid) and 22:6 (docosahexaenoic acid) as indicated by MS/MS (*SI Appendix*, Fig. S2). White matter (Fig. 1*B*) is characterized by an increased relative abundance of *m/z* 788 (PS 18:1–18:0), 888, 906, and 916. Sulfatides [e.g., *m/z* 888; (3′-sulfo)GalCer 24:1] are particularly abundant, which correlates with the increased myelination of neurons. The pattern of ions that corresponded to gray and white matter was consistent with previous studies of murine brain tissue (25). The variations seen in the ratio of the signals associated with *m/z* 834 and 888 do not compromise the differences in relative abundance between gray and white matter (*SI Appendix*, Fig. S4). Additional information on the identification of ions detected in the lipid profile can be found in *SI Appendix* (*SI Appendix*, Figs. S2 and S3 and Table S1). Differences in the lipid profiles were noted between anatomical regions of the brain, such as the molecular layer of the cortex and the other cortical layers (e.g., in the specimen shown in *SI Appendix*, Fig. S5). The *m/z* 788, 834, and 885 varied between the molecular layer, which surrounds a meningeal blood vessel (apparent in the ion image of *m/z* 788) and that of the cortex itself. Furthermore, unsupervised multivariate analysis by interactive brushing (26) supports the observed differences. Specific cases of special pathological or chemical interest like this one are discussed throughout. The average mass spectrum for gliomas (Fig. 1*C*) is very different from that of normal brain parenchyma, in that it lacks the ions at *m/z* 834 and 888 characteristic of gray and white matter, respectively. Rather, an increase in the abundance of *m/z* 794 [chloride adduct of phosphatidylcholine (PC) 34:1] and *m/z* 885 [phosphatidylinositol (PI) 18:0_20:4] was noted.

Principal component analysis (PCA) was performed on the lipid profiles selected from pathology-defined regions of brain parenchyma and glioma tissue sections (Fig. 1 *D* and *E*). Gray and white matters were well-separated based primarily on *m/z* 834 and 888, respectively. The dispersed locations of a few gray and white matter points, those that fall between their respective groupings, corresponded to tissue of mixed composition as reflected in the mass spectra (*SI Appendix*, Fig. S6). This observation reflects typical parenchyma composition, which contains a mixture of unmyelinated and myelinated neurons as well as glial cells. Brain parenchyma and glioma were well-separated in PCA space, indicating that the first level of pathologic evaluation (is this a glioma or brain parenchyma?) can be answered readily. Interestingly, the glioma grouping was dispersed (Fig. 1*D*). Dispersion along the vector of gray and white matter separation (right to left) is related to the relative contribution of the parenchyma background to the detected lipid profile. Specimen 42 (secondary infiltrated; with ~40% tumor cell concentration) is illustrative of the juxtaposition

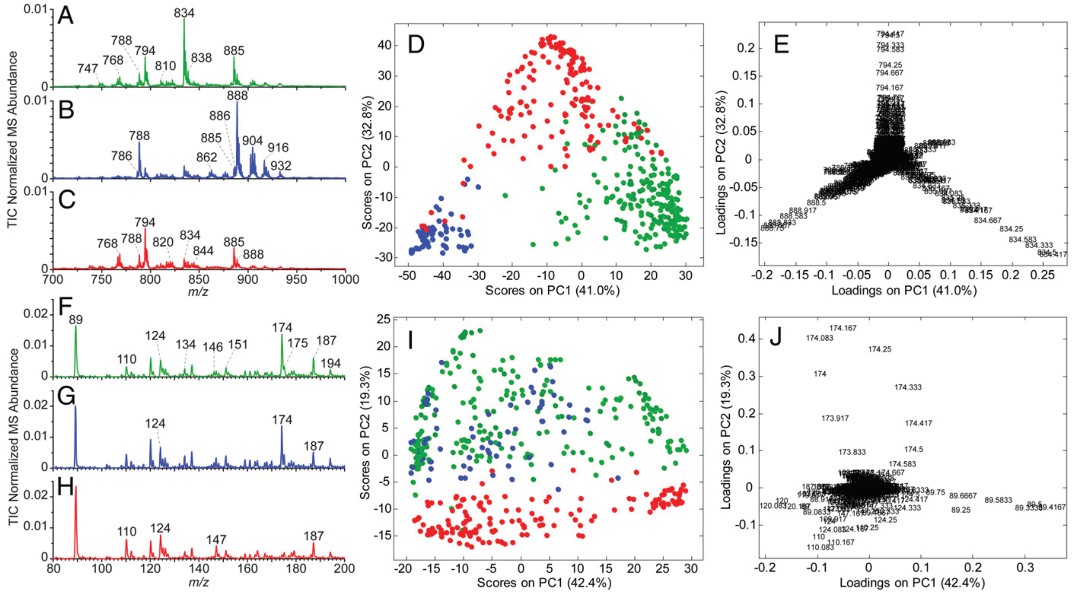

Fig. 1. Average lipid (*m/z* 700–1,000) and metabolite (*m/z* 80–200) MS profiles for gray matter ($n = 223$), white matter ($n = 66$), and glioma ($n = 158$) with PCA score and loading plots. Average normalized [total ion chronogram (TIC)] lipid MS profile for (*A*) gray matter, (*B*) white matter, and (*C*) glioma. (*D*) PCA score plot [principal component 1 (PC1) vs. principal component 2 (PC2)] using lipid profile information for gray matter (green circles), white matter (blue circles), and glioma (red circles). (*E*) PCA loading plot with *m/z* annotated. Average metabolite MS profile for (*F*) gray matter, (*G*) white matter, and (*H*) glioma. (*I*) Metabolite profile PCA score plot for gray matter, white matter, and glioma and (*J*) corresponding PCA loading plot.

of gray and white matter regions (*SI Appendix*, Figs. S7 and S8) and the contribution of the background parenchyma to the lipid profile. The differences between gray and white matter can overshadow more subtle differences that indicate the presence of invasive tumor cells. This observation does not preclude the differentiation of normal tissue, infiltration, and gliomas but rather, confirms the complexity associated with brain tumors. The dispersion of the glioma class in the vertical direction in PCA score space (Fig. 1*D*) reflects the extent of infiltration of tumor cells. A likely contribution to the observed dispersion of the glioma group is the presence of glioma subtypes (e.g., astrocytoma and oligodendroglioma), which are related to the glial cells from which the cancer is derived. For example, the lipid profile of an oligodendroglioma might appear more similar to white matter, which is composed of a greater number of oligodendrocytes than gray matter. Discrimination of glioma subtypes has been previously studied (9) and is outside the scope of this study. Note that subsequent histopathologic evaluation revealed that normal specimens commonly contained various levels of secondary infiltration. The gray and white matter classes were comprised of regions containing <25% tumor cell concentration (mode was 10%), and one sample contained 40% tumor cell, representing a tissue composition that is reasonably expected near the surgical margin. A few samples well-separated from the glioma class in PCA space were considered completely normal and found by the pathologist to contain no observable tumor cells (<5%). Glioma points that fell between the glioma group and either the gray or white matter group illustrate the disease spectrum and the complexity in determining the disease state with contributions of background parenchyma and infiltration.

The metabolite profile, acquired subsequent to the lipid profile, has not been explored previously by DESI-MS in human brain tissue. The average metabolite profile mass spectra obtained from gray matter, white matter, and gliomas are displayed in Fig. 1 *F*–*H*, respectively. The anion of lactic acid was detected at *m/z* 89 (identified by exact mass measurements) (*SI Appendix*, Fig. S9 and Table S1) and occurred in slightly increased abundance (128.9 ± 17.5%) in gliomas vs. healthy tissue. This observation is consistent with metabolic aberrations inherent in cancer (e.g., high rates of aerobic glycolysis) as postulated by Warburg (27), but it does not seem to be uniquely predictive of disease. By contrast, a dramatic decrease in *m/z* 174 was noted between gray and white matter and gliomas. A box and whisker plot (Fig. 2*A*) indicated that *m/z* 174 alone allows discrimination of brain parenchyma from glioma (Kruskal–Wallis *P* value <0.001). Furthermore, a receiver-operating characteristic curve of brain parenchyma and glioma resulted in an area under the curve of 0.998 (*SI Appendix*, Fig. S10). Exact mass (Fig. 2*B*) and MS/MS fragmentation obtained by collision-induced dissociation (Fig. 2*C*) were used to identify *m/z* 174 as *N*-acetyl-aspartic acid (NAA) detected as the deprotonated ion. The dramatic difference between gray matter and glioma tissue is illustrated in specimen 51 (Fig. 2*D*). The intensities of *m/z* values 174, 794, 834, and 888 are plotted from individual pixels noted in Fig. 2*E* over the transition region from glioma to gray matter (Fig. 2*F*). The changes in the lipid ions correctly reflect the regions indicated as glioma and brain parenchyma by pathology (*SI Appendix*, Fig. S11). The change in NAA is evident with a similar rate of change to the lipids near the boundary of the two regions (approximately at pixel 12).

PCA was performed on the metabolite profile (Fig. 1 *I* and *J*) and yielded poor separation of gray and white matter from each other but clear separation between brain parenchyma and glioma. The overwhelming significance of NAA in the multivariate separation is notable. Interestingly, this finding supports previous MRSI studies that indicated the significance of NAA in discriminating normal and diseased neural tissues (28, 29) and current use in

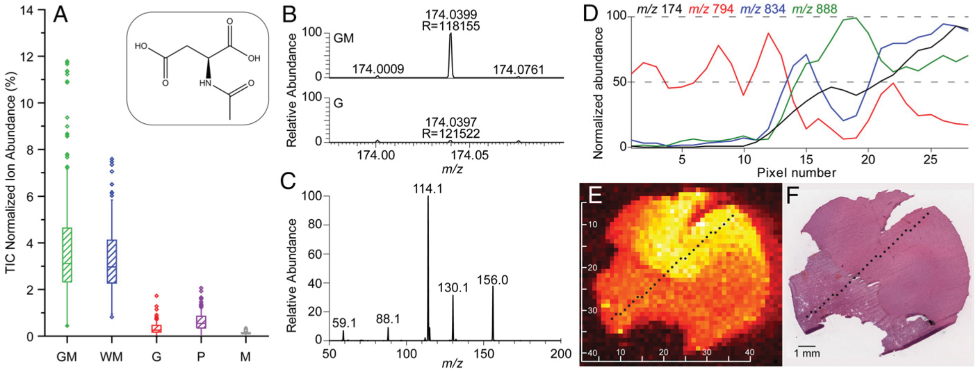

Fig. 2. Statistical significance and identification of NAA. (*A*) Box and whisker plot for *m/z* 174: gray matter (GM), $n = 223$; white matter (WM), $n = 66$; glioma (G), $n = 158$; pituitary (P), $n = 154$; and meningioma (M), $n = 111$. The box represents the interquartile range with a median line and whiskers ±1.5 SD; outliers are represented by open circles. (*A*, *Inset*) NAA. (*B*) Detection of NAA by high-resolution MS in (*Upper*) gray matter and (*Lower*) high-grade glioma in specimen 51; *m/z* and resolution are annotated. (*C*) Collision-induced dissociation (CID) MS/MS fragmentation pattern obtained for NAA from gray matter in specimen 51. (*D*) Plot of intensity change of select ions [*m/z* 174 (black), 794 (red), 834 (blue), and 888 (green)] occurring with the transition between high-grade glioma and brain parenchyma in specimen 51. The pixels plotted in *D* (those of the horizontal scale bar) are indicated in the false-color image of a summed set of ions (281, 303, 788, 834, 885, and 888) in *E*. (*F*) H&E image of specimen 51 with approximate location of pixels.

tumor diagnosis (13, 30). However, detection of NAA in situ by MS has greater molecular specificity and speed compared with MRSI. NAA is an abundant molecule in the human nervous system, the biological function of which is still to be unraveled, but evidence indicates a significant role in neural metabolism (31). Ties to central metabolic processes can be made by aspartic acid as well as acetate, including lipid metabolism, energy production, amino acid synthesis, and gene regulation (31). Furthermore, NAA has been found to decrease in many neurological diseases and disorders, such as stroke, Alzheimer's disease, epilepsy, and multiple sclerosis (31). A reduction in the relative abundance of NAA was also noted in specimens containing reactive matter (*SI Appendix*, Fig. S12); thus, NAA seems to be an important measure of overall neural health.

2-Hydroxyglutaric acid (2HG; *m/z* 147) was also detected in the metabolite profile in some of the glioma samples. 2HG is a downstream metabolite of IDH mutations and serves as an important prognostic indicator (32, 33). The presence of *m/z* 147 in specimen 51 was confirmed by MS/MS (*SI Appendix*, Fig. S13) and found to correlate with the pathologically determined IDH mutation status. The presence of *m/z* 147 in the metabolite profile (full-scan mode) was indicative of 2HG presence, but additional specificity and confirmation were achieved by MS/MS. The detection of 2HG and its correlation with IDH mutation status are outside the scope of this report, having been investigated previously (33). The ability to ascertain such information rapidly expands the value of DESI-MS methodology beyond tissue diagnosis.

The best separation of gray and white matter and glioma was obtained when the lipid and metabolite profiles were considered together using midlevel data fusion (*SI Appendix*, Fig. S14). Gray matter ($n = 223$), white matter ($n = 66$), and gliomas ($n = 158$) were well-separated and had little intraclass dispersion. PCA followed by linear discriminant analysis (LDA) was performed to estimate classification performance when fusing the two MS profiles. The classification of gray matter, white matter, and gliomas (*SI Appendix*, Table S2) had an overall sensitivity (i.e., measure of the proportion of positives that are correctly identified as such) of 97.4% and a specificity (i.e., measure of the proportion of negatives that are correctly identified as such) of 98.5%. The methodology developed was further evaluated by predicting the disease state and estimating the tumor cell concentration of a pathologically ambiguous specimen (Fig. 3) as an external validation. A false-color plot of the PC1 scores of individual pixels (*SI Appendix*, Fig. S15) revealed a region associated with glioma (red pixels in Fig. 3*A*) and a region more closely associated with white matter (blue pixels in Fig. 3*A*). Pathologic evaluation (Fig. 3*B*) of these two regions was ambiguous, with one clearly a glioma and the other being either a diffuse glioma or an infiltrated region adjacent to the tumor region, qualitatively matching our findings of two chemically different regions. Additional evaluation was performed using PCA LDA as shown in Fig. 3*C*, which classified a region of glioma (on the right in Fig. 3*C*) while classifying the adjacent region as white matter (on the left in Fig. 3*C*). The region classified by LDA as white matter prompted additional examination for infiltration (because infiltration was not a part of the PCA LDA model) by estimation of the tumor cell concentration. The tumor cell concentration of each pixel (Fig. 3*D*) was calculated by regression of a semilogarithmic plot of the natural log of NAA's TIC normalized abundance vs. tumor cell concentration (Pearson's $r = -0.89$) (*SI Appendix*, Fig. S15). The estimated tumor cell concentration in the glioma region was >75%, whereas the other region had estimated concentrations ranging from ~50% to 30%, roughly matching with pathologic evaluation of 60%. This illustrative example supports that MS profiles, processed using multivariate statistics, can correctly discriminate gliomas and that they can also be used to detect diffuse and infiltrative tumors, a particularly critical question during surgical resection.

Discrimination of Tumor Types. Meningiomas and pituitary tumors represent a large fraction of all brain tumors; the lipid profile of the former was explored in a previous study (11). We sought to differentiate the tumor types investigated: glioma, meningioma, and pituitary tumor. The average lipid mass spectra displayed differences in the relative abundances of *m/z* 788, 794, and 885 between the tumor types (*SI Appendix*, Fig. S16). The metabolite profile, previously discussed as being highly significant for glioma discrimination, was less informative for meningiomas and pituitary tumors, with small changes being noted in the average mass spectra. PCA performed on glioma ($n = 158$), meningioma ($n = 111$), and pituitary tumors ($n = 154$) using the lipid information

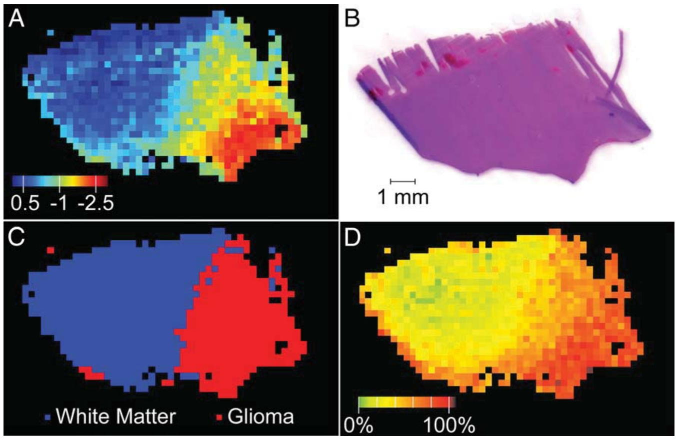

Fig. 3. DESI-MS predictions for specimen 65 and corresponding H&E. (*A*) PCA projection (false color) indicates PC1 score values. (*B*) H&E stain. (*C*) PCA LDA prediction of class and (*D*) calculated tumor cell concentration based on NAA abundance.

provided good separation between all tumor types and was supported by PCA LDA estimation of sensitivity (99.4%) and specificity (99.7%) (*SI Appendix*, Table S3). Although remarkable, this result is not surprising, because the cells and tissue from which the various tumors arise are quite different (e.g., glia vs. meninges), which is also reflected in histopathologic evaluation. The midlevel fusion of metabolite and lipid profile information did not substantially change the predicted classification. However, the average metabolite MS for meningiomas indicated the lowest amounts of *m/z* 89 (lactic acid) and 174 (NAA). In the case of NAA, the absence is supported by previous NMR and liquid chromatography-MS studies (34), thus serving as an endogenous positive control (i.e., signal neither expected nor detected). DESI-MS ion images of specimen 20 (*SI Appendix*, Fig. S17) illustrate the considerable difference between gray matter and an invasive boundary of a meningioma. Differential levels of NAA in gliomas, meningiomas, and pituitary tumors were reported by MRSI, and our data support these previous findings (29) (Fig. 2*A*). NAA signals were significantly different between tumor types ($P < 0.001$), although the lack of significant change (such as that observed between normal brain parenchyma and glioma) limits the predictive value of NAA for discriminating between tumor types. Comprehensively, lipid and metabolite profiles subjected to PCA yielded separation of gliomas, meningiomas, and pituitary tumors with little ambiguity, suggesting that an unknown sample from one of these three types of tumor could be chemically recognized by the MS profiles.

DESI-MS Imaging and Characterization of Human Brain Tissue Smears. DESI-MS analysis of tissue smears is an attractive alternative to the use of tissue sections, removing the need for tissue freezing and sectioning. To date, DESI-MS analysis of tissue and cytological smears has been only briefly explored (7, 33). Smears are commonly performed by placing a minute amount of tissue onto a glass slide and then physically spreading the material to achieve a relatively uniform and diffuse layer of cellular material for staining and subsequent pathology. Smears are typically made using less than 50 mm^3 tissue. A custom tissue smear device was designed to confine the tissue to the middle of the glass slide (along the narrowest dimension) and smear the tissue along the longest dimension with an approximate thickness of 100 μm (*SI Appendix*, Fig. S18).

Tissue smears were imaged over an area of ~75 mm^2, exploring the MS quality and the homogeneity of the chemical information. The absolute MS signal was generally equal to that of tissue sections. Importantly, the relative abundances of the ions were similar between tissue sections and tissue smears. The average metabolite and lipid profiles of gray matter and gliomas (*SI Appendix*, Fig. S19) mirror those of the tissue sections. For example, the abundance of *m/z* 834 is notable in the gray matter spectrum and dramatically reduced in the gliomas. Similarly, the statistical significance of NAA (*m/z* 174; $P < 0.001$) allows for the discrimination of gray matter and gliomas (*SI Appendix*, Fig. S20). Canonical correlation analysis (CCA) (35) was performed to assess the similarity of the chemical information obtained from tissue smears and sections (*SI Appendix*, Fig. S21). The correlation coefficients are notable (greater than 0.95) between the first three canonical variables for both the lipid and metabolite profiles, emphasizing that the physical change induced by smearing does not influence the chemical information. As a precaution, it should be mentioned that the sample matrix and associated analytical effect could influence the data obtained by MS, but this effect was not observed in our experiments. The lipid and metabolite profiles of smears were nearly identical to those recorded from tissue sections, indicating that sectioning can be foregone for more rapid tissue smear analysis.

Conclusions

The application of DESI-MS in brain cancer resection requires knowledge of the characteristic chemical features that distinguish brain parenchyma from glioma and different tumor types from each other, and these differences are explored here for the first time to our knowledge. The strategy of using MS profiles to characterize tissue differs from the traditional use of biomarkers, in which a single molecule (or ion detected by MS) is used as an indicator of disease. MS profiles are an integrated representation of downstream metabolism and provide important information that extends beyond tissue diagnosis (e.g., in the case of 2HG to prognosis).

In this study, we show that MS analysis of tissue sections revealed lipid-derived and metabolite signals that differ between gray and white matter and gliomas, facilitating discrimination by multivariate statistics. Difference in the MS profiles revealed the effect of brain parenchyma on the signal obtained from glioma samples. This observation is particularly significant, because gliomas frequently invade along white matter tracts, illustrating the need to understand the contribution of brain parenchyma and infiltration in predicting disease state. The significance of NAA in discriminating brain parenchyma and glioma is clear and immense. This study offers strong evidence that NAA is, in fact, an oncometabolite and the first in situ detection, to our knowledge, of NAA by ambient MS. The importance of NAA in glioma differentiation confirms nearly 20-y-old MRSI data. NAA also seems to be predictive of tumor cell concentration in unknown samples with an exponential-like decay in MS signal from brain parenchyma to glioma. Fusion of the lipid and metabolite MS profiles provided the best discrimination of brain parenchyma (gray and white matter) and gliomas, with an overall sensitivity of 97.4% and a specificity of 98.5%. Furthermore, the MS profiles proved capable of discriminating tumor types (i.e., glioma, meningiomas, and pituitary tumors) with sensitivity and specificity >99%.

Surgical intervention of brain tumors could be simplified with intraoperative analysis of tissue without extending operative times. Tissue smears that eliminate the need for tissue freezing and sectioning before DESI-MS were explored. The use of a custom 3D-printed smear device aided in the distribution of tissue during smearing while maintaining a sufficiently thin smear for DESI-MS. The observed lipid or metabolite profiles were not significantly altered by the physical act of smearing, and their signal intensities were comparable with those of tissue sections. Furthermore, the chemical information obtained from tissue smears was equivalent to that from tissue sections as determined by CCA. The validation of tissue smears as samples for discriminate analysis remains to be fully vetted; however, this work lays the foundation for implementation of DESI-MS intraoperatively.

Materials and Methods

Cryopreserved human neurological specimens were obtained from 74 patients (58 patients of whom were included in the sample cohort) through the Biorepository of Methodist Research Institute. Tissue specimens were prepared as tissue sections and tissue smears on glass microscope slides and stored at −80 °C before analysis. MS measurements were performed on a linear ion trap mass spectrometer (Finnigan LTQ; Thermo Electron Corporation). High-resolution MS measurements were performed using an Orbitrap Mass Spectrometer (Exactive, Thermo). DESI-MS was performed using dimethylformamide-acetonitrile (1:1 vol/vol), which preserved tissue morphology for subsequent pathology. Blind histopathologic evaluation was performed by an expert pathologist. Sections and smears were subjected to two sequential negative-mode DESI-MS image acquisitions (250-μm pixel resolution). The first image included data from *m/z* 200–1,000, with the mass spectrometer tuned for maximum transmission of *m/z* 786. The moving stage was then reset to the origin position, allowing for a subsequent image was acquired from *m/z* 80–200 (MS tuned for *m/z* 174). Data were exported from XCalibur 2.0 into .csv files, which were then imported into MATLAB. In-house MATLAB routines were used to process all MS data unless otherwise specified. Multivariate statistics, including PCA, midlevel data fusion PCA, and CCA, were performed on the data. Kruskal–Wallis nonparametric test was used to evaluate the statistical significance of NAA. Additional information and discussion of the materials and methods can be found in *SI Appendix*.

ACKNOWLEDGMENTS. The authors thank the Purdue University for Cancer Research, Clint Alfaro, Paolo Oliveri, Cody Howell, and George Sandusky. Research was supported by National Institute of Biomedical Imaging and Bioengineering of the NIH Grant R21EB015722. V.P. thanks the American Society for Mass Spectrometry (ASMS) for a 2015 ASMS Post-Doctoral Award.

1. Domin M, Cody R, eds (2014) *Ambient Ionization Mass Spectrometry* (Royal Society of Chemistry, Cambridge, United Kingdom).
2. Eberlin LS, et al. (2011) Nondestructive, histologically compatible tissue imaging by desorption electrospray ionization mass spectrometry. *ChemBioChem* 12(14):2129–2132.
3. Kerian KS, et al. (2015) Differentiation of prostate cancer from normal tissue in radical prostatectomy specimens by desorption electrospray ionization and touch spray ionization mass spectrometry. *Analyst (Lond)* 140(4):1090–1098.
4. Dill AL, et al. (2011) Multivariate statistical identification of human bladder carcinomas using ambient ionization imaging mass spectrometry. *Chemistry* 17(10):2897–2902.
5. Dill AL, et al. (2010) Multivariate statistical differentiation of renal cell carcinomas based on lipidomic analysis by ambient ionization imaging mass spectrometry. *Anal Bioanal Chem* 398(7-8):2969–2978.
6. Masterson TA, et al. (2011) Distinctive glycerophospholipid profiles of human seminoma and adjacent normal tissues by desorption electrospray ionization imaging mass spectrometry. *J Am Soc Mass Spectrom* 22(8):1326–1333.
7. Jarmusch AK, et al. (2015) Characteristic lipid profiles of canine non-Hodgkin's lymphoma from surgical biopsy tissue sections and fine needle aspirate smears by desorption electrospray ionization–mass spectrometry. *Analyst (Lond)* 140(18):6321–6329.
8. Eberlin LS, et al. (2014) Molecular assessment of surgical-resection margins of gastric cancer by mass-spectrometric imaging. *Proc Natl Acad Sci USA* 111(7):2436–2441.
9. Eberlin LS, et al. (2012) Classifying human brain tumors by lipid imaging with mass spectrometry. *Cancer Res* 72(3):645–654.
10. Eberlin LS, et al. (2013) Ambient mass spectrometry for the intraoperative molecular diagnosis of human brain tumors. *Proc Natl Acad Sci USA* 110(5):1611–1616.
11. Calligaris D, et al. (2015) Molecular typing of meningiomas by desorption electrospray ionization mass spectrometry imaging for surgical decision-making. *Int J Mass Spectrom* 377:690–698.
12. Ostrom QT, et al. (2014) CBTRUS statistical report: Primary brain and central nervous system tumors diagnosed in the United States in 2007-2011. *Neuro-oncol* 16(Suppl 4):iv1–iv63.
13. Kwock L (2014) *Proton Magnetic Resonance Spectroscopy and Spectroscopic Imaging of Primary Brain Tumors. Functional Brain Tumor Imaging* (Springer, Berlin), pp 143–167.
14. Jermyn M, et al. (2015) Intraoperative brain cancer detection with Raman spectroscopy in humans. *Sci Transl Med* 7(274):274ra19.
15. Pogue BW, et al. (2010) Review of neurosurgical fluorescence imaging methodologies. *IEEE J Sel Top Quantum Electron* 16(3):493–505.
16. van Dam GM, et al. (2011) Intraoperative tumor-specific fluorescence imaging in ovarian cancer by folate receptor-α targeting: First in-human results. *Nat Med* 17(10):1315–1319.
17. Shankar GM, et al. (2015) Rapid intraoperative molecular characterization of glioma. *JAMA Oncol* 1(5):662–667.
18. Barceló-Coblijn G, Fernández JA (2015) Mass spectrometry coupled to imaging techniques: The better the view the greater the challenge. *Front Physiol* 6(3):3.
19. Yoshimura K, et al. (2012) Analysis of renal cell carcinoma as a first step for developing mass spectrometry-based diagnostics. *J Am Soc Mass Spectrom* 23(10):1741–1749.
20. Mandal MK, et al. (2013) Biomolecular analysis and cancer diagnostics by negative mode probe electrospray ionization. *Analyst (Lond)* 138(6):1682–1688.
21. Wei Y, et al. (2015) Tissue spray ionization mass spectrometry for rapid recognition of human lung squamous cell carcinoma. *Sci Rep* 5(2015):10077.
22. Kononikhin A, et al. (2015) A novel direct spray-from-tissue ionization method for mass spectrometric analysis of human brain tumors. *Anal Bioanal Chem* 407(25):7797–7805.
23. Agar NY, et al. (2011) Development of stereotactic mass spectrometry for brain tumor surgery. *Neurosurgery* 68(2):280–289.
24. Balog J, et al. (2013) Intraoperative tissue identification using rapid evaporative ionization mass spectrometry. *Sci Transl Med* 5(194):194ra93.
25. Eberlin LS, Ifa DR, Wu C, Cooks RG (2010) Three-dimensional vizualization of mouse brain by lipid analysis using ambient ionization mass spectrometry. *Angew Chem Int Ed Engl* 49(5):873–876.
26. Pirro V, Eberlin LS, Oliveri P, Cooks RG (2012) Interactive hyperspectral approach for exploring and interpreting DESI-MS images of cancerous and normal tissue sections. *Analyst (Lond)* 137(10):2374–2380.
27. Warburg O (1956) On the origin of cancer cells. *Science* 123(3191):309–314.
28. Preul MC, et al. (1996) Accurate, noninvasive diagnosis of human brain tumors by using proton magnetic resonance spectroscopy. *Nat Med* 2(3):323–325.
29. Kinoshita Y, Yokota A (1997) Absolute concentrations of metabolites in human brain tumors using in vitro proton magnetic resonance spectroscopy. *NMR Biomed* 10(1):2–12.
30. Soares DP, Law M (2009) Magnetic resonance spectroscopy of the brain: Review of metabolites and clinical applications. *Clin Radiol* 64(1):12–21.
31. Moffett JR, Ross B, Arun P, Madhavarao CN, Namboodiri AM (2007) N-Acetylaspartate in the CNS: From neurodiagnostics to neurobiology. *Prog Neurobiol* 81(2):89–131.
32. Dang L, et al. (2009) Cancer-associated IDH1 mutations produce 2-hydroxyglutarate. *Nature* 462(7274):739–744.
33. Santagata S, et al. (2014) Intraoperative mass spectrometry mapping of an onco-metabolite to guide brain tumor surgery. *Proc Natl Acad Sci USA* 111(30):11121–11126.
34. Urenjak J, Williams SR, Gadian DG, Noble M (1992) Specific expression of N-acetylaspartate in neurons, oligodendrocyte-type-2 astrocyte progenitors, and immature oligodendrocytes in vitro. *J Neurochem* 59(1):55–61.
35. Doeswijk T, et al. (2011) Canonical correlation analysis of multiple sensory directed metabolomics data blocks reveals corresponding parts between data blocks. *Chemometr Intell Lab Syst* 107(2):371–376.